Investigation of Microphysical Assumptions in TRMM Radiometer's Rain Profile Algorithm using KWAJEX Satellite, Aircraft & Surface Datasets

[Doctoral Dissertation]

Steven T. Fiorino

Department of Meteorology
Florida State University
Tallahassee, Florida 32306-4520
Tel: 850-644-2575; Fax: 850-644-9639; Email: sfiorin@met.fsu.edu

July 2002

**Undersigned members of Ph.D. Advisory Committee approve
Doctoral Dissertation of Steven T. Fiorino**
[submitted to FSU Department of Meteorology -- July 2002]

_____
Prof. Eric A. Smith
Major Professor
NASA/GPM Project Scientist
NASA/Goddard Space Flight Center

_____
Prof. Noel E. LaSeur
Departmental Committee Member
Department of Meteorology
Florida State University

_____
Prof. Paul H. Ruscher
Co-Major Professor
Department of Meteorology
Florida State University

_____
Prof. Guosheng Liu
Departmental Committee Member
Department of Meteorology
Florida State University

_____
Prof. James B. Elsner
Outside Committee Member (Univ. Rep.)
Department of Geography
Florida State University

_____
Prof. Peter S. Ray
Departmental Committee Member
Department of Meteorology
Florida State University

Report Documentation Page

Report Date	Report Type	Dates Covered (from... to)
01JUL2002	N/A	-

Title and Subtitle	Contract Number
Investigation of Microphysical Assumptions in TRMM Radiometers Rain Profile Algorithm using KWAJEX Satellite, Aircraft & Surface Datasets	Grant Number
	Program Element Number

Author(s)	Project Number
Fiorino, Steven T.	Task Number
	Work Unit Number

Performing Organization Name(s) and Address(es)	Performing Organization Report Number
Florida State University	

Sponsoring/Monitoring Agency Name(s) and Address(es)	Sponsor/Monitor's Acronym(s)
The Department of the Air Force AFIT/CIA, Bldg. 125 2950 P. St. Wright-Patterson AFB, OH 45433	Sponsor/Monitor's Report Number(s)

Distribution/Availability Statement
Approved for public release, distribution unlimited

Supplementary Notes
The original document contains color images.

Abstract

Subject Terms

Report Classification	Classification of this page
unclassified	unclassified

Classification of Abstract	Limitation of Abstract
unclassified	UU

Number of Pages
107

TABLE OF CONTENTS

ABSTRACT

The Tropical Rainfall Measuring Mission (TRMM) level 2 radiometer precipitation profile algorithm employs assumed (cloud model-derived) vertical microphysical structures and radiative transfer within the inversion process to generate rainrate estimates. To date, this algorithm has been evaluated through raingauge and ground radar intercomparisons, algorithm-to-algorithm intercomparisons, diagnostic moisture budget analyses, and physical hypothesis testing. None of these approaches has specifically addressed the underlying microphysical properties of the algorithm itself. Therefore, what remains is perhaps the most fundamental check -- direct intercomparison of the assumed profile microphysics with actual three-dimensional microphysical observations.

This research intercompares *in situ* aircraft microphysical measurements directly with the assumed microphysical parameters of the level 2 TRMM facility radiometer algorithm -- specifically the cloud-radiation model-generated database of the radiometer-only 2A-12 algorithm -- in which retrievals are obtained from reconstructed and coincident TRMM overpasses during the 1999 Kwajalein Atoll field experiment (KWAJEX). The analyzed differences are used to diagnose weaknesses in the assumed profile microphysics and to guide a physically-based reformulation of the microphysical representations in the 2A-12 algorithm which would mitigate the weaknesses. The analysis process includes: (1) creation of a matched-merged microphysics/radiometer/radar database for KWAJEX observations; (2) generation of 2A-12 and radar-only (2A-25) retrievals from prototype aircraft instrument radiometer/radar-derived synthetic TRMM observations; (3) introduction of a passive microwave emission – scattering (*E-S*) coordinate system that permits concurrent mapping and quantitative comparison of radiometer brightness temperatures, radar reflectivities, rainrates, and bulk microphysical parameters; and (4) application of hypothesis testing which asserts that 2A-12 to ground radar-derived rainrate differences are correlated to differences in assumed versus observed liquid-ice bulk microphysical properties derivable from drop size distribution (DSD) information. Thus, the main scientific objective of this research is to identify and overcome the foremost model-generated microphysical weaknesses in the TRMM 2A-12 facility algorithm through analysis of: (1) *in situ* aircraft microphysical observations; (2) ground-, aircraft-, and satellite-based radar measurements; (3) aircraft- and satellite-based radiometer measurements; (4) synthetic satellite radar reflectivities and radiometer brightness temperatures; (5) radiometer-only (2A-12) satellite retrievals; and (6) radar-only (2A-25) algorithm retrievals.

Despite the restricted nature of the *in situ* microphysical measurements, results indicate the assumed 2A-12 microphysical profiles differ most from aircraft observations where ground-aircraft radar and 2A-12 rainrate differences are greatest. The *E-S* coordinate system highlights the 2A-12 algorithm's tendency to match hi-emission/hi-scattering observed profiles to hi-emission/lo-scattering database profiles. This is due to a lack of mixed-layer ice hydrometeor scatterers in the model-generated profiles as compared to observed profiles. Direct comparisons between aircraft measured and model-generated 2A-12 microphysics suggest that, on average, the radiometer algorithm's microphysics database retrieves liquid and ice water contents ~3 times smaller than observed at levels less than 10 km. The 2A-12 rainrate retrievals are shown to be strongly influenced by the algorithm's convective fraction specification. Modification of this factor is proposed as a means to improve 2A-12 rainrate retrievals, however fundamental changes to the cloud-radiation model's ice parameterization would be necessary to physically correct the algorithm's diagnosed mixed-layer ice hydrometeor deficits.

1.0 Introduction & Background

Remotely sensed rainfall measurements, made by either ground-based radars or space-based radiometers and radars including radiometer-radar combinations, offer the only reliable means of obtaining spatially continuous precipitation measurements at the global scale. However, despite the obvious fine scale, volumetric, and continuous coverage advantages of remotely sensed rainfall retrieval, the lack of a complete characterization of the vertical distribution of the optical-radiative properties of precipitation-sized water and/or ice hydrometeors prevents such measurements from being accepted as fully verified (Smith, 1999). With the 1997 launch of the Tropical Rainfall Measuring Mission (TRMM) satellite carrying both the multi-channel passive TRMM Microwave Imager (TMI) measuring the integrated effects of liquid and ice along the instrument viewing paths and the 13.8 GHz Precipitation Radar (PR) measuring detailed vertically-resolved rainrate profiles, critical new analyses regarding the four-dimensional distribution of precipitation and latent heating in the tropics are now available (Kummerow and Okamoto, 1999).

The following subsection reviews the basic microphysical and radiative transfer concepts related to the TRMM algorithm development. A summary of the TRMM facility rainfall algorithms follows, succeeded by a motivating discussion and synopsis related to the main scientific objectives of this dissertation. The main focus of the research is to understand the foremost weaknesses in the assumed microphysics of the TRMM radiometer retrieval algorithm -- in conjunction with *in situ* aircraft microphysical measurements made during the Kwajalein Atoll field experiment (KWAJEX) in 1999. Concomitant with this main scientific objective is the further objective of suggesting physically-based modifications to improve the level 2 radiometer algorithm retrievals.

1.1 Basic Concepts

Unlike standard infrared (IR) satellite sensors, which are sensitive only to the microphysical properties of the uppermost layers of clouds, passive microwave radiometers measure energy that passes through clouds, offering insight into the structure of rainfall itself. Rainrate estimation schemes using passive satellite-based microwave instruments depend on the modification of upwelling surface and atmospheric radiation produced by precipitation-sized hydrometeors. Both scattering and absorption modify the amount of energy reaching the

sensors. Absorption and re-emission of incoming (or outgoing) energy by media between the surface and the sensor changes the brightness temperature properties of the media and generally increases or decreases upwelling brightness temperatures over situations where no significant absorbing constituents are present.

Scattering invariably reduces upwelling brightness temperatures because the upwelling sources almost always exceed the relatively weak downward cosmic source. Water surfaces (such as oceans) offer more favorable backgrounds for passively detecting precipitation since relatively smooth water has relatively lower emissivity at cm-mm microwave frequencies and thus presents a radiometrically cold background in contrast to the warmer radiometric emission produced by precipitating hydrometeors (Wilheit et al. 1977). Land backgrounds generally have larger and more variable emissivities and typically present a warmer and less contrasting background against which to detect the precipitation emission signal (Wilheit, 1986). Nevertheless, significant scattering is detectable over both land and water, depending on the microwave frequency in which scattering increases with frequency.

The degree of scattering and thus the depression in upwelling brightness temperatures caused by scattering is a function of hydrometeor type, hydrometeor size, hydrometeor concentration, and frequency. Kidder and Vonder Haar (1995) list the following important properties of microwave radiative transfer in precipitating media:

- Ice generally only scatters, as ice microwave absorption is typically 2 to 3 orders of magnitude less than ice microwave scattering.
- Liquid water drops both absorb and scatter, but absorption dominates until very large drop sizes become present.
- Scattering and absorption both increase with frequency and with rainrate. However, scattering by ice increases much more rapidly with frequency than scattering by liquid.

Figure 1 illustrates the depression effect due to scattering, the brightness temperature frequency dependence, and ocean/land background differences. The point at which the brightness temperature curves stop increasing with rainrate is the point of "saturation;" increased rainrates beyond saturation result in depressed brightness temperatures mostly due to scattering by ice particles. For example, the 18 GHz over ocean curve in Figure 1 becomes saturated at ~15 mm h^{-1} and ~260 K -- at rainrates above 15 mm h^{-1} the brightness temperatures become depressed below the 260 K peak. While scattering due to large hydrometeors, particularly ice, accounts for much of the depression effect seen in the curves of Figure 1, absorption attenuation due to a lapsed atmosphere also contributes.

The TMI takes observations in 9 channels at 5 frequencies -- 10.7, 19.35, 21.3, 37.0 and 85.5 GHz -- with corresponding resolutions of 36, 18, 17, 10 and 4 km in the cross-track direction, respectively (Kummerow et al., 1998). All frequencies are measured independently in the horizontal and vertical polarization planes except the 21.3 GHz channel, which is measured in the vertical plane only. The TMI resulted from a design modification to the Special Sensor Microwave Imager (SSM/I), except that the TMI has an additional pair of channels at 10.7 GHz and has approximately 2.5 times better spatial resolution due to TRMM's lower orbit altitude of ~350 km (before August 2001) versus SSM/I's ~800 km altitude. Because 10.7 GHz is largely a Rayleigh frequency with respect to typical sizes of precipitating hydrometeors, and since characteristic optical depths relative to the 10.7 GHz channel beam sizes do not saturate, the 10.7 GHz channels provide a nearly linear response to all but extremely heavy rain situations. Additionally, SSM/I's 22.235 GHZ water vapor absorption channel was changed to 21.3 GHz on TMI to avoid saturation near the center of this water vapor absorption line in highly moist atmospheres characteristic of the tropics (Kummerow et al., 1998).

Active microwave sensors, or radars, have been used to monitor precipitation for research and operational purposes for decades. While operational precipitation radars are typically surface-based and there are a few airborne meteorological research radars, TRMM is the first Earth satellite equipped with a rain radar. The TRMM PR is a 13.8 GHz (2.2 cm), non-coherent radar and the only instrument on TRMM that can directly observe the vertical distribution of rainrate and provide unambiguous rainrate estimation over land as well as ocean. The footprint size of the PR is small enough to allow the study of inhomogeneous rainfall effects relative to the comparatively coarser resolution of the lower frequency TMI emission channels. The PR's measuring frequency was selected by considering three issues: (1) the requirement for sufficient dynamic range at the base of the rain profile, (2) a sufficiently narrow beam width to meet spatial resolution requirements, and (3) the requirement to comply with the ITU table of frequency allocations (Kummerow and Okamoto, 1999).

1.2 TRMM Rainfall Retrieval Methods

This ultimate goal of this research is to improve the microphysical-radiation relationships inherent to the radiometer-only level 2 TRMM profile retrieval algorithm (2A-12) in order to achieve higher accuracy and precision with instantaneous retrievals in areas covered by the TMI footprint. In addition to 2A-12 (the TMI facility profile algorithm), other level 2 TRMM facility

algorithms include 2A-25 (the PR facility profile algorithm), and 2B-31 (the combined TMI-PR facility profile algorithm). The papers of Kummerow et al. (1996), Kummerow (1998), Iguchi and Meneghini (1994), Igugchi et al. (2000), Meneghini et al. (2000), Smith et al. (1997), and Haddad et al. (1997) describe the algorithm methods. These algorithms have been validated through raingauge comparisons, ground radar comparisons, PR radar comparisons, algorithm-to-algorithm comparisons, diagnostic moisture budget studies, and physical hypothesis testing. However, the most fundamental validation -- direct comparison of the assumed profile microphysics to three-dimensional microphysical measurements -- has not yet been performed.

First, a brief overview of the previous research leading to the development of the current 2A-12, 2A-25, and 2B-31 algorithms is in order. The principles behind the TRMM 2A-12 passive profiling algorithm began with the development of an SSM/I-based physical rain profile retrieval algorithm for passive microwave brightness temperatures using a high resolution three-dimensional cloud model with explicit microphysics to provide the microphysical underpinnings to the inversion process. The microphysical parameters generated by the cloud model are retained in a large *a priori* database of potential cloud and rainrate profiles that might be observed by the satellite sensors. Radiative transfer computations are then used to calculate the upwelling radiances that might be seen by the satellite. Such an algorithm was described in the studies of Smith et al. (1994a-b) and was based on the theoretical studies of Mugnai and Smith (1988), Smith and Mugnai (1988, 1989), Mugnai et al. (1990), Smith et al. (1992) and Mugnai et al. (1993). An overview of cloud model-based rain profile inversion is found in the papers of Smith et al (1994c) and Wilheit et al. (1994). The key cloud model used for this purpose was the University of Wisconsin Nonhydrostatic Modeling System (UW-NMS) developed by Professor Gregory Tripoli and colleagues (Tripoli, 1992a-b). The radiative transfer model used as the functional for an optimizer-controlled inversion procedure was the 2-stream delta Sobolev model of Xiang et al. (1994), which was described for microwave applications by Smith et al. (1994a).

Concurrent with the development of cloud-radiation modeling type algorithms, Kummerow et al. (1989) and Olson (1989) introduced hybrid statistical-physical retrieval techniques that capitalized on the strengths of both the physical and early empirical approaches. These techniques did not use a cloud model to generate atmospheric profiles, opting instead for a set of radar-derived basic profile structures to simplify the radiative transfer and brightness temperature matching calculations.

The current TRMM 2A-12 facility algorithm uses an *a priori* database of thousands of cloud-model generated microphysical profiles to retrieve surface rainrates. A Bayesian inversion approach, inspired by Evans et al. (1995) and simplified by Kummerow et al. (1996) to avoid iterative radiative transfer calculations, improves the algorithm's efficiency by producing a weighted average of the profiles in the *a priori* database whose multi-channel brightness temperature signature is similar to the observations. The intent is to derive a physical cloud profile that matches the multi-channel calculated brightness temperatures to the observations.

As part of the developmental research on profile inversion methods, potential improvements of the TMI over SSM/I were reported in an aircraft-based study by utilizing the low frequency 10.7 GHz channel on the TMI and the higher spatial resolution offered by the low altitude TRMM orbit (Smith et al., 1994d). This was done using linearly polarized high resolution brightness temperatures from the NASA/Marshall Space Flight Center four-channel (10.7, 19.35, 37.1, and 85.5 GHz) Advanced Microwave Precipitation Radiometer (AMPR) described by Spencer et al. (1994). Following Farrar and Smith (1992), the influence of spatial resolution enhancement on the lower frequency-lower resolution SSM/I channels (19, 22, 37 GHz) was also studied by employing energy-conserving deconvolution transforms on six different SSM/I precipitation retrieval algorithms. This study concluded that retrieval schemes that make use of both emission and scattering frequencies (e.g. 19, 37, and 85 GHz), such as TRMM level 2 profile algorithms, are least susceptible to retrieval bias due to partial beam filling effects inherent to diffraction-limited passive microwave brightness temperature measurements (Farrar et al., 1994).

The current TRMM radar-only retrieval algorithm, 2A-25, is described in detail by Iguchi et al. (2000) and Meneghini et al. (2000). Since the 13.8 GHz frequency band selected for the TRMM PR can be strongly attenuated by heavy rain, the compensation of rain attenuation is the major issue addressed by the retrieval algorithm. The algorithm assigns various drop size distribution models according to rain type, including vertical variations, and corrects for non-uniform beam-filling effects. The attenuation correction is based on a hybrid of the Hitschfeld and Bordan (1954) method and application of the Surface Reference Technique (SRT) applicable to down-looking radars (Meneghini et al., 2000). The algorithm provides distinct drop size distributions for convective, stratiform, and "other" rainfall types.

While not specifically analyzed in this study, more recent research also led to the design and implementation of a Day-1 TRMM combined algorithm (2B-31). This method is essentially a radar retrieval algorithm like 2A-25, except the 10.7 GHz brightness temperature measurements from the TMI are used to estimate total path attenuation at 13.8 GHz -- the frequency of the PR -- while drop size distribution coefficients are obtained from a Bayesian-based inversion scheme. Even though the PR itself can be used to estimate the total path attenuation through the SRT (a somewhat noisy scheme based on the difference in ocean surface cross sections between cloud-free and raining radar pixels, as pointed out by Smith et al., 1997 and references therein), TMI estimates of path-integrated attenuation offer several advantages. The principle advantages of the radiometer-based approach are its independence from the radar measurements, its ease of implementation, and its relatively stable variance properties as compared to the SRT (Smith et al., 1997).

The total path attenuation algorithm is described by Smith et al. (1997), while the algorithm inversion scheme is described by Haddad et al. (1997). The Bayesian technique utilized in the 2B-31 algorithm provides estimates of the drop size distribution (DSD) coefficients from an *a priori* DSD parameter database. To fill the database, DSD observations were acquired from various tropical experimental sites operating disdrometers after which a large number of simulations were performed where three independent DSD parameters were varied over the entire range of potential solutions. For each simulation, the corresponding radar reflectivities and microwave attenuation factors were calculated. Despite complications due to geometric complexity, basic solutions can be obtained by selecting the simulations which best match the observed reflectivities and total path attenuation.

1.3 Scientific Objectives & Motivation

As noted above, the level 2 TRMM radiometer-only algorithm assumes cloud-model generated microphysical profiles in the inversion and radiative transfer processes used to produce rainrate retrievals. A main goal of various TRMM field experiments (such as KWAJEX) was to acquire datasets that could be used to support microphysical analyses and verification studies of all the TRMM algorithms, but more specifically 2A-12 due to its greater dependence on assumed microphysical profiles. However, it may be more precise to state that the main purpose for collecting the TRMM field datasets was to seek *falsification* of the TRMM algorithms (Smith, 1999). Such a deficiency analysis would permit better understanding of TRMM algorithm

strengths, weaknesses, uncertainties, and lead to desired improvements to the radiative transfer models and microphysical parameterizations for achieving more reliable high-resolution rain retrievals. To that end, a foremost objective of this research is to generate matched and merged microphysical-radiometer-radar datasets from the TRMM KWAJEX field experiment. These datasets are then used to determine sources of error in the instantaneous rain retrievals by the level 2 TRMM radiometer facility algorithm related to oversimplified or invalid microphysical assumptions.

An expected benefit of the research will be the development of more accurate methods for retrieving wide swath, radiometer-based instantaneous rainrates from space, noting that TRMM's TMI is the main workhorse for measuring rainfall because the PR's surface coverage is swath-limited and only ~1/3rd the size of the TMI swath. [The major role of the PR on TRMM is to provide details on rain vertical structure -- which are used to help refine the radiometer-based retrievals.] In turn, this provides a better understanding of how the tropical/subtropical water budgets at large scales build up from micro- and mesoscale cloud and precipitation processes. Such results address a core objective of TRMM, that being producing highly representative rainfall climatologies from physically-based and objectively validated retrieval algorithms. The link between vertically distributed rainfall and vertical profiles of latent heating enables this research to further contribute to improved weather prediction through data assimilation and global climate prediction through general circulation model (GCM) validation. Additionally, improvements to the TRMM radiometer algorithm are applicable to the future Global Precipitation Measurement (GPM) mission in which a constellation of satellites, each carrying a microwave radiometer, will provide the main rainfall coverage.

The methodology for this research is discussed in section 2.0. Section 3.0 describes the required datasets and an in-depth discussion of the correlated KWAJEX dataset. Analysis and final conclusions are given in sections 4.0 and 5.0, respectively.

2.0 Methodology

Four steps are followed to achieve the main scientific objectives of this research:

(1)   Generate a merged-matched microphysics/radiometer/radar dataset from the TRMM KWAJEX measurements, "synthesizing" additional TMI/PR data from aircraft radiometer/radar measurements as necessary;

(2)   Focus on areas where the ground radar rainrates and synthesized TMI-derived 2A-12 rainrates differ most, and intercompare assumed 2A-12 and 2A-25 facility algorithm microphysics using an *E-S* coordinate system;

(3)   Analyze and determine the significant differences (or lack thereof) between the *in situ* microphysical measurements and the assumed 2A-12 facility algorithm microphysics and conduct hypothesis testing;

(4)   Suggest a physically-based reformulation of various microphysics-radiative transfer procedures in the 2A-12 algorithm which would mitigate the exposed microphysical weaknesses.

This research investigates the assumed, model-generated microphysics of the 2A-12 algorithm since its retrievals provide complete liquid and ice water content profiles. The remainder of this section provides the details of the methodology with each of the following subsections addressing one of the above steps.

2.1 Generation of KWAJEX Datasets

The KWAJEX dataset pool consist of ten time and space coincident subsets collected during the Kwajalein field experiment, which took place during the months of August and September, 1999 on Kwajalein Atoll, Republic of Marshall Islands (RMI). All datasets generally contain 40140 elements corresponding to "wet" or "raining" AMPR brightness temperature superpixels recorded during the 28 KWAJEX DC-8 flights. A superpixel is the basic KWAJEX dataset intercomparison area unit; it consists of 20 AMPR elements (5 along track, 4 cross track). Briefly, the ten components of the Kwajalein dataset used in this research are: (1) AMPR brightness temperature (Tb) measurements, (2) Kwajalein S-band ground validation radar (GV-radar) reflectivities, (3) 13.8 GHz Airborne Rain Mapping Radar (ARMAR) reflectivities, (4) coincident TMI Tbs, (5) coincident PR reflectivities, (6) synthesized TMI Tbs based on AMPR Tbs, (7) synthesized PR reflectivities based on ARMAR reflectivities, (8) 2A-12 algorithm rainrate retrievals, (9) 2A-25 algorithm rainrate retrievals, and (10) coincident aircraft microphysical measurements. Additionally there are two "wet/dry" 7140-point datasets of AMPR Tbs and ARMAR reflectivities at all KWAJEX superpixels within +/- 10 minutes of TRMM overpasses during the KWAJEX field phase. These datasets are called wet/dry because

they include both raining and non-raining superpixels. Specifics and details of all KWAJEX datasets and components are outlined in section 3.

In addition to rainfall information, the 2A-12 algorithm produces microphysical information related to manipulation of selected microphysical profiles from its database used for the Bayesian estimates. To facilitate the intercomparison with *in situ* aircraft measured data, the observed and assumed facility algorithm microphysics are analyzed into bulk parameters. Specifically, the bulk microphysical parameters include both observed and assumed liquid water content (LWC) and ice water content (IWC) values, as well as water droplet and equivalent ice sphere effective radii/effective variances for both water and ice size spectra. The reasoning behind and calculation procedures for the bulk microphysical parameters are addressed in the next subsection, and further detailed in section 3.

The KWAJEX dataset pool incorporates "synthesized" TMI and PR data. The main reason KWAJEX collected coincident AMPR/ARMAR measurements was due to these instruments' similarities to the TMI and PR. Since coincident aircraft and TRMM overpasses within the Kwajalein ground radar domain turned out to be relatively rare (see Table 1 and Figure 2), the similarities between the AMPR/ARMAR and TMI/PR instruments are exploited via TRMM overpass synthesis to produce a more complete correlated KWAJEX intercomparison dataset. Despite differences in resolution and swath width, viable methods to synthesize TMI and PR data from coincident satellite/aircraft overpasses are developed and described in section 3.0.

2.2 Measured vs. Modeled Microphysics & Radiative Transfer

While the coincidence of aircraft equipped with microphysics-sensing equipment and TRMM overpasses were infrequent events during KWAJEX, they exist in sufficient quantity and are the key in establishing direct microphysical-radiation analyses. Three research aircraft were flown during KWAJEX -- the NASA DC-8, the University of North Dakota (UND) Citation, and the University of Washington (UW) Convair-580. During the KWAJEX field campaign, the DC-8 generally flew at altitudes between 10 and 13 km, the Citation generally flew between 5 and 10 km (except during descent spirals as described by Heymsfield et al., 2002), and the Convair generally sampled from near the surface to as high as 6 km. Each aircraft was equipped with state-of-the-art microphysical instrumentation that included a number of electro-optical probes, namely the, Forward Scattering Spectrometer Probe (FSSP), Two-Dimensional Cloud Probe (2DC), Two-Dimensional Precipitation Probe (2DP), High Volume Particle Sampler

(HVPS), and Cloud Particle Imager (CPI). The FSSP, 2DC, 2DP, HVPS, and CPI are all designed to sample increasingly larger sizes of hydrometeors with decreasing resolution. In addition to the electro-optical probes, the Citation and Convair were equipped with King (hot-wire) and Rosemount (icing) probes to detect cloud liquid water amounts; see explanation within TRMM Common Microphysics Product Definition (CMPD) given in Appendix 2.

The three different aircraft altitude blocks encompassing the majority of the troposphere allow the generation of statistically composited-vertically distributed, observed microphysical profiles for total column intercomparison. The assumed microphysics in the 2A-12 *a priori* cloud-radiation database is specified in the algorithm output in the form of liquid water content (LWC) and ice water content (IWC) at fourteen levels between 0.5 km and 18 km. Assuming a Marshall-Palmer (M-P) drop size distribution (DSD) permits the calculation of bulk level-specific and total column DSD parameters such as water/ice effective radii (r_e^{wat}, r_e^{ice}), and water/ice effective variances (v_e^{wat}, v_e^{ice}) from the LWC-IWC values since the 2A-12 rainrate is only specified for the surface. An assumption of an M-P DSD also allows the calculation of level-specific and/or total column r_e^{wat}, v_e^{wat} and LWC parameters from the range (height) gated rainrate output of 2A-25. Worthy of note, however, is that the assumed effective variances -- a measure of the spread of the DSD -- are constant since the assumed distribution is an analytic expression bearing that property. Therefore, when assumed DSD parameters for the 2A-12 and 2A-25 facility profiles are directly compared to the observed DSD parameters, observed-assumed v_e^{wat}, v_e^{ice} differences are defined completely by the observed variations. However, meaningful intercomparisons between all the observed and assumed microphysical parameters -- total column and level-specific -- are obtained when the profile algorithm rainrates are related through a common framework to the ground validation (GV) radar derived rainrates.

Such a common link between radar and radiometer measurements and observed microphysical parameters with modeled radiation signatures exists empirically in reflectivity/rainrate relationships ($Z=aR^b$). Another, perhaps more physically-based link-up between the radar-radiometer-microphysical realms results from transforming the reflectivity/rainrate measurements into emission and scattering coordinate space. The concept behind this relationship is the Emission-Scattering Chart, which has x- and y-axes defined by an index of volume emission and an index of volume scattering, respectively. Rainrates or reflectivities are linked to their respective emission and scattering indices through time and space

matched measurements and displayed on the z-axis. Early passive microwave precipitation retrieval techniques generally either relied on purely emission-based (e.g. Wilheit et al., 1977, 1991) or scattering-based (e.g. Adler et al., 1993 and Ferraro and Marks, 1995) algorithms when determining the precipitation. Liu and Curry (1992, 1998) coupled the emission and scattering signals to alleviate emission signal saturation at low frequency and high rainrates and the scattering signal's typical insensitivity to low rainrates. Transformation of reflectivity and derived rainrate "surfaces" into emission - scattering coordinate space allows the respective strengths of the radiometer (emission) and radar (scattering) to be combined for simultaneous analysis and graphical visualization. Furthermore, addressing both emission and scattering effects together provides a more complete account of processes involved in cloud-radiation model precipitation retrievals as are employed with the TMI and 2A-12, and retrievals involving attenuating radars and their facility algorithms such as the PR and 2A-25.

The *E-S* indices used for the analysis are calculated from the KWAJEX AMPR 4-channel Tbs. The indices are normalized to values between zero and one with values nearing 1.0 indicating more emission or scattering. The indices are optimized for precipitation-sized emitters and scatterers for the range of AMPR Tbs occurring during the KWAJEX DC-8 overflights. A straight-forward description of the *E-S* index calculation procedure and a script of pseudo-FORTRAN code are included in Appendix 1. Figure 3 illustrates *E*-index and *S*-index values for all KWAJEX wet superpixels in a 40140-point diagram, thus providing a measure of the relative amount of mm-cm microwave energy that is being emitted and/or scattered in each superpixel volume. Each point is further subdivided by color-coding according to its 19.35 and 37.1 GHz saturation/depression characteristics. The color of each point coupled with its location in *E-S* coordinate space allows for interpretation about the total column microphysical properties of the absorbing/scattering layer during the time of measurement. For example, and in simple terms, a point with a *S*-index larger than its *E*-index and color-coded for no 19.35 GHz saturation but scattering at 37.1 GHz would be characterized by an environment containing numerous large ice particles and perhaps only moderate rainrates, while a point with an *E*-index larger than its *S*-index and color-coded for 19.35 GHz saturation but no scattering at 37.1 GHz would be characterized by an environment containing numerous large water drops (i.e., large rainrates), but few large ice particles.

Figure 4 illustrates how volumetric emission – scattering effects on radar reflectivity are plainly apparent in *E-S* coordinates. During KWAJEX, the ARMAR provided 60-m vertical resolution reflectivity measurements at more than 75 % of the AMPR superpixels. These quality controlled ARMAR-AMPR match-ups amount to ~31000 superpixels and are referred to as "ARMAR-AMPR QC" values. In Figure 4 the ARMAR reflectivities are averaged into 1-km layers and illustrated for the layers between 1 and 10 km. In layers below 4 km, the reflectivity surfaces generally exhibit variation only along the emission axis -- that is, reflectivities become larger with larger *E*-index values, but show little change along the scattering axis. This is due to the emission effects of the primarily liquid precipitation at these levels. Above 6 km, the reverse is true -- the variation is mainly along the scattering axis. At these levels, precipitation is mainly ice particles, which are primarily scatter. The in-between 4-6 km layer is the mixed-phase layer, which contains differing amounts of both water and ice precipitation; the ARMAR reflectivity surfaces respond to these mixtures as they vary along both emission and scattering axes.

Figure 5 graphically demonstrates how *E-S* coordinates and the transformation into total column microphysical coordinates are used to link the radar, radiometer, and microphysical measurements to identify differences between what the facility algorithms assume and what is observed. As shown in subplots (a) and (b) of Figure 5, the GV-radar reflectivities are cast into *E-S* space and converted (through the appropriate *Z-R* relation) into rainrates. Note only high quality (HQ) GV-radar points are used, i.e., range < 78 km and satisfying a high interpolation-quality test. The GV-radar rainrates can then be compared to the TRMM facility algorithm rainrates (in this case, 2A-12), such that areas of differences can be identified. The facility algorithm rainrates are then transformed into both assumed and observed total column microphysical coordinates, i.e., subplots (d)-(f). Differences between the assumed and observed microphysics are then calculated, i.e., subplots (g)-(i) and are related back to rainrate discrepancies from the GV-radar measurements (or other facility algorithms). The results shown in Figure 5 are discussed in detail in section 4.

2.3 Determination of Algorithm Discrepancies

As expected and evident in Figure 5, direct comparison of the assumed DSD-derived algorithm microphysics yields distinguishable differences from aircraft measured microphysical data. These differences are linked back to the ground radar measurements and are shown to be greater where the algorithm-derived rainrates differ most from the ground radar rainrates.

As further discussed in sections 3 and 4, the aircraft microphysical measurements were confined to "safe" regions of clouds, typically areas of lower reflectivities and surface rainrates. The total column microphysical measurements were even more limited as they required the close coupling in time and space of at least two aircraft and HQ GV-radar data. Thus a study of level-specific algorithm discrepancies is included in section 4 as well. The level-specific intercomparisons reveal a deficiency in the GV-radar data -- namely that its vertical resolution (layers at 1.5-3.0, 3.0-7.5, 7.5-9.0, and 9.0-12.0 km) is too coarse to yield highly-correlated relationships in direct comparison with aircraft sampled data. In turn, there are more favorable comparisons between specific levels of aircraft microphysical data and the more highly resolved ARMAR reflectivities/rainrates and synthesized 2A-25 PR rainrates and derived microphysics.

Finally, a difference analysis focusing on the high emission/high scattering areas not probed by the aircraft is performed on 2A-12-retrieved liquid water contents and those derived from 2A-25. This analysis highlights the principle advantages offered by the synthesized PR rainrates in this study: (1) they are available at more than 75% of all raining KWAJEX superpixels, (2) they correct for the attenuating effects suffered by the uncorrected ARMAR measurements at higher reflectivities, and (3) they are well-correlated enough to observed liquid water microphysical parameters to allow the calculation (through an assumed DSD) of "proxy" *in situ* measurements where the aircraft measurements are unavailable.

2.4 Suggested Algorithm Reformulation

Because weaknesses of the assumed microphysics can be isolated and quantified in this research, a suggested reformulation of the microphysical guidance within the 2A-12 facility algorithm is developed. The suggested modifications mainly apply to the mixed-layer where *in situ* IWCs are approximately 3 times larger than assumed in the 2A-12 database.

Since these modifications are targeted at improving the 7-category microphysical parameterization scheme used to generate the 2A-12 cloud-radiation database, mixed-layer ice fraction and ice habit characteristics are calculated and included. The KWAJEX CMPD (see Appendix 2) allows the identification of three ice habits in addition to total ice water content. Subtraction of the three habits -- graupel, aggregates, and needle/columns -- from the total precipitation IWC yields a catch-all fourth category, i.e., indeterminate ice particles. In the stratiform cases investigated, fractions for each of the habits in relation to the overall IWC are calculated to aid in development of alternate mixed layer ice mass transfer parameterizations.

3.0 Required Datasets

The initial thrust of the analysis is to merge the existing, previously processed component KWAJEX datasets into a single merged-matched dataset and then to derive additional required components, especially the synthesized PR reflectivities and TMI Tbs. Of the ten "wet" datasets and two 'wet/dry' datasets indicated in section 2.1, seven -- including both the wet/dry datasets -- were previously processed and ready for intercomparison within the merged dataset.   These seven datasets -- the wet AMPR, the wet/dry AMPR, the GV-radar, the wet ARMAR, the wet/dry ARMAR, the coincident (overpass) TMI Tbs, and the coincident PR reflectivities -- are described in the following subsection. Subsequent subsections describe each of the individual derived KWAJEX datasets: 3.2 -- synthesized TMI Tbs; 3.3 -- synthesized PR reflectivities; 3.4 -- 2A-12 retrievals; 3.5 -- 2A-25 retrievals; and 3.6 -- matched aircraft microphysics.

3.1 Previously Processed KWAJEX Datasets

The analysis starts with the 4-channel AMPR Tbs that were collected from approximately 12 km altitude aboard the NASA DC-8.   This dataset was originally processed by Mr. Frank LaFontaine and Ms. Robbie Hood of NASA's Global Hydrology and Climate Center (GHCC). It establishes the basic temporal and spatial reference to which all other KWAJEX data components are matched and is thus the core of the merged dataset. From its 4-channel Tbs, the basic superpixel unit area, E-S indices, 19.35 GHz saturation and 37.1 GHz depression flags, a modified convective/stratiform separation index, and synthesized TMI Tbs are calculated.

As described previously, KWAJEX superpixels generally consist of 20 AMPR elements, which coupled with a nominal aircraft ground speed of ~200 m s^{-1}, ~12 km altitude, and scan rate of 7 s, establishes a 5-scan by 4-element superpixel ground area of about 1.9 km by 1.5 km (at 85.5 GHz).   Since the 85.5 GHz channel is used to define the superpixel size, the lower resolution, larger footprints at the other three frequencies cause those channels to be purposefully oversampled in each superpixel.   Use of the larger superpixel size aids in matching the measurements from other KWAJEX instruments and brings the AMPR resolution closer to the coarser TMI resolution. While a 1.9 km by 1.5 km superpixel size presents some issues in synthesizing TMI values (addressed in subsection 3.2) and in the execution of the 2A-12 algorithm (subsection 3.4), it does not detract from intercomparison analyses conducted on merged dataset components all scaled to the same superpixel area. The primary purpose of the

wet/dry datasets (those only consisting of superpixels within +/- 10 min of TRMM overpasses) is for the synthesis of TMI and PR values, as discussed in subsections 3.2 and 3.3.

Ground truth rainrates for KWAJEX were obtained from the reflectivity measurements of the Kwajalein Ground Validation (GV) S-band radar. The GV-radar component dataset was produced and matched to the 40140-superpixel AMPR dataset by Dr. Sandra Yuter of the University of Washington, Department of Atmospheric Sciences (UWA/AS). Given the superpixel time, latitude, and longitude, Dr Yuter's matching algorithm first finds the closest radar volume in time that is not after the superpixel time but is within 10 min of the superpixel time. Since superpixels and radar pixels cannot be matched exactly, and since the radar beam width is usually 2 km or less at the range of the aircraft, the algorithm calculates statistics on the closest 2×2 km radar pixel. The *Z-R* relationship used to obtain GV-radar rainrates in this research is:

$$Z = 175R^{1.5} \tag{1}$$

where *Z* is reflectivity in units of $mm^6\ m^{-3}$ and *R* is rainrate in mm h^{-1}. This expression was derived specifically for KWAJEX data using the methodology given in Hagen and Yuter, 2002 (S. Yuter, personal communication, 2002). The matched GV-radar data were divided into 5 height layers: (1) below 3.0 km (generally interpreted as 1.5 to 3.0 km), (2) 3.0 to 7.5 km (melting band) layer, (3) 7.5 to 9.0 km (lower ice region) layer, (4) 9.0 to 12.0 km (upper ice region) layer, and (5) above 12.0 km (not used in analysis). Surface rainrates were calculated using reflectivities from the 1.5 to 3.0 km layer only.

The 60-m vertical resolution ARMAR reflectivity measurements for KWAJEX were collected aboard the NASA DC-8 under the direction of the principal investigator for ARMAR, Dr. Steve Durden of the Jet Propulsion Laboratory/California Institute of Technology (JPL/CIT). The ARMAR reflectivity profiles were matched to both the 40140-superpixel wet dataset and 7140-superpixel wet/dry dataset by Dr. Joseph Turk of the Naval Research Laboratory at Monterey. As with the GV-radar, the ARMAR data were matched to the merged dataset by geolocating the ARMAR beams in time-space with each of the AMPR-defined superpixel positions and times. Since the DC-8 flight altitude of about 12 km gave a (nadir) resolution of about 800-meters and the beams were spaced approximately 400 meters apart both along and across-track, there were up to 15 beams per superpixel. Each of these beams was collected and all radar data (including incidence angle) averaged horizontally at each range gate position.

The 7140-superpixel AMPR and ARMAR wet/dry component datasets were created specifically for use in conjunction with coincident TMI and PR overpass measurements to synthesize additional TMI and PR observations. Both the coincident TMI from TRMM 1B-11 data and coincident PR from TRMM 1C-21 data were processed and matched to the merged dataset by Dr. Song Yang of NASA's Goddard Space Flight Center (NASA/GSFC). As noted previously, "coincident" in this research is taken to mean within at most a plus/minus 10-minute time difference. Any AMPR-defined superpixel observed during KWAJEX and occurring within the +/-10 min coincidence window -- regardless of the presence of clouds or precipitation -- was included in the wet/dry datasets.

The coupling of the AMPR (ARMAR) component datasets with the coincident TMI (PR) observations permits the development of relationships between the similar instruments aboard the aircraft and spacecraft. This, as outlined in the next two subsections, allows the synthesis of TMI Tbs and PR reflectivity profiles at all KWAJEX superpixels.

3.2 TMI Synthesis

TMI observations for all KWAJEX superpixels are synthesized by first obtaining channel-specific linear regressions of the wet/dry AMPR measurements to the coincident TMI overpass measurements, and then applying regression equations to the AMPR Tbs of the 40140-superpixel wet dataset for synthesized TMI Tbs. The primary variable in the regressions is the time difference between the AMPR and satellite measurements. While maintaining sufficient dynamic range to include both wet and dry superpixels, the regressions are optimized by minimizing the maximum allowable time difference and maximizing the correlation coefficient of the scatter to the regression. Additionally, the slope stability of the regression as compared to adjacent time difference windows is considered in some cases. All regressions result in optimal maximum time differences of less than 60 seconds -- strong evidence of the short autocorrelation length scale of the precipitation processes.

Both the horizontal and vertical channels of each of the TMI's four rain frequencies are projected from the four, linearly polarized AMPR channels. The lower panels in Figures 6a-d illustrate the synthesis plots of the vertically and horizontally polarized TMI regression curves for each of the four radiometer frequencies. The top panels in these figures show the variation of the correlation coefficients and dynamic range with changes in maximum allowable time difference. The middle panel in Figure 6d plots both the change in 85.5 GHz (vertical and

horizontal) regression curve slope and the variation in correlation coefficient against changes in maximum allowable time difference.

One minor drawback to the above regression optimization procedure is that for a small population of superpixels, the synthesized 37.0 and 85.5 GHz horizontally polarized Tbs exceed the vertically polarized values (see the "crossover" of regression curves at AMPR Tb value of ~280 K in Figure 6c and ~170 K in Figure 6d). These "non-physical" points amount to only 0.04% of 37.0 GHz cases and 0.7% of 85.5 GHz cases and are not used in subsequent analysis

Since the difference between an observed Tb and a surrounding "clear-air" Tb is an input variable to the 2A-12 facility algorithm, clear-air or background Tbs are also calculated for each AMPR channel at all 40140 raining superpixels. These clear-air AMPR Tbs are calculated from the AMPR wet/dry dataset by applying a linear regression to all 4923 completely non-raining (i.e., no wet AMPR full resolution pixels) superpixels over each channel's KWAJEX time series. Diagrams of the clear-air Tb projections for each of the four frequencies are depicted in Figure 7.

Using the synthesis equations shown in Figures 6a-d and 7, vertically polarized and horizontally polarized TMI Tbs are produced for both the wet and clear-air cases (40140 superpixels).

3.3 PR Synthesis

To synthesize PR reflectivities from ARMAR values, a layer-by-layer calibration correction is found based on the reflectivity differences in the uncorrected 1C-21 PR and ARMAR measurements. The layer-by-layer calibration corrections are then applied to the 40140-superpixel wet ARMAR dataset to produce synthesized PR profiles. Because 1C-21 measurements were all made within +/-10 min of a PR overpass, the calibration correction must be made with data in the ARMAR wet/dry dataset, in which approximately 70% of the superpixel profiles are non-raining. As a consequence, there is a dearth of PR echoes for calibration comparisons at most of the 7140 wet/dry superpixels. To improve the statistical significance of the distribution of echoes in the layer comparisons, the 60-m resolution ARMAR data and 250-m resolution PR data are averaged into 1-km layers from the surface to 8 km for the calibration comparisons (the lowest layer is set at 0.5-1 km due to the cluttered nature of the surface returns). A sensitivity threshold of 14 dBZ is set in the ARMAR data so it would more closely match the PR's threshold as evidenced in the 1C-21 data.

Similar to the procedure followed with the TMI synthesis, the primary variable used in optimizing the calibration between the PR and ARMAR data is the maximum allowable time difference between measurement times in the datasets. As an example, the top two panels in Figure 8 illustrate for the 3-4 km layer the variability of the mean and median distribution reflectivities and the change in population size of the matched distribution with respect to the variation in maximum time difference. For a given superpixel to qualify as "matched", the reflectivity values of both radars have to exceed 14 dBZ. Note that unlike the TMI synthesis cases, the optimum combination of matched distribution size and stability in the mean/median differences occurs at a time difference of approximately 6 minutes. This is the case for all layers up to 8 km, except the 0.5-1.0 km layer where using a time difference of 1 min limits the matched distribution enough to eliminate most of the surface contaminated echoes and allows a more refined determination of the calibration correction. The lower two panels of Figure 8 illustrate the histogram distributions of the PR and ARMAR reflectivities in the 3-4 km layer. A weighted average of the mean and median differences -- where slightly more weight is given to the mean differences due to the non-Gaussian nature of the distributions -- is used to set the ARMAR to PR calibration corrections.

Figure 9 shows the smoothed variation with height of the ARMAR to PR corrections for all eight layers. Notably, all differences are less than 1 dBZ, thus suggesting that the two instruments were closely calibrated during KWAJEX, and that they were interrogating the same microphysical phenomena despite the up to 6-min differences in observation times. The 60-m vertical resolution wet ARMAR dataset is then averaged to 250-m resolution and the smoothed ARMAR to PR calibration corrections are applied to produce the synthesized wet PR dataset. Additionally, a high-resolution 60-m wet PR component dataset and 60-m and 250-m PR component datasets consisting of clear-air profiles only (for path integrated attenuation calculations) are produced.

3.4 Synthesized 2A-12 Retrievals

The 2A-12 facility algorithm retrievals used for analysis are the product of a modified version of the current operational algorithm (i.e., Version 5). Modifications to the operational algorithm are necessary to accommodate the format of the inputs, the lack of a water vapor channel input, and the limited field of view (FOV) of the superpixel areas where unique retrievals are desired. Drs. Song Yang and William Olson of NASA/GSFC applied the necessary

changes to the algorithm. With the exception of the 22.3 GHz channel Tbs, the primary input parameters to the modified 2A-12 algorithm are the same as the operational version, i.e., TMI Tbs, TMI background Tbs, and convective fraction. An explanation of the differences in how these input parameters are obtained follows.

Synthetic TMI Tbs and background (clear-air) TMI Tbs are obtained as outlined in subsection 3.2. The 22.3 GHz water vapor channel input to the operational 2A-12 algorithm is mainly used to distinguish between raining and non-raining areas within the TMI FOV. Since *E-S* indices are used to determine all 40140 superpixels in the wet datasets as raining, and background Tbs are synthesized separately using *E-S* determined dry superpixels, the 22.3 GHz Tb input is not necessary for this study. Due to the limited FOV and somewhat independent nature of each of the superpixels (a given superpixel may be seconds or days separated from adjacent superpixels in the intermittent time series), calculation of convective fraction values for each superpixel requires a different approach than is done operationally.

In a manner similar to what is used in the operational 2A-12 algorithm, an AMPR-based convective-stratiform index (CSI) is developed that determines convective fraction from an integration of CSI values for convective or stratiform superpixels as determined by the GV-radar. The technique to calculate a CSI and derive from it convective fraction is an adaptation of a similar scheme detailed in Hong et al., (1999). To calculate the CSI for each superpixel, a combination of the *E*-index and *S*-index weighted by scattering information in the 85 GHz channels is determined as follows:

$$\mathrm{CSI} = (1 - w)\mathrm{E}_{\mathrm{index}} + w\mathrm{S}_{\mathrm{index}} \tag{2}$$

where *w* is defined:

$$w = \begin{cases} 0 & \text{if } \mathrm{T}_{\mathrm{B85}} > \mathrm{T}_{\mathrm{B85bg}} \\ \left(\mathrm{T}_{\mathrm{B85bg}} - \mathrm{T}_{\mathrm{B85}}\right)/80 & \text{if } \mathrm{T}_{\mathrm{B85bg}} - 80 < \mathrm{T}_{\mathrm{B85}} < \mathrm{T}_{\mathrm{B85bg}} \\ 1.0 & \text{if } \mathrm{T}_{\mathrm{B85}} < \mathrm{T}_{\mathrm{B85bg}} - 80 \end{cases} \tag{3}$$

and T_{B85bg} is the background (clear-air) AMPR Tb. As a result of using *E-S* indices, the CSI values are automatically normalized to a range of 0 to 1.

Once the CSI is calculated for all 40140 superpixels, all superpixels characterized as convective or stratiform by the GV-radar convective/stratiform map (adapted from Steiner et al., 1995, and Yuter and Houze, 1997 as tuned for KWAJEX) are divided into 10 CSI bins of 0.1 CSI width (i.e. 0-0.1, 0.1-0.2, 0.2-0.3, etc.). Convective fraction values for each of the CSI bins

are then calculated and plotted versus CSI. The upper panel in Figure 10a depicts the spread of convective and stratiform superpixels by CSI and superpixel sequence number. Superpixels designated stratiform by the GV-radar are generally confined to CSI values less than 0.3; this is quite apparent in the convective fraction diagram (lower panel of Fig. 10a) where the 50% convective fraction threshold is crossed at a CSI of ~0.31. Convective fraction values for all CSI are calculated by interpolation, and thus each of the 40140 wet KWAJEX superpixels is assigned a convective fraction value unique to its CSI value. By identifying which superpixels are more than half convective, a significantly more distinct convective/stratiform separation in *E-S* space is achieved as illustrated in Figure 10b with the contrasting GV-radar convective/stratiform mapping (upper panel) and CSI-derived mapping (lower panel).

The validity of the convective fraction values, as determined above, is predicated upon several assumptions. Most important, the convective fraction procedure assumes spatial and temporal homogeneity in the convective/stratiform "texture" of the FOV during the period of KWAJEX -- a reasonable supposition given that KWAJEX took place in the tropical Pacific in August and September without a tropical cyclone passage. Additionally, the FOV of the KWAJEX radar domain is also assumed to approximate the FOV of the TMI, and the fractional number of superpixels is considered analogous to fractional area.

Derived parameters from the modified 2A-12 algorithm include surface rainrates (total and convective portion), precipitation LWCs/IWCs, and cloud LWCs/IWCs at 14 levels from 0.5 km to 18 km. Only the total surface rainrate and precipitation LWC/IWC profiles are used in this analysis. A superpixel-by-superpixel comparison of the 2A-12 rainrate retrievals versus HQ GV-radar rainrates, as shown in Figure 11a, indicates that the 2A-12 retrievals and the GV-radar retrievals generally produce rainrates similar in magnitude at the same times and locations. However, the scatter diagram and histograms of Figure 11b indicate the 2A-12 rainrates often exceed the GV-radar values by ~60-70% at rainrates greater than 7 mm h^{-1} and often underestimate the GV-radar values by ~50% below 7 mm h^{1}. Additionally, maximum 2A-12 rainrates appear to be "capped" at approximately 35 mm h^{-1}.

To calculate the cloud-radiation model-based DSD shape parameters shown in Figure 5 and described previously in subsection 2.2, the r_e^{wat}/ r_e^{ice} and ν_e^{wat}/ ν_e^{ice} values are derived from the LWCs/IWCs assuming a Marshall-Palmer (Marshall and Palmer, 1948) distribution where:

$$n(D_0) = n_0 \exp(-\Lambda D_0) \hspace{4cm} (4)$$

and $n_o = 8000$ m^{-3} mm^{-1}. Pruppacher and Klett (1997) further show that Λ is related to LWC by:

$$\Lambda = \left[\frac{\rho_w \pi n_0 \times 10^{-3}}{LWC} \right]^{1/4} \tag{5}$$

with units Λ (mm^{-1}), LWC (g m^{-3}), and $\boldsymbol{r}_w$ (water density - g cm^{-3}). Since the inverse of Λ is the DSD's characteristic diameter, D_o, and the effective diameter is $D_{eff} = 3D_o$ (Flatau et al., 1989), the liquid water effective radius, r_e^{wat} (mm), is defined by:

$$r_e^{wat} = \frac{3}{2} \left[\frac{\rho_w \pi n_0 \times 10^{-3}}{LWC} \right]^{-1/4} \tag{6}$$

A similar approach is taken to calculate the ice effective radius, r_e^{ice}, where the water density is replaced by an ice density, $\boldsymbol{r}_{ice} = 0.25$ g cm^{-3} and LWC with IWC. This assumes a precipitation ice distribution with fairly dense spherical ice particles characterized by number concentrations nearly the same as those of the liquid precipitation. This assumption is supported by the high concentrations of graupel particles found in the observed *in situ* data (described in subsections 3.6 and 4.0) and in the observed minus assumed effective radii comparisons of Figure 5h where the r_e^{ice} differences are similar in magnitude to the r_e^{wat} differences.

As noted in subsection 2.2, the assumed distribution effective variances based on the 2A-12 retrievals are constant due to the analytical nature of the assumed DSD. In the case of the full (non-truncated) Marshall-Palmer DSD applied in this analysis, the analytical solution for effective variance reduces to a value of one third (0.33). So while the absolute observed minus assumed effective variance differences shown in Figure 5g are based on the variations in the observed values only, fractional error or difference analyses in section 4.0 use an assumed effective variance value of 0.33.

3.5 Synthesized 2A-25 Retrievals

The 2A-25 retrievals are produced from the synthetic PR reflectivity profiles using the version 6.32 facility algorithm adapted specifically for the merged KWAJEX dataset by Dr. Ziad Haddad of JPL/CIT. Like the 2A-12 analysis discussed previously, modifications to the 2A-25 algorithm are required to accommodate the format of the input data. More importantly, modifications are additionally needed on account of the synthetic surface reflectivities being contaminated and unusable. Without reliable surface cross-section measurements, the techniques employed by the version 6.32 algorithm to estimate attenuation, i.e., the surface reference

technique (Meneghini et al., 2000) or use of adjacent clear-air profiles to calculate path integrated attenuation (PIA), are not possible. Furthermore, the contaminated surface returns hinder the algorithm's convective/stratiform mapping. Thus, Dr. Haddad generated two full 40140-pt datasets -- one assuming all superpixels as convective, the other assuming all stratiform -- by estimating PIA for each profile from the measured reflectivity and TOGA COARE (Tropical Ocean Global Atmospheres/Coupled Ocean Atmosphere Response Experiment) DSD parameters. The remainder of this subsection addresses how the convective-stratiform data are blended for subsequent intercomparison and analysis, and how liquid microphysical data are obtained from modified 2A-25 rainrate retrievals.

The convective and stratiform 2A-25 outputs are blended into a single 40140-pt dataset using the CSI-based convective/stratiform separation technique developed in subsection 3.4. For reasons given in subsection 3.4, superpixels with a CSI > .31 are assigned the *Z-R* relationship for convection whereas superpixels with a CSI value ≤ .31 are assigned the stratiform *Z-R* relationship. The lowest range gates of the 2A-25 retrievals -- the surface, 250-m, and 500-m -- are deemed contaminated and eliminated from subsequent analysis. In fact, the five 250-m range gates in the 1-2 km layer proved to comprise the least noisy, lowest layer. Therefore, in comparisons with the 2A-12 surface rainrates, an average of the 1-2 km layer rainrates is used. In comparisons with the GV-radar, which approximately samples the 1.5-3.0 km layer at its lowest elevation angle, using an average of the 1-2 km layer 2A-25 rainrates yields a closer comparison than using 2A-25 surface rainrates. Averages of the rainrates in the 1-2 km layer are also used for 2A-25 - ARMAR rainrate comparisons.

Figure 12 shows matched superpixel and scatter diagram comparisons of 2A-25 rainrates versus GV-radar, 2A-12, and ARMAR rainrates. In the GV-radar match-up (top panels), only the HQ GV-radar superpixels are used, which results in ~8000 matches. While the 2A-25 rainrates significantly exceed the GV-radar rainrates between matched superpixels 2000 to 4000, overall the scatter is evenly distributed around the 1-to-1 line. The comparison with the 2A-12 rainrates results in about 21000 matches. The matched superpixel diagram of the 2A-25 and 2A-12 rainrates (middle, left panel) indicates good agreement in terms of the timing and proportional magnitudes of the rainrate changes -- perhaps even better agreement than seen in the GV-radar/2A-25 matched superpixel diagram. However, inspection of the 2A-12/2A-25 scatter diagram (middle, right panel) suggests that similar to the comparison between 2A-12 and GV-

radar retrievals (Figure 11b), the 2A-12 rainrates overestimate the 2A-25 rainrates by 60-70% at rainrates greater than 7 mm h^{-1} and underestimate the 2A-25 rainrates by ~50% at rainrates below 7 mm h^{-1}. The bottom panels of Figure 12 illustrate 1-2 km layer comparisons of the 2A-25 rainrates with rainrates derived from uncorrected ARMAR reflectivities in equation (1). The 2A-25/ARMAR comparisons match up at ~31000 superpixels and agree closely in the matched superpixel diagram since the ARMAR reflectivities are used to produce the synthetic PR inputs to 2A-25. The differences between the ARMAR and 2A-25 rainrates are due to 2A-25's distinct convective and stratiform *Z-R* relationships, and its attenuation corrections in areas of higher rainrates. These differences are most evident in the scatter diagram where the 2A-25 rainrates are generally slightly lower than the ARMAR values at rainrates below 10 mm h^{-1} (points designated stratiform by the CSI) and often significantly higher than the ARMAR values at rainrates > 10 mm h^{-1} due to the attenuation correction and the convective *Z-R*.

To make limited microphysical comparisons between 2A-25, 2A-12, and the *in situ* aircraft measurements, a M-P distribution assumption is applied to derive liquid water microphysical parameters from the 2A-25 rainrate retrievals. Only liquid water parameters are derived since the 2A-25 algorithm does not provide IWC values. Liquid water content values are obtained from the rainrates using the relationship given by Pruppacher and Klett (1997), i.e.:

$$\text{LWC} = \frac{\rho_w \pi n_o \times 10^{-3}}{\left(4.1 R^{-0.21}\right)^4} \tag{7}$$

where *R* is rainrate in mm h^{-1}, LWC in g m^{-3}, *r_w* (water density) in g cm^{-3}, and $n_o = 8000$ m^{-3} mm^{-1}. Effective water radius, r_e^{wat}, can be obtained from the LWC values using equation (6), and effective water variance, v_e^{wat}, reduces to $v_e^{wat} = 0.33$ for all M-P DSDs as explained in subsection 3.4.

As a check on the validity of the LWC calculations made from the 2A-25 rainrate profiles, 1-km layer averages of 2A-25 rainrates and derived LWCs are compared to matched *in situ* measurements. Figure 13 depicts matched superpixel and scatter diagram comparisons of average 2A-25 rainrates and derived LWCs to Convair-derived rainrates and LWCs at matched superpixels in the 2-3 km layer. The comparisons in Figure 13 demonstrate the sensitivity of the near vertical-looking ARMAR and its derived/synthetic PR datasets to small-scale microphysical fluctuations. At rainrates below 4 mm h^{-1} and LWCs less than 0.25 g m^{-3}, the agreement between the 2A-25 and Convair values is similar despite the mostly different environmental

conditions in which the measurements were made and processed. At higher rainrates, the 2A-25 values underestimate the Convair values -- due possibly in part to the inadequacy of the fallout equations used in calculating the Convair rainrates from the measured particle spectra. However, the Convair LWC values are calculated without any gravitational assumptions, and the 2A-25 LWC values remain slightly underestimated at LWCs > 0.25 g m^3. Assumptions, conversions, and calculations necessary to obtain the Convair rainrates and LWCs are addressed in the next subsection.

3.6 Matched Aircraft Microphysics

As discussed in subsection 2.2, *in situ* microphysical measurements were collected from three different research aircraft during KWAJEX. The UW Convair-580 data were collected, compiled, and processed for the KWAJEX CMPD dataset by the Cloud and Aerosol Research Group (CARG), led by Dr. Peter Hobbs at the UWA/AS. The UND Citation data were collected, compiled, and processed under the direction of Drs. Jeffery Stith (National Center for Atmospheric Research -- NCAR), Julie Haggerty (NCAR), and Anthony Grainger (UND). The NASA DC-8 microphysical data were prepared for distribution by Dr. David Kingsmill of the Desert Research Institute at the University of Nevada in Reno (UNR/DRI). The four research groups listed above posted the common microphysical product data by priority flight legs composed of varying numbers of 1-km length segments of flight path. These "priority leg" segments of data were then matched in time and space to the merged KWAJEX dataset superpixels for intercomparison and analysis. Subsequent discussion in this subsection describes the priority leg matching methods, the calculations required to obtain derived microphysical data such as effective radii and variances, the adjustments and recalculations made to the lower-level Convair data, and finally some intercomparisons between size-spectra-derived reflectivity and reflectivity measured remotely by the ARMAR.

To match the aircraft microphysical data to the times and geolocations of the superpixels, a maximum time difference of +/- 5 minutes and maximum latitude and longitude differences of +/- 0.01 degrees between the priority leg segment center and the superpixel center are used as matching criteria. The +/- 5 minute time difference is chosen because it falls between the 30 to 45 second satellite/aircraft instrument time differences used for synthesizing the TMI Tbs and the up to 6-minute satellite/aircraft instrument time differences used in synthesizing the PR reflectivities. This time difference is also consistent with the use of HQ GV-radar data, which

are predominantly restricted to superpixel/radar time differences of less than 6 minutes. For locations near the equator -- as is the case for KWAJEX -- the latitude/longitude difference of 0.01 degrees results in a maximum difference between priority leg segment center and matched superpixel center of ~1100 m in either the east-west or north-south directions. This ensures that matched centers are never more than 1.5 km apart and are generally within 1 km of one another, and that geolocation differences are essentially the size of or smaller than the flight segment length and/or superpixel dimensions (1.9×1.5 km).

The matching of the aircraft data to the merged superpixels results in 1012 DC-8 matches, 496 Citation matches, and 450 Convair matches. A diagram of the matched aircraft points in *E-S* coordinate space is shown in the top panel of Figure 14. As is evident in Figure 14, most of the matched aircraft microphysical measurements take place at low emission/low scattering, and generally stratiform superpixels. Only the DC-8 sampled matched superpixels where the AMPR indicates 19.35 GHz saturation (red and green points in the figure), and these measurements are at altitudes above 10 km where virtually no liquid water is present. Presumably, the reason the aircraft data appear restricted to predominately light rain, stratiform regions is due to the safety of flight considerations (thunderstorm avoidance) that were practiced during KWAJEX. To produce total column microphysical profiles from the aircraft data, the *in situ* measurements have to be combined to adequately represent both the liquid water and ice water paths (LWP and IWP). Since only the Convair sampled at levels with enough liquid water to characterize a tropical LWP (below 6 km), superpixels with adequate matched total column microphysics are further restricted to points with Convair plus Citation and/or DC-8 data. The limited nature of the distribution of matched superpixels with total column microphysics is illustrated in the bottom panel of Figure 14.

In addition to the superpixel year, month, day, hour, minute, second, latitude, and longitude data, 19 flight and microphysical parameters are obtained for each superpixel in the matching process. Fifteen of the flight and microphysical parameters are extracted directly from the CMPD-format priority leg segment data and 4 are calculated from the particle size spectra for each segment and then subsequently matched. The 19 parameters, plus 2 additional Convair-only variables (explained below), are given in Table 2. Water and ice effective radii are calculated from the particle spectra using the relationship:

$$r_{eff} = \frac{\int_0^\infty r^3 n(r)dr}{\int_0^\infty r^2 n(r)dr} \approx \frac{\sum\limits_{i=5\,\mu m}^{25\,mm} n_i D_i^3 \Delta D_i}{2\sum\limits_{i=5\,\mu m}^{25\,mm} n_i D_i^2 \Delta D_i} \tag{8}$$

where n_i is the particle concentration per bin per bin width (L^{-1} μm^{-1}), ΔD_i is the bin width (μm), and D_i is the maximum particle dimension (μm) -- which with the assumption for this calculation that all water and ice particles are spheres, becomes diameter. Actual bin widths vary over the measured particle size range of 5 μm to 25 mm and are listed in the TRMM CMPD Version 4 Document (Appendix 2) as follows: 5-40 μm range with 5 μm bin width (7 bins), 40-150 μm range with 10 μm bin width (11 bins), 150-1000 μm range with 50 μm bin width (17 bins), and 1-25 mm range with 400 μm bin width (60 bins). Ice particle concentrations are summed from the individual ice habit concentrations -- graupel, aggregates, needle/columns, and indeterminate ice particles. Water and ice effective variances are similarly calculated using:

$$v_{eff} = \frac{\int_0^\infty (r - r_{eff})^2 \pi r^2 n(r)dr}{r_{eff}^2 \int_0^\infty \pi r^2 n(r)dr} \approx \frac{\sum\limits_{i=5\,\mu m}^{25\,mm} \left(\frac{D_i}{2} - r_{eff}\right)^2 n_i \left(\frac{D_i}{2}\right)^2 \Delta D_i}{r_{eff}^2 \sum\limits_{i=5\,\mu m}^{25\,mm} n_i \left(\frac{D_i}{2}\right)^2 \Delta D_i} \tag{9}$$

Water effective radii and variances for the DC-8 are set to zero since this aircraft flew too high to sample meaningfully liquid water. At temperatures above +5°C, the Convair r_e^{wat}/ r_e^{ice} and v_e^{wat}/ v_e^{ice} values are summed using water and ice particle concentrations recalculated after the conversion of ice artifacts into water spheres. The reasoning for this conversion and how it is performed is explained below.

At levels below ~4 km, the Convair microphysical data derived directly from the priority leg CMPD exhibited an unexpectedly high amount of IWC. After matching with the merged KWAJEX dataset, there remained superpixels where the precipitation IWCs exceeded the coexisting precipitation LWCs at levels with temperatures as high as 10-25°C. This is illustrated in the top panel of Figure 15 where ice fraction of the total precipitation water content (LWC + IWC) is plotted against outside air temperature at matched Citation and Convair superpixels. Ice fraction values are generally > 0.9 at temperatures below –10°C. At temperatures between –10 and +2°C, ice fractions drop below 0.7 in both the Citation and Convair data. However, at temperatures above +5°C, the Convair ice fraction values begin to increase towards 1.0 rather

than rapidly approach zero as might be expected in a tropical atmosphere. The principal investigator (PI) for the Convair microphysical data explained that the warm-layer precipitation IWCs were due to "ice artifacts caused by drop splashing" (P. Hobbs, personal communication, 2002) created by the impact of large rain drops on the aircraft instrumentation. Since the TRMM microphysics software used by the TRMM PIs to produce the CMPD data identified ice and ice habits by particle shape without reference to temperature, the fragmented rain drops evidently appeared non-spherical and were classified as ice (D. Kingsmill, personal communication, 2002).

While the warm-layer ice artifacts led to IWCs that were insignificant as compared to the IWCs measured by the Convair at higher levels and overall, the erroneous ice classifications nonetheless caused a gross under-representation of LWCs in the layer with temperatures above $+5^{\circ}$C. To recover more representative precipitation LWC values in the warm-layer Convair data, a procedure was developed -- and deemed acceptable by the Convair PI (P. Hobbs, personal communication, 2002) -- where the ice artifacts were converted to equivalent-sized liquid water spheres. For this conversion, the four ice habit concentrations (graupel, aggregates, needle/columns, and indeterminate) and the spherical habit (proxy for liquid) concentrations were summed for each Convair segment where the outside air temperature was $> +5^{\circ}$C. The $+5^{\circ}$C threshold was chosen in part because radar-detected bright (melting) bands generally reside in the 0 to $+5^{\circ}$C layer (Pruppacher and Klett, 1997). Furthermore, the hail study of Rassmussen and Heymsfield (1987) and snow research of Mitra et al. (1990) both indicate that ice particles generally persist below the $+5^{\circ}$C level only when the relative humidity in the below-cloud layer is significantly $< 75\%$ and during large hail (> 1.2 cm) events -- neither of which were recorded during KWAJEX. The four ice habit concentrations were then set to zero at temperatures above $+5^{\circ}$C. Thus, the precipitation LWC in g m^{-3} for each of these segments is recalculated using (Pruppacher and Klett, 1997):

$$\mathrm{LWC} = \left(\frac{\pi}{6}\right) \times 10^{-3} \rho_w \int_0^\infty D^3 n(D) dD \approx \left(\frac{\pi}{6}\right) \times 10^{-3} \sum_{i=5\,\mu m}^{25\,mm} D_i^3 n_i \Delta D_i \qquad (10)$$

where r_w is water density in g cm^{-3}, D_i and ΔD_i (bin width) are in mm, and D_i is the diameter corresponding with each of the summed concentrations. The full range of particle sizes -- 5 μm to 25 mm -- is used to calculate the precipitation LWC because this range results in the best comparisons between precipitation LWCs extracted directly from the Convair CMPD and those calculated with the spherical particle concentrations inserted into equation (10). Converting the

ice artifacts in this manner results in the expected ice fraction versus outside air temperature diagram shown in the bottom panel of Figure 15.

Converting the ice artifacts to liquid water spheres not only changes the LWC of the layer where the conversion is performed, but also radically changes the calculated reflectivity and the aforementioned r_e^{wat}/ r_e^{ice} and ν_e^{wat}/ ν_e^{ice} values for that layer. Presumably, more representative rainrate values could be derived from the recalculated liquid water spectra, as well. The effective radii and variances for the $+5^oC$ and warmer layer are recalculated with the converted liquid water spectra using equations (8) and (9), respectively. For Convair temperatures warmer than $+5^oC$, the reflectivity (dBZ) is recalculated with (Doviak and Zrnic, 1993):

$$Z = 10\log_{10}\left[\int_0^\infty n(D)D^6 dD\right] \approx 10\log_{10}\left[\sum_{i=5\,\mu m}^{25mm} 1000n_i\left(\frac{D_i}{1000}\right)^6 \Delta D_i\right] \qquad (11)$$

where D_i and ΔD_i (bin width) are in μm and n_i is concentration in $L^{-1}\,\mu m^{-1}$. Rainrates (mm h^{-1}) for the same layer are calculated using (Doviak and Zrnic, 1993):

$$R = 3.6\times10^7\left(\frac{\pi}{6}\right)\int_0^\infty D^3 n(D)w_t(D)dD \approx 3.6\times10^3\left(\frac{\pi}{6}\right)\sum_{i=5\mu m}^{25mm}\left(\frac{D_i}{10^4}\right)^3 n_i w_{ti}\Delta D_i \qquad (12)$$

where the variables are in the same units as in equation (11) and $w_t(D)$ and w_{ti} represent the drop terminal velocity (m s^{-1}). The drop terminal velocity is estimated from (Atlas et al., 1973):

$$w_t(D) = 9.65 - 10.3\exp(-600D) \qquad (13)$$

where D is the drop size converted into meters. The converted LWCs, reflectivities, effective radii and variances, and derived rainrates are calculated for all Convair CMPD segments and are then subsequently matched to the merged dataset for intercomparison.

Validation of the ice artifact conversion process outlined above is perhaps best represented by the Convair versus PR/2A-25 rainrate and LWC diagrams described and presented in Figure 13 of subsection 3.5. The comparisons would not have been nearly as favorable without ice artifact conversion given that the original matched Convair LWC values were in general 2 orders of magnitude smaller than the converted values. As a further check of both raw CMPD and recalculated Convair values, calculated reflectivities for both the Citation and Convair data are compared to ARMAR measurements in two layers. Figure 16 illustrates scatter diagrams and histograms of layer average ARMAR versus aircraft microphysics-derived reflectivity in the 2-3 km layer (Convair) and 6-7 km layer (Citation). Despite the attenuating effects present in the

ARMAR data -- which are negligible in the 6-7 km layer comparison and fairly small in the 2-3 km layer since rainrates are less than 7 mm h^{-1} -- the comparisons exhibit similarity in the nearly 1-to-1 relationships in the scatter diagrams and similar shapes and peaks in the histograms. The 6-7 km layer comparison using reflectivity directly from the CMPD suggests the Citation did not produce erroneous measurements of ice concentrations due to drop splashing. The ARMAR values slightly exceed the Citation values in the 6-7 km layer and slightly underestimate the Convair values in the 2-3 km layer -- this is attributed to the attenuating effects on the ARMAR measurements noted above.

A summary of all superpixels with matched aircraft microphysical data is included for reference as Appendix 3, in which the sequence number, latitude/longitude, and aircraft designation (DC-8, Citation, or Convair) are tabulated for matched superpixels.

4.0 Analysis

In accordance with the methodology laid out in subsections 2.3 and 2.4, the results presented in this section are divided along two general lines of inquiry: (1) identifying algorithm discrepancies, and (2) deducing an appropriate algorithm reformulation. Differences between the algorithm microphysics and observed microphysics that demonstrate the validity of the hypothesis are discussed in subsection 4.1. Subsection 4.2 offers two approaches for mitigating the weaknesses noted in the model-derived microphysics.

4.1 Algorithm Discrepancies

As outlined in the methodology section, observed minus assumed microphysical differences are investigated as both total column differences and level-specific differences. Figures 17a and 17b illustrate scatter diagram comparisons of the LWC and IWC observations from the individual aircraft versus the closest time/space matched 2A-12 retrievals. The figures also delineate the degree of difference between GV-radar and synthesized 2A-12 rainrates, where red points indicate the greatest differences, green points the least, and blue points insignificant or indeterminate (no radar match) differences. While the matched points (superpixels) shown in Figures 17a and 17b include a wider range of *E-S* values than found in the total column microphysical observations (see Figure 14), they are still predominately stratiform in nature with rainrates less than 7 mm h^{-1}. With predominately medium to low rainrates available for comparison, it is difficult to discern in this case the relationship between the observed-assumed microphysical and radar-model rainrate differences. What is clear, however, is that despite the relatively small range of variation across the match-up points, there is a great deal of variability in the observed low-level (Convair) precipitation LWCs and observed IWCs at all levels that is not present in the assumed model profiles.

An inspection of 2A-12 rainrates plotted versus GV-radar rainrates at the 142 matched total column superpixels (center plot of Figure 18), reveals that while the 2A-12 rainrates generally underestimate the GV-radar rainrates, a rainrate difference of 2 mm h^{-1} or more was exceeded at only 23 of the match-ups. Restricting the rainrate difference analysis to these points highlights the expected trend of increasing observed-assumed microphysical differences with increasing radar-algorithm rainrate differences. Absolute observed-assumed column average microphysical differences versus radar-algorithm rainrate differences are plotted for the six column average microphysical parameters in the graphs surrounding the central scatter diagram of Figure 18.

The linear regression trend lines included in the diagrams indicate a hypothesis-supporting, positive slope in the microphysical versus rainrate difference relationship, except in the case of effective water variance where the relationship is virtually constant. This result for total column microphysical points cannot alone be considered conclusive, given that the matched points cover only a restricted portion of the *E-S* space under consideration and make up less than 0.5% of the total number of KWAJEX superpixels.

Figures 11a and 11b had indicated there are areas where the 2A-12 rainrate retrievals and the GV-radar rainrates differ by much more than 2 mm h^{-1} -- in some cases by as much as 15 mm h^{-1} over significant numbers of superpixels. By mapping the GV-radar, synthesized 2A-25, and synthesized 2A-12 rainrate surfaces into *E-S* coordinate space, rainrate discrepancies beyond just magnitude differences become apparent. Figure 19 illustrates smoothed surfaces of near-surface rainrates derived from the GV-radar and synthesized 2A-25 and 2A-12 algorithms. While all three rainrate surfaces are similar in the approximate *E-S* region where most aircraft *in situ* measurements occur, and the GV-radar and 2A-25 surfaces are similar throughout *E-S* space, the 2A-12 rainrates deviate significantly from the radar rainrates at high emission superpixels. This algorithm deviation takes the form of positive GV-radar minus 2A-12 rainrate differences at high emission, high scattering (hereafter hi-emission/hi-scattering) points, and strongly negative differences at high emission, low scattering (hi-emission/lo-scattering) points. Before postulating why the 2A-12 algorithm seems unable to match Tbs exhibiting hi-emission/hi-scattering characteristics to high rainrate (hereafter hi-rainrate) profiles while producing profiles with too much rain for hi-emission/lo-scattering Tbs, microphysical differences in the areas of significant rainrate differences are first examined.

To obtain microphysical observations in the *E-S* regions that the aircraft tracks avoided and where the greatest radar-algorithm rainrate differences exist, proxy *in situ* LWC profiles are created using the well-correlated synthesized PR to Convair microphysics relationship described in subsection 3.5 (see Figure 13). The 1-2 km layer average LWC values obtained from applying a M-P distribution to the 2A-25 reflectivity/rainrate profiles are then compared to the matching 1-2 km layer average 2A-12 LWC values. Ice water contents are not calculated in a parallel procedure because additional assumptions would be required to produce IWCs from rainrate profiles alone. In a manner similar to that used for the total column microphysical comparisons (Figure 18), the absolute LWC differences are plotted versus the matched near-

surface GV-radar minus 2A-12 rainrate differences for hi-emission/hi-scattering points with rainrate differences > 2 mm h^{-1} and for hi-emission/lo-scattering points with > 5 mm h[1] rainrate differences. These two diagrams, plus diagrams of the associated 2A-12 versus 2A-25 LWCs in the two *E-S* quadrants under study (*E*-index > 0.5, *S*-index > 0.5 and *E*-index > 0.5, *S*-index < 0.5) are depicted in Figure 20. The LWC/rainrate difference analysis diagrams (left side panels in Fig. 20) exhibit increasing LWC differences with increasing rainrate differences. As would be expected from the rainrate differences shown in Figure 19, the right panels of Figure 20 indicate that the 2A-25 LWCs exceed the 2A-12 LWCs in the hi-emission/hi-scattering quadrant, with the opposite being true in the hi-emission/lo-scattering quadrant. The results illustrated in Figure 20, coupled with the earlier results appearing in Figure 18 are taken as conclusive evidence of the validity of the hypothesis of observed-assumed microphysical differences being positively correlated to the GV-radar minus 2A-12 algorithm rainrate differences.

To provide a better understanding of why the 2A-12 hi-emission rainrates appear to overemphasize lo-scattering areas and suppress rainrates in hi-scattering regions, observed and assumed LWC and IWC profiles are matched, plotted and compared. Figure 21a illustrates assumed 2A-12 and aircraft measured LWCs/IWCs plotted at aircraft altitudes and matched to the closest of the 14 model profile levels. The curves running through the data scatter in each diagram are layer-by-layer averages smoothed by cubic spline interpolation, representing the composite assumed and observed profiles shown in Figure 21b. The most salient feature in the composite profiles of Figures 21a and 21b is the significantly greater liquid and ice hydrometeor masses in the observed profiles below 10 km. Above 10 km, the assumed IWCs slightly exceed the values observed by the DC-8; as of now it is not understood why these systematic differences switch signs at high altitude. Also of note is the existence of a small, but significant concentration of presumably supercooled liquid precipitation hydrometeors as high as 9.5 km (measured only by the Citation). Stith et al. (2002) also reported small, but persistent supercooled water concentrations in the Citation KWAJEX measurements.

The consequence of additional mixed layer ice in the observed composite profile is the greater scattering of upwelling microwave radiation than is being reproduced in the cloud-radiation model database. Although the observed composite IWC profile results from predominately stratiform (lo-emission/lo-scattering) superpixels, if the same "factor-of-three" IWC underestimate is assumed for the 2A-12 hi-emission/hi-scattering points, an explanation of

why the algorithm matches highly scattered Tbs to hi-emission/lo-scattering and thus hi-rainrate profiles, can be offered. The presumption that the cloud-radiation model database's underestimate of mixed layer ice at lo-emission superpixels can be assumed for the hi-emission superpixels where no *in situ* measurements were made is supported by the variation of 2A-12 rainrates in the lo-emission region. Since 2A-12's rainrates drop as scattering increases in the hi-emission region, one would expect a decrease in algorithm rainrates with increasing scattering in the lo-emission (*E*-index < 0.5) region as well -- if the aircraft-documented lack of 2A-12 mixed layer ice is truly a contributor to the inverse rainrate relationship. Inspection of the 2A-12 rainrate surface shown in Figure 19 indicates lo-emission rainrates actually increase with increased scattering. However, this is really more a result of the modifying effects of the convective fraction specification (see subsection 3.4) than the actual output of 2A-12's Tb matching and profile selection process.

Figure 22 is a depiction of how 2A-12's unmodified rainrates are modified by the convective fraction specification. The middle panel in Figure 22 shows the convective fraction surface plotted in *E-S* coordinates -- note the values are nearly constant across all scattering values and near maximum in hi-emission areas, while they increase dramatically from near 0 to 1 from lo- to hi-scattering in the lo-emission region. Thus, in hi-emission regions the convective fraction acts to increase rainrates across all scattering values, but not to reverse the reduction in rainrates from lo- to hi- scattering values. In the lo-emission region, rainrates are increased at hi-scattering values but left nearly unchanged at lo-scattering values -- an effect that could reverse a rainrate reduction from lo- to hi-scattering to an increase. The upper panel in Figure 22 is the 2A-12 rainrate surface before modification by the convective fraction (courtesy S. Yang, personal communication, 2002). Note that the lo-emission rainrates do in fact decrease slightly from lo- to hi-scattering values as expected -- given the analyzed mixed layer ice discrepancies.

In summary, the 2A-12 algorithm, derived from synthesized KWAJEX TMI Tbs, underestimates GV-radar and synthesized PR rainrates by ~50% at rainrates < 7 mm h^{-1}, and overestimates GV-radar and PR rainrates by nearly 67% at rainrates ≥ 7 mm h^{-1}. Examination of the 2A-12 rainrates in *E-S* coordinates reveals most of the overestimation occurs at hi-emission/lo-scattering superpixels, while the radar-derived rainrates indicate that 2A-12 significantly underestimates rainrates at convective, hi-emission/hi-scattering points. It is concluded the apparent underproduction of mixed layer ice by the 2A-12 cloud-radiation model

suppresses the number of hi-scattering, hi-rainrate database profiles and forces the algorithm's Bayesian matching scheme to match hi-emission/hi-scattering Tbs (saturated or nearly saturated low frequency channels and depressed high frequency channels) to hi-emission/lo-scattering profiles (highly saturated low frequency channels and non-depressed high frequency channels).

4.2 Algorithm Reformulation

Two possible modifications are offered to mitigate the effects of the mixed layer ice hydrometeor shortage in the cloud-radiation model database profiles. A "simple" procedure is first outlined involving the modification of the convective fraction specification, then a more "microphysically satisfying" procedure addressing ice parameterization in the cloud-radiation model is suggested.

As illustrated in Figure 22, the convective fraction specification has a profound effect on the 2A-12 rainrate retrievals. The algorithm convective fraction specification not only enhances the rainrates in proportion to its fractional value at individual superpixels, but additionally augments the profile microphysics. Since the rainrate at each superpixel is nonlinearly related to the microphysical profile that supports it and produces the microwave Tbs viewed from space (Kummerow, 1998), adjusting the microphysical profile in proportion to changes in the surface rainrate introduces microphysical errors. Nonetheless, one can see that adjusting the convective fraction surface to de-emphasize the enhancement at lo-scattering (S-index < 0.5) and further augment the enhancement in hi-scattering areas could bring the 2A-12 surface rainrate values more in line with the GV-radar and 2A-25 rainrates in E-S space. Mathematically, the convective fraction values could be reduced at hi-emission values by modifying the emission input to the CSI in equation (2). While such an adjustment would do little to correct the apparent mixed layer ice hydrometeor deficit in the profile database, it would offer some improvement to the low-level LWC values and would circumvent having to re-parameterize the cloud-radiation model ice physics and repopulate the database profiles and Tbs. In essence, this would comprise the "simple" modification.

The more microphysically-based modification would be to improve the 7-category numerical modeling simulation microphysical parameterization scheme used to generate the 2A-12 cloud-radiation database. In such parameterizations, up to six hydrometeor categories have been represented (i.e., cloud droplets, precipitating water drops, pristine ice crystals, snow, aggregates, and graupel/hail). Water vapor is the seventh, non-hydrometeor, water category. As

evident in Figures 17a-b and Figures 21a-b, both water and ice contents are under-represented at levels below 10 km in the cloud-radiation model database. This suggests the most significant parameterization problem may be the mass transfer of vapor into the various allowed hydrometeor categories rather than the mass transfers between specific ice habits and liquid water categories.

An example of how the water vapor mass transfer parameterization could be linked to the modeled deficiencies of both liquid and ice hydrometeors is shown in Figure 23. This schematic, in the context of the UW-NMS model and the associated Colorado State University Regional Atmospheric Mesoscale Model (CSU-RAMS) cloud microphysics module (described in Flatau et al., 1989), depicts microphysical water transfer processes amongst six hydrometeor categories. The diagram indicates that, in general, the modeled mass transfers begin with condensation/deposition from vapor to cloud droplets and pristine ice crystals at the top and proceed downward to larger hydrometeors through collection, riming, autoconversion, and additional condensation/deposition. While there are numerous mass transfer interactions between the various categories, with various transfers ignored or not allowed (as noted in the figure legend), it is clear that the modeled production of all liquid and ice hydrometeors would be suppressed if the efficiency of the initial nucleation processes of drop and crystal formation, and the respective deposition growths, are underestimated. It is further noted that despite the 2A-12 cloud-radiation model's parameterization differences from those illustrated in Figure 23, that the early vapor-to droplet and vapor-to-crystal exchanges are fundamental and common to any reasonable parameterization scheme.

Finally, recognizing that in order to be representative, the radiative transfer calculations used to generate the microphysics profile database Tbs must be sensitive to specific ice habits and ice water paths, particularly with respect to the larger particles. Therefore, any improvements to the microphysical parameterization scheme must include emphasis on graupel production throughout all relevant mass transfers leading to graupel. The *in situ* aircraft measurements analyzed here indicate that graupel is the dominant ice habit in the mixed phase layer. This is emphasized in Figure 24 which illustrates the variation in height of the total IWC fraction of the various aircraft-measured ice habits -- graupel being the largest fraction below 9.5 km and making up nearly 70% of the total IWC in the 1500 m layer above the melting layer.

5.0 Conclusions

This investigation has found that the differences between *in situ* measured microphysics and 2A-12 algorithm-assumed profile microphysics are greatest where the algorithm's surface rainrates differ most from rainrates derived from the KWAJEX ground validation radar rainrates, as well as synthesized 2A-25 rainrates. In addition to verifying the hypothesis which motivates this research, the analysis also accomplishes the following: (1) demonstrates the usefulness of a 2-dimensional emission-scattering framework (*E-S* coordinate system) in intercomparing radar- and radiometer-derived microphysics and rain measurements; (2) identifies and quantifies ice deficiencies in the current version of the 2A-12 TRMM facility algorithm (Version 5); (3) proposes modifications to the 2A-12 algorithm that would mitigate its shortcomings vis-à-vis microphysical assumptions; (4) diagnoses the strengths of a downward-looking radar in validating a radiometer rain algorithm; and (5) quantifies the limitations in using manned aircraft for exploring the complete microphysical domain of precipitating clouds.

The *E-S* coordinate system proves to be effective in uncovering the tendency of the 2A-12 algorithm to match hi-emission/hi-scattering brightness temperature signatures with hi-emission/lo-scattering assumed cloud-radiation model generated database profiles.   The *E-S* coordinate diagrams show clearly the similarity between the GV-radar-derived and synthesized PR-derived rainrate surfaces in *E-S* space, and provide an excellent contrasting depiction of the concomitant 2A-12 rainrate surface for isolating differences. It is worth noting that, generally, the *E-S* coordinate system is more effective than a combination of matched superpixel plots, scatter diagrams, and histograms for isolating algorithm problems in conjunction with the assumed microphysics.

The mismatching by 2A-12 of hi-rainrate/hi-scattering microphysical profiles into hi-emission/lo-scattering profiles is shown to be traceable to an apparent shortage of scattering mixed-layer ice hydrometeors in the cloud-radiation model simulations used to populate the algorithm database. Analysis of the *in situ* observations indicates that the assumed profile mixed-layer IWCs and low-level LWCs are as much as three times too low in generally stratiform cases, i.e., those cases which the aircraft largely interrogated.   The aircraft measurements additionally show that graupel hydrometeors comprise nearly 70% of the IWC in the lowest regions of the mixed-layer where the greatest observed minus assumed IWC differences occur.

Two algorithm modifications are proposed to reduce the observed-assumed rainrate and microphysical differences. First, a "simple" modification involving a change to the current 2A-12 convective fraction specification is suggested. This modification would be straight-forward to implement and would improve the rainrate match-up in magnitude and *E-S* space. By the same token, it would do little to rectify underlying ice microphysics problems in the cloud-radiation model simulations. The second, more physically-based modification requires that the microphysical parameterization scheme of the cloud model be improved to better characterize liquid and ice water contents for levels below 10 km -- but especially IWCs within the mixed-phase layer due to graupel. Such a modification would then require an updated 2A-12 cloud-radiation model database to be compiled.

This study provides evidence that downward-looking radars, such as the TRMM PR or the aircraft-deployed ARMAR system, best produce the vertical resolution required for meaningful microphysical intercomparisons. The implication here is that future field campaigns organized to validate spaceborne radiometers should always make use of downward-looking radars for optimal algorithm validation analysis.

Analysis of the KWAJEX field campaign data reveals that aviation safety concerns resulting from using manned research aircraft have been, and will continue to be, a major limitation in the collection of *in situ* microphysical measurements across the full spectrum of precipitation phenomena. Although the aircraft priority leg microphysical data obtained during KWAJEX and analyzed for this research could not have been obtained with balloon-sondes, dropsondes, or rocketsondes, (and thus were invaluable to the conclusions that have been reached), they were seriously limited flight tracks insofar as many of the strong action zones of precipitating clouds are off limits to pilots. Therefore, it is advisable that similar future campaigns examine new ways to equip and utilize remotely-controlled drone aircraft, other unmanned aerial vehicles (UAVs), and elevated mountain terrains to collect *in situ* microphysical data.

These last remarks should not be taken as wholesale criticism of the use of manned aircraft for probing the microphysics of precipitating clouds. Whereas Figure 19 shows very clearly that the KWAJEX aircraft tracks restricted themselves to only one of the four major quadrants of microphysical E-S space, i.e., the lo-emission/lo-scattering quadrant, it is that very quadrant where a great deal of mid- to light-rainfall occurs. As various past studies have noted, this is

perhaps the most difficult of the retrieval regimes for both space-viewing radiometers and radars, e.g., see Smith et al. (1998) and Meneghini et al. (2000). Therefore, it should be stressed that the major role for manned aircraft in studies of precipitation microphysics and in validation campaigns for precipitation algorithms, is within the low-mid to light rain regimes where modern algorithms have had difficulty in detection of precipitation and quantization of rainrates. Manned aircraft are simply not going to be useful in gathering *in situ* microphysical data within intense rainfall regimes, and future field experiments need to account for that in their *a priori* strategies and planning.

As noted in the introductory paragraphs, the analyses completed for this research offer the most fundamental, physically-based validation of the TRMM radiometer-only facility algorithm to date -- a detailed three-dimensional intercomparison of the algorithm's assumed profile microphysics with *in situ*, GV-radar, and airborne-radar derived microphysics. The intercomparisons have exposed the algorithm's most prominent weaknesses -- the ice water content within the mixed phase layer and inconsistencies concerning the specification of convective fraction in conjunction with implied rainrates and microphysical properties. Notwithstanding the possibility that the diagnosis performed on microphysical weaknesses could be in part due to inaccuracies arising from the synthesis of TMI brightness temperatures from AMPR measurements and further inaccuracies intrinsic to the time-space match-up procedures -- this analysis has arrived at conclusions that justify algorithm modifications in specific components of the 2A-12 algorithm that have been historically suspect (C. Kummerow, personal communication, 2002). In this context, it is important to note that the results shown in Figure 21b exhibit discrepancies between microphysical observations and algorithm assumptions that deserve careful scrutiny by others, particularly the producers of the 2A-12 algorithm. Furthermore, the results shown in Figure 22 are persuasive in quantifying how sensitive 2A-12 retrievals are to the specification of convective fraction -- a parameter that is directly linked to the algorithm's underlying microphysical assumptions and thus directly to the algorithm's rainfall outcomes.

The principle expected benefit of physically-based improvement to the TRMM radiometer algorithm is the development of more accurate, instantaneous retrievals of rainrates and associated microphysical profiles from space. This will provide a better understanding of how tropical/subtropical water budgets at large scales build up from micro- and mesoscale cloud and

precipitation processes (Hou et al., 2000). Such results address a core objective of TRMM, which is to produce highly representative rainfall climatologies from physically-based and objectively-validated retrieval algorithms. Furthermore, the successor to TRMM, the Global Precipitation Measurement (GPM) mission, is expected to launch a globe-encircling fleet of satellites each carrying a passive microwave radiometer. With enhanced retrieval algorithms, such a constellation will provide complete and continuous coverage and relatively accurate determination of one of the atmosphere's most important meteorological variables.

6.0 Acknowledgements

7.0 References

Adler, R. F., G. J. Huffman, and P. R. Keehn, 1994: Global tropical rain estimates from microwave adjusted geosynchronous IR data. *Rem. Sens. Rev.*, **11**, 125-152.

Atlas, D., R. C. Srivastava, and R. S. Sekhon, 1973: Doppler radar characteristics of precipitation at vertical incidence. *Rev. Geophys. Space Phys.*, **2**, 1-35.

Doviak R. J., and D. S. Zrnic, 1993: *Doppler Radar and Weather Observation (*2nd ed.). Academic Press, 458 pp.

Evans, K. F., J. Turk, T. Wong, and G. L. Stephens, 1995: A Bayesian approach to microwave precipitation profile retrieval. *J. Appl. Meteorol.*, **34**, 260-279.

Farrar, M. R., E. A. Smith, 1992: Spatial resolution enhancement of terrestrial features using deconvolved SSM/I microwave brightness temperatures. *IEEE Trans. Geosci. Rem. Sens.*, **30**, 349-355.

Farrar, M.R., E. A. Smith, and X. Xiang, 1994: The impact of spatial resolution enhancement of SMM/I microwave brightness temperatures on rainfall retrieval algorithms. *J. Appl. Meteor.*, **33**, 313-333.

Ferraro, R. R., and G. F. Marks, 1995: The development of SSM/I rain-rate retrieval algorithms using ground based radar measurements. *J. Atmos. Oceanic Tech.*, **12**, 755-770.

Flatau P. J., G. J. Tripoli, J. Verlinde, and W. R. Cotton, 1989: The CSU-RAMS cloud microphysical module: general theory and code documentation. Paper No. 451, Dept. of Atmospheric Science, Colorado State University, Fort Collins, CO.

Haddad, Z. S., E. A. Smith, C. D. Kummerow, T. Iguchi, M. R. Farrar, S. L. Durden, M. Alves, and W. S. Olson, 1997: The TRMM "Day-1" radar/radiometer combined rain-profiling algorithm. *J. Meteor. Soc. Japan*, **75**, 799-809.

Hagen, M., and S. E. Yuter, 2002: Relations between radar reflectivity, liquid water content, and rainfall rate during the MAP-SOP. *Quart. J. Roy. Meteor. Soc.*, conditionally accepted.

Heymsfield, A. J., A. Bansemer, P. R. Field, S. L. Durden, J. Stith, J. E. Dye, W. Hall and T. Grainger, 2002: Observations and parameterizations of particle size distributions in deep tropical cirrus and stratiform precipitating clouds: Results from *in-situ* observations in TRMM field campaigns. *J. Atmos. Sci.*, in press.

Hitschfeld, W., J. Bordan, 1954: Errors inherent in the radar measurement of rainfall at attenuating wavelengths. *J. Atmos. Sci.*, **11**, 58–67.

Hong, Y., C. D. Kummerow, and W. S. Olson, 1998: Separation of convective and stratiform precipitation using microwave brightness temperature. *J. Appl. Meteor.*, **38**, 1195-1213.

Hou, A. Y., S. Q. Zhang, A. M. da Silva, W. S. Olson, 2000: Improving assimilated global datasets using TMI rainfall and columnar moisture observations. *J. Climate*: **13**, 4180–4195.

Iguchi, T., and R. Meneghini, 1994: Intercomparison of single-frequency methods for retrieving a vertical rain profile from airborne or spaceborne radar data. *J. Atmos. Oceanic Tech.*, **11**, 1507-1511.

Iguchi, T., T. Kozu, R. Meneghini, J. Awaka, and K. Okamoto, 2000: Rain-profiling algorithm for the TRMM precipitation radar. *J. Appl. Meteorol.*, **39**, 2038-2052.

Kidder, S. Q., and T. H. Vonder Haar, 1995: *Satellite Meteorology: An Introduction.* Academic Press, 466 pp.

Kummerow, C. D., R. A. Mack, and I. M. Hakkarinen, 1989: A self consistency approach to improve microwave rainfall rate estimation from space. *J. Appl. Meteor.*, **28**, 869-884.

Kummerow, C. D., W.S. Olson, and L. Giglio, 1996: A simplified scheme for obtaining precipitation and vertical hydrometeor profiles from passive microwave sensors. *IEEE Trans. Geosci. Rem. Sens.*, **34**, 1213-1232.

Kummerow, C. D., 1998: Beamfilling errors in passive microwave rain retrievals. *J. Appl. Meteor.*, **37**, 1837-1858.

Kummerow, C., W. Barnes, T. Kozu, J. Shiue, and J. Simpson, 1998: The Tropical Rainfall Measuring Mission (TRMM) sensor package. *J. Atmos. Oceanic Tech.*, **15**, 809-817.

Kummerow, C., and K. Okamoto, 1999: Space-borne remote sensing of precipitation from TRMM. *Rev. Radio Sci.* (1996-1999), Oxford Univ. Press, 487-502.

Liu, G., and J. A. Curry, 1992: Retrieval of precipitation from satellite microwave measurement using both emission and scattering. *J. Geophys. Res.*, **97**, 9959-9974.

Liu, G., and J. A. Curry, 1998: An investigation of the relationship between emission and scattering signals in SSM/I data. *J. Atmos. Sci.*, **55**, 1628-1643.

Marshall, J.S., W. McK. Palmer, 1948: The distribution of raindrops with size. *J. Atmos. Sci.,* **5**, 165–166.

Meneghini, R., T. Iguchi, T. Kozu, L. Liao, K. Okamoto, J. Jones, and J. Kwiatkowski, 2000: Use of the surface reference technique for path attenuation estimates from the TRMM Precipitation Radar. *J. Appl. Meteorol.*, **39**, 2053-2070.

Mitra, S. K., O. Vohl, M. Ahr, H. R. Pruppacher, 1990: A wind tunnel and theoretical study of the melting behavior of atmospheric ice particles. IV: Experiment and theory for snow flakes. *J. Atmos. Sci.,* **47**, 584–591.

Mugnai, A., and E. A, Smith, 1988: Radiative transfer to space through a precipitating cloud at multiple microwave frequencies. Part I: Model description. *J. Appl. Meteor.*, **27**, 1055-1073.

Mugnai, A., H. J. Cooper, E. A. Smith, and G. J. Tripoli, 1990: Simulation of microwave brightness temperatures of an evolving hail storm at SSM/I frequencies. *Bull. Amer. Meteor. Soc.*, **71**, 2-13.

Mugnai, A., E. A. Smith, and G. J. Tripoli, 1993: Foundations for statistical-physical precipitation retrieval from passive microwave satellite measurements. Part II: Emission source and generalized weighting function properties of a time dependent cloud radiation model. *J. Appl. Meteor.*, **32**, 17-39.

Olson, W. S., 1989: Physical retrieval of rainfall rates over the ocean by multispectral microwave radiometry: Application to tropical cyclones. *J. Geophys. Res.*, **74**, 2269-2280.

Pruppacher, H. R., and J. D. Klett, 1997: *Microphysics of Clouds and Precipitation*. Kluwer Academic Publishers, 954 pp.

Rasmussen, R. M., A. J. Heymsfield, 1987: Melting and shedding of graupel and hail. Part III: Investigation of the role of shed drops as hail embryos in the 1 August CCOPE Severe Storm. *J. Atmos. Sci.*, **44**, 2783–2803.

Smith, E. A., and A. Mugnai, 1988: Radiative transfer to space through a precipitating cloud at multiple microwave frequencies. Part II: Results and analysis. *J. Appl. Meteor.*, **27**, 1074-1091.

Smith, E. A., and A. Mugnai, 1989: Radiative transfer to space through a precipitating cloud at multiple microwave frequencies. Part III: Influence of large ice particles. *J. Meteor. Soc. Japan*, **67**, 739-755.

Smith, E. A., A. Mugnai, H. J. Cooper, G. J. Tripoli, and X. Xiang, 1992: Foundations for statistical-physical precipitation retrieval from passive microwave satellite measurements. Part I: Brightness temperature properties of a time dependent cloud-radiation model. *J. Appl. Meteor.*, **31**, 506-531.

Smith, E. A., X. Xiang, A. Mugnai, and G. J. Tripoli, 1994a: Design of an inversion-based precipitation profile retrieval algorithm using an explicit cloud model for initial guess microphysics. *Meteor. Atmos. Phys.*, **54**, 53-78.

Smith, E. A., A. Mugnai, G. J. Tripoli, 1994b: Theoretical foundations and verification of a multispectral, inversion-type microwave precipitation profile retrieval algorithm. *Proceedings of ESA/NASA International Workshop on Microwave Radiometry*, VSP Science Press, Utrecht – The Netherlands, 599-621.

Smith, E. A., C. Kummerow, and A. Mugnai, 1994c: The emergence of inversion-type precipitation profile algorithms for estimation of precipitation from satellite microwave measurements. *Remote Sensing Reviews*, **11**, 211-242.

Smith, E. A., X. Xiang, A. Mugnai, R. Hood, and R. W. Spencer, 1994d: Behavior of an an inversion-based precipitation retrieval algorithm with high resolution AMPR measurements including a low frequency 10.7 GHz channel. *J. Atmos. Oceanic Tech.*, **11**, 858-873.

Smith, E. A., F. J. Turk, M. R. Farrar, A Mugnai, X. Xiang, 1997: Estimating 13.8 GHz path integrated attenuation from 10.7 GHz brightness temperatures for TRMM combined PR-TMI precipitation algorithm. *J. Appl. Meteor.*, **36**, 365-388.

Smith, E.A., J. Lamm, R. Adler, J. Alishouse, K. Aonashi, E. Barrett, P. Bauer, W. Berg, A. Chang, R. Ferraro, J. Ferriday, S. Goodman, N. Grody, C. Kidd, D. Kniveton, C. Kummerow, G. Liu, F. Marzano, A. Mugnai, W. Olson, G. Petty, A. Shibata, R. Spencer, F. Wentz, T. Wilheit, and E. Zipser, 1998: Results of WetNet PIP-2 project. *J. Atmos. Sci.*, **55**, 1483-1536.

Smith, E. A., 1999: Use of TRMM field campaign data for validation-application studies with level 2 rain profile algorithms. Proposal to NASA Research Announcement 99-OES-03, Dept. of Meteorology, Florida State Univ., Tallahassee, FL.

Spencer, R. W., H. M. Goodman, R. E. Hood, 1989: Precipitation retrieval over land and ocean with the SSM/I: Identification and characteristics of the scattering signal. *J. Atmos. Oceanic Tech.* **6**, 254–273.

Spencer, R. W., R. E. Hood. F. J. LaFontaine. E. A. Smith, J. Galliano, and E. Lobl, 1994: High resolution imaging of rain systems with the Advanced Microwave Precipitation Radiometer. *J. Atmos. Oceanic Tech.*, **11**, 849-857.

Steiner, M., R. A. Houze Jr., S. E. Yuter, 1995: Climatological characterization of three-dimensional storm structure from operational radar and rain gauge data. *J. Appl. Meteor.,* **34**, 1978–2007.

Stith, J. L., J. E. Dye, A. Bansemer, A. J. Heymsfield, C. A. Grainger, W. A. Petersen, R. Cifelli, 2002: Microphysical observations of tropical clouds**.** *J. Appl. Meteor.*, **41**, 97–117.

Tripoli, G. J. 1992a: A nonhydrostatic model designed to simulate scale interactions. *Mon. Wea. Rev.*, **120**, 1342-1359.

Tripoli, G. J. 1992b: An explicit three-dimensional nonhydrostatic numerical simulation of a tropical cyclone. *Meteor. Atmos. Phys.*, **49**, 229-254.

Wilheit, T. T., A. T. C. Chang, M. S. V. Rao, E. B. Rodgers, and J. S. Theon, 1977: A satellite technique for quantitatively mapping rainfall rates over the oceans. *J. Appl. Meteor.,* **16**, 551-560.

Wilheit, T. T., 1986: Some comments on passive microwave measurement of rain. *Bull. Amer. Meteor. Soc.*, **67**, 1226-1232.

Wilheit, T. T., A. T. C. Chang, L. S. Chiu, 1991: Retrieval of monthly rainfall indices from microwave radiometric measurements using probability distribution functions. *J. Atmos. Oceanic Tech.*, **8**, 118-136.

Wilheit, T., R. Adler, S. Avery, E. Barret, P. Bauer, W. Berg, A. Chang, J. Ferriday, N. Grody, S. Goodman, C. Kidd, D. Kniveton, C. Kummerow, A. Mugnai, W. Olson, G. Petty, A. Shibata, E. Smith, and R. Spencer, 1994: Algorithms for the retrieval of rainfall from passive microwave measurements. *Remote Sensing Reviews*, **11**, 163-194.

Xiang, X., E. A. Smith, and C.G. Justus, 1994: A rapid radiative transfer model for reflection of solar radiation. *J. Atmos. Sci*., **51**, 1978-1988.

Yuter, S. E., R. A. Houze Jr., 1997: Measurements of raindrop size distributions over the Pacific warm pool and implications for *Z–R* relations. *J. Appl. Meteor.,* **36**, No. 7, pp. 847–867.

8.0 Appendix 1: Description of *E-S* Coordinate System

Plain Language Formulation of E-S Index

Emission Index (10.7 & 19.35 GHz Tbs)

1. Calculate initial E-index based on 10.7 GHz warming.

2. Calculate E-index enhancement multiplier based on 19.35 GHz warming.

3. Assume 19.35 GHz saturation if: Tb10.7 or Tb19 > 275 K .

Scattering Index (37.0 & 85.5 GHz Tbs)

1. Calculate initial S-index based on relative relationship between 19.35 and 37.0 GHz Tbs, in which there are four (4) possibilities:

    i.   no scattering (low Tb19 / low Tb37)
    ii.   low level scattering (low Tb19 / Tb37 warms)
    iii.   moderate scattering (Tb19 warms / Tb37 > Tb_{CUT})
    iv.   heavy scattering (Tb19 warms / TB37 < Tb_{CUT})

2. Calculate S-index enhancement based on depression in Tb85.

3. Assume 37.0 GHz depression if: Tb19 warms & Tb37 < 260 K .

Establish Threshold Definitions: To maximize the spread of *E-S* points, maximum emission channel Tb thresholds (10.7 & 19.35 GHz) should be set just below the maximum Tbs measured in the dataset under consideration. The minimum emission channel Tb threshold should be set at or just above the 10.7 and 19.35 GHz Tb distribution peaks -- this tunes the *E*-index for precipitation-sized hydrometeors. Minimum and maximum scattering channel (37.0 and 85.5 GHz) Tb thresholds should be set close to the minimum and maximum Tbs measured in the dataset for those particular channels.

Emission Index Calculation: There are three steps: Step (1) calculate the initial *E*-index based on 10.7 GHz warming; Step (2) calculate *E*-index enhancement multiplier based on 19.35 GHz warming; and Step (3) assume 19.35 GHz saturation if Tb10 or Tb19 > 275 K.

Scattering Index Calculation: There are also three steps, but step one has four conditions: Step (1) calculate the initial *S*-index based on the relative relationship between 19.35 and 37.0 GHz Tbs by considering four possibilities:

> (a) no scattering (low Tb19 / low Tb37)
> (b) low scattering (low Tb19 / Tb37 warms)
> (c) moderate scattering (Tb19 warms / Tb37 > $Tb37_{CUT}$)
> (d) heavy scattering (Tb19 warms / Tb37 < $Tb37_{CUT}$)

Step (2) calculate the *S*-index enhancement based on the depression in Tb85; Step (3) assume 37.0 GHz depression if Tb19 warms and Tb37 < 260 K.

A listing of pseudo FORTRAN code for this procedure follows.

Appendix 1: Continued.

Pseudo FORTRAN Code for Calculation *E-S* Indices

```
INTEGER SATFAC, DEPFAC

C Bound and Threshold Definitions

TB10MAX = 280
TB19MAX = 280
TB37MAX = 285
TB85MAX = 290
TB10MIN = 150
TB19MIN = 200
TB37MIN = 230
TB85MIN = 140
TBSAT = 275
TBDEP = 260

C Set Brightness Temperature Bounds

IF (TB10.LT.0) TB10 = 0
IF (TB19.LT.0) TB19 = 0
IF (TB37.LT.0) TB37 = 0
IF (TB85.LT.0) TB85 = 0
IF (TB10.GT.TB10MAX) TB10 = TB10MAX
IF (TB19.GT.TB19MAX) TB19 = TB19MAX
IF (TB37.GT.TB37MAX) TB37 = TB37MAX
IF (TB85.GT.TB85MAX) TB85 = TB85MAX

C Determine Emission Index (EIND) & 19 GHz Saturation Factor (SATFAC)

EIND = 0
ESCL = 1
IF (TB10.GE.TB10MIN)
$ EIND = 0.5 * (TB10-TB10MIN) / (TB10MAX-TB10MIN)
IF (TB19.GE.TB19MIN)
$ ESCL = 1.0 + (TB19-TB19MIN) / (TB19MAX-TB19MIN)
EIND = ESCL * EIND
SATFAC = 0
IF (TB19.GE.TBSAT) SATFAC = 1
IF (TB10.GE.TBSAT) SATFAC = 1

C Determine Scattering Index (SIND) & 37 GHz Depression Factor (DEPFAC)

SIND = 0
SSCL = 1
IF (TB19.LT.TB19MIN.AND.TB37.LT.TB37MIN) SIND = 0.0
IF (TB19.LT.TB19MIN.AND.TB37.GE.TB37MIN)
$ SIND = 0.1 * (TB37MAX – TB37) / (TB37MAX – TB37MIN)
IF (TB19.GE.TB19MIN.AND.TB37.GE.TB37MIN)
$ SIND = 0.5 * (TB37MAX – TB37) / (TB37MAX – TB37MIN)
IF (TB19.GE.TB19MIN.AND.TB37.LT.TB37MIN) SIND = 0.5
IF (TB85.GE.TB85MIN)
$ SSCL = 1.0 + (TB85MAX – TB85) / (TB85MAX – TB85MIN)
IF (TB85.LT.TB85MIN) SSCL = 2.0
SIND = SSCL * SIND
DEPFAC = 0
IF (TB19.GT.TB19MIN.AND.TB37.LT.TBDEP) DEPFAC = 1
```

9.0 Appendix 2: TRMM Common Microphysics Product Definition (CMPD)

[Version 4: January'02]

This document represents Version 4 of the TRMM Common Microphysical Product Definition (CMPD). The CMPD is not a substitute for the flight-level state parameter time series data provided by each aircraft to the TRMM DAAC. Neither is the CMPD the only microphysics data set that will be archived. Three basic types of microphysics products will reside in the DAAC: raw data as recorded onboard the aircraft, CMPD for defined flight legs, and specialized data products which contain detailed information not present in the CMPD.

A. Scientific Objectives

In situ measurements of the vertical profiles of hydrometeors were one of the primary objectives of recent TRMM Field Campaigns (FCs). These data will address key issues related to TRMM Microwave Imager (TMI) and TRMM Precipitation Radar (PR) algorithm designs, algorithm validation, cloud modeling, and generation of ground validation products. During the FCs, aircraft often flew in vertical stacks of up to three aircraft to simultaneously sample the hydrometer content of clouds at different temperatures.

The preliminary goal of microphysical data processing for TRMM Users is to produce a form of the data from the different aircraft and microphysical instruments that can be combined in a straightforward fashion to yield representative vertical profiles of hydrometeors. As much as possible, the data processing should remove the aircraft and instrument dependent aspects of the data to yield datasets from each aircraft that accurately portray the relative differences between the samples obtained at different temperatures. Additionally, the algorithms should be fully documented and available in the public domain so that other investigators will have a known starting point before applying additional corrections to the data.

These preliminary products will represent, by design, the lowest common denominator among the various aircraft instruments used in the FCs. Other more sophisticated and specialized products will be eventually produced by participants in this effort as well as by other TRMM PIs. Most importantly, the needs of the TRMM User community require a dataset that can be combined into vertical hydrometeor profiles by June-2001, and thus these common microphysical products must be given first priority. TRMM has funded Sky Tech Research, Inc to develop software (TRMM Microphysics Software) that will be used by TRMM PI's to generate these products. The Common Microphysical Product will serve as an input to computations of derived variables such as rain rate, brightness temperature, No etc.

B. Schedule

A timetable of decisions and deliverables relevant to the TRMM CMPD is as follows:

Jan 2000:   Complete Version 0.0 of CMPD document.

Feb 2000:   Finalize Version 0.1 of CMPD document, algorithms and ASCII product format. Determine 2-3 *high priority* microphysics legs from each FC to be processed for May 2000-SLC meeting (no more than 30 min of data from each aircraft from each FC). Assign order for processing *high priori* microphysics legs for May-2000 SLC meeting.

May 2000:   Examine *high priority* microphysics legs processed for SLC meeting. Revise to Version 1.0 CMPD document, algorithms and ASCII product format. Determine prioritization of aircraft missions within each FC.

Oct 2000:   Complete definition of *priority* flight legs for product generation in priority order for each FC. Priority flight legs will include approximately 300 min of data from each aircraft from each FC. After interim assessment of User needs, refine to Version 1.1 CMPD document, algorithms and ASCII product format.

Mar 2001   Refine to Version 2 CMPD document and delivery of TRMM Microphysics Software (TMS) software to TRMM PIs.

May 2001   Refine to Version 3 CMPD document.

Sep 2001:   Version 3 processing of all priority legs, approximately 300 minutes of data from each aircraft from each FC, due for delivery to TRMM DAAC.

Jan 2002:   Alter bin widths at particle sizes greater than 1 mm to improve the quality of size and area spectra. Refine to Version 4 CMPD.

C. Lowest Common Denominator Product

The TRMM common microphysics product consists of a time series of variables derived over 1-km sections of flight tracks. For state variables such as temperature, and microphysical variables such as particle size spectra, these will represent 1-km track averages.

Aircraft and Instrumentation

Four different aircraft were used in the FC's:
UND Citation	TEFLUN B/CAMEX, LBA, KWAJEX
NASA DC8	TEFLUN B/CAMEX, KWAJEX
SPEC Lear	TEFLUN A
UW Convair	KWAJEX

Each aircraft was equipped with an array of microphysical instrumentation that included combinations of opto-electrical probes such as the FSSP (Forward Scattering Spectrometer Probe), CPI (Cloud Particle Imager), 2DC (Two-Dimensional Cloud Probe), HVPS (High Volume Particle Sampler), and 2DP (Two-Dimensional Precipitation Probe). The FSSP, CPI, 2DC, and HVPS are designed to sample increasingly larger sizes of hydrometeors with decreasing resolution. Each probe covers a relatively unique size range that can vary depending on the aircraft and FC in question. The 2DP has a slightly better resolution than the HVPS, but has a smaller dynamic sampling range. For the purposes of the CMPD, data from the HVPS will be used to characterize large particles unless that probe was not operating or not deployed on an aircraft; in this event, data from the 2DP will used unless that probe was not operating or not deployed on an aircraft.

In addition to the opto-electrical probes, the Citation, Lear, and Convair were equipped with King (hot-wire) and Rosemount (icing) probes to detect and quantify the presence of cloud liquid water. Finally, all four aircraft recorded navigation (e.g., location, altitude) and state parameter (e.g., temperature, pressure) data.

Flight Leg Definition

A coordinator from each field campaign (G. Heymsfield-TEFLUN A and B/CAMEX, W. Petersen- LBA, S. Yuter-KWAJEX) will specify the latitude-longitude coordinates of the start and end points of the microphysical legs to be processed so that the data from each aircraft can be associated in the vertical. Although the stacked aircraft tracks were usually within a few km in the horizontal, they often were not precisely overlaid. For purposes of the TRMM common microphysics product, the point at which an aircraft passes closest to the defined start point lat-lon is defined as the 0-km coordinate along a flight track. The point closest to the end point lat-lon is defined as within the N km coordinate along the flight track (N is determined as the scalar distance between the start and end points). This method of defining straight and spiral flight tracks will yield integer numbers of kilometers (N_i) for each ith leg.

An example of a proposed flight leg from KWAJEX (Fig. 1, not shown) is as follows: This leg is from the 11 Aug 1999 mission at ~2213-2225 UTC. The Citation & Convair are heading SW. The beginning point is 8.81 deg N/168.10 deg E while end point is 8.23 deg N/167.85 deg E. The flight leg length is ~68 km.

Please note that the defined start and end times may not correspond to the actual start and end times for a specific aircraft, parameters that will be a function of exactly when the aircraft in question passes closest to the defined start and end locations. If an aircraft is executing a turn or another maneuver at the beginning or end of a defined, straight microphysical leg, and the microphysical data collected onboard are not considered to be usable for research purposes, the values of the product variables for the affected km coordinates will be set to missing. Another issue to address is when aircraft are flying in opposite directions along a flight track. In these cases the data file from an aircraft whose track starts with the end point (and ends with the start point) will need to be reversed in time order and then coordinate tagged accordingly. The proposed KWAJEX flight leg from ~2151-2159 UTC during the 19 Aug 1999 mission is an example of this scenario (Fig. 2, not shown). In this flight leg, the DC-8 is moving NE to SW whereas the Citation is on a reverse track heading SW to NE. The beginning point (i.e., the NE end of the leg) is at 8.45 deg N/167.22 deg E while the end point (i.e., the SW end of the leg) is at 8.22 deg N/166.83 deg E. The length of this flight leg is 50 km.

Data from each flight leg will be in a separate file consisting of header information followed by the actual time series data. The file naming convention is based on CMPD Version #, UTC date, experiment name, aircraft name, and total number of 1-km leg segments. The total number of 1 km segments may vary among aircraft for the same defined flight leg as aircraft did not usually fly on identical tracks. Leg start times and segment counts are determined by the field campaign flight leg coordinator and will be accessible from an online web master list. The filename format convention is to be given as:

cmp_vers#_yyyymmddhhmm_expname_acname_totseg#

For example, "cmp_vers4_199908112213_kwajex_cit_68" names a common microphysical product data file using the Version 4 CMPD (versions are now in whole rather than decimal numbers), for an August 11, 1999 KWAJEX flight leg from the Citation with defined leg start time of 2213 and with 68 1-km segments. Although dates alone would be adequate to differentiate between different field campaigns, the field campaign name is incorporated in the file definition to minimize file recognition mistakes by the various classes of Users. Note that "defined leg start time" is a label assigned by the field campaign flight leg coordinator and may or may not correspond to the exact start time of the leg for a particular aircraft.

D. Formats and Definitions

The common microphysical product variables will be given in ASCII format, with all lines ending in a carriage return. The format consists of several header lines followed by lines containing data for each 1-km leg segment.

Header

The 1st header line will contain an integer indicating the total number of header lines (which must NOT be less than 3). The 2nd header line will contain the filename. The 3 rd header line will contain the bin center in μm of each size category in the spectra data. These bin centers are needed to properly plot the particle spectra. Additional header comment lines can be defined by a data provider as long as they are accounted for in the 1st header line. Data providers are STRONGLY encouraged to provide additional information in the comment lines regarding which probes were used to characterize certain sets of bins, the characteristics of probes used in the calculations (e.g., resolution, size range, response time), how size spectra were computed, specifications of mass-dimension relationships, and specifications for thresholds used in habit recognition calculations. The comment lines are also the place where specific "user beware" information regarding the uncertainties of various fields should be placed.

Time series

The time series data will be presented as columns delimited by a blank space, with a carriage return at the end of each line. A value of -999.99 must be used for missing values. Each 1-km segment along a flight track will be represented by 13 lines. The first line will contain fifteen parameter sectors in order, containing 92 fields as follows: time tag (6 fields), position coordinate (4 fields), ambient temperature (1 field), true air speed (1 field), ground speed (1 field) pressure (1 field), dewpoint (1 field), vertical air velocity (1 field), total counts and concentrations (8 fields), habit (45 fields), water/ice masses (13 fields), mass-weighted mean particle size (1 field), reflectivity (1 field), artifacts (2 fields) and spares (6 fields). The second and third lines will contain spectral representations of particle area (90 fields per line). Lines 4-13 will contain spectral representations of particle size (98 fields per line). If any spectra is missing, a value of -999.99 must be placed in all size bins. In this manner, the time tag information for each 1 km along the flight track will appear as the first 6 fields in every 13 th line of the time series data.

Line 1

1. Time Tag: 6 fields containing UTC time at center of 1-km flight track segment (e.g., first time tag indicates time where aircraft is 500 m from start point) -- format is 4-digit year, 2-digit month, 2-digit day, hour, minute, seconds to 1-decimal place accuracy (note leading zeros must be present for 2-digit month, day, hour, and min values).

Example: 1999 08 05 22 15 2.3

2. Position Coordinate: 4 fields total, first two fields contain lat-lon coordinates at center of 1-km flight track segment (e.g., first position coordinate indicates position where aircraft is 500 m from start point) -- format in decimal degrees to 4-decimal place accuracy with north (south) latitudes given as positive (negative) and east (west) longitudes given as positive (negative). Third field contains best measurement of average altitude in meters MSL at center of 1-km flight track segment to nearest meter. Fourth field is a flag indicating source of lat-lon position data (I for INS, G for GPS).

Example: 8.8555 168.1000 5056 G

3. Ambient Temperature: 1 field containing best measurement of average temperature along 1-km flight track segment -- format in deg C to 1 decimal place accuracy.

Example: -2.1

4. True Air Speed: 1 field containing best measurement of average true air speed along 1-km flight track segment -- format in m/s to 1 decimal place accuracy.

Example: 150.3

5. Ground Speed: 1 field containing best measurement of average ground speed along 1-km flight track segment – format in m/s to 1 decimal place accuracy.

Example: 150.3

6. Pressure: 1 field containing best measurement of average pressure along 1-km flight track segment -- format in mb to nearest mb.

Example: 772

7. Dewpoint: 1 field containing best measurement of average dewpoint along 1-km flight track segment -- format in deg C to 1 decimal place accuracy. If data is considered unreliable set to missing.

Example: 5.3

8. Vertical air velocity: 1 field containing best measurement of average vertical air velocity along 1-km flight track segment -- format in m/s to 1 decimal place accuracy. If data is considered unreliable or is unavailable set to missing.

Example: 2.5

9. Total Counts and Concentrations: 2 fields computed for each of the FSSP, CPI, 2DC, and HVPS/2DP probes. Counts (non-dimensional) displayed in floating point notation with 1 decimal place accuracy and Concentrations (L -1) displayed in exponential notation with 3 decimal place accuracy (e.g., 1.234e-56). All 2D/HVPS concentrations and counts based on the Heymsfield and Parrish (1978) reconstructed method. The description of the counts and concentrations will be in the following order:

a. Total Counts calculated from the FSSP over the size range specified for the FSSP in the size spectra below in (16).
b. Total Concentration calculated from the FSSP over the size range specified for the FSSP in the size spectra below in (16).
c. Total Counts calculated from the CPI over the size range specified for the CPI in the size spectra below in (16).
d. Total Concentration calculated from the CPI (scaled to 2DC observations) over the size range specified for the CPI in the size spectra below in (16).
e. Total Counts calculated from the 2DC over the size range specified for the 2DC in the size spectra below in (16).
f. Total Concentration calculated from the 2DC using a reconstructed sample volume over the size range specified for the 2DC in the size spectra below in (16).
g. Total Counts calculated from the HVPS/2DP over the size range specified for the HVPS/2DP in the size spectra below in (16).
h. Total Concentration calculated from the HVPS/2DP using a reconstructed sample volume over the size range specified for the HVPS/2DP in the size spectra below in (16).

10. Habit recognition for spheres (proxy for liquid), graupel, aggregates, needles/columns, and small, indeterminate particles: 45 fields (5 habits times 3 combinations of instruments times 3 different weighting functions) containing percentage of particles in each of the above habit classifications. Format in nearest integer percent from 0-100. The threshold for indeterminate particles will be images with less than 25 pixels of image area. Pixel area will be a function of probe type.

a. Number weighted percentage of spherical, graupel, aggregate, needle/column and indeterminate particles from CPI (5 fields).
b. Area weighted percentage of spherical, graupel, aggregate, needle/column and indeterminate particles from CPI (5 fields).

c. Mass weighted percentage of spherical, graupel, aggregate, needle/column and indeterminate particles from CPI (5 fields).

d. Number weighted percentage of spherical, graupel, aggregate, needle/column and indeterminate particles from 2DC using Heymsfield's area-sphere ratio (5 fields).

e. Area weighted percentage of spherical, graupel, aggregate, needle/column and indeterminate particles from 2DC using Heymsfield's area-sphere ratio (5 fields).

f. Mass weighted percentage of spherical, graupel, aggregate, needle/column and indeterminate particles from 2DC using Heymsfield's area-sphere ratio (5 fields).

g. Number weighted percentage of spherical, graupel, aggregate, needle/column and indeterminate particles from HVPS/2DP using Heymsfield's area-sphere ratio (5 fields).

h. Area weighted percentage of spherical, graupel, aggregate, needle/column and indeterminate particles from HVPS/2DP using Heymsfield's area-sphere ratio (5 fields).

i. Mass weighted percentage of spherical, graupel, aggregate, needle/column and indeterminate particles from HVPS/2DP using Heymsfield's area-sphere ratio (5 fields).

11. Water/Ice Masses: 13 fields containing (a) cloud liquid water existence (yes/no) as observed by either the King hot-wire, Rosemount icing, or FSSP probes, (b) cloud liquid water content (LWC) as observed by either the King hot-wire, Rosemount icing, or FSSP probes, (c) flag for probe used in determination of cloud LWC: K for King hot-wire, R for Rosemount icing or F for FSSP, (d) cloud/precipitation LWC from spheres as observed by the CPI, (e) cloud/precipitation ice water content (IWC) for all ice particles observed by the CPI, (f) cloud/precipitation (IWC) from graupel as observed by the CPI, (g) cloud/precipitation IWC from aggregates as observed by the CPI, (h) cloud/precipitation IWC from needles/columns as observed by the CPI, (i) precipitation LWC from spheres as observed by the 2DC and HVPS/2DP, (j) precipitation IWC for all ice particles observed by the 2DC and HVPS/2DP, (k) precipitation IWC from graupel as observed by the 2DC and HVPS/2DP (l) precipitation IWC from aggregates as observed by the 2DC and HVPS/2DP and (m) precipitation IWC from needles/columns as observed by the 2DC and HVPS/2DP. Except for the first three fields, these parameters will be derived by integrating over the relevant size spectra using separate mass-dimension relationships for water, graupel, aggregates, and needles/columns as defined in the header. These LWC and IWC values will be reported in units of gram per cubic meter. If a mass field is unable to be calculated, a value of -999.99 will be set.

12. Mass-weighted mean particle size: 1 field containing mass-weighted mean particle size observed by the 2DC and HVPS/2DP. Values will be reported in micrometers.

13. Reflectivity: 1 field containing reflectivity observed by the 2DC and HVPS/2DP as calculated with the Heymsfield et al. (2000) technique. Values will be reported in dBZe. Missing values (-999.99) will be reported for air temperatures between –3° to +3° C.

14. Artifacts: 2 fields containing number weighted percentage of artifacts for the 2DC and HVPS/2DP, respectively. Format in nearest integer percent from 0-100.

15. Spares: 6 fields set to missing –999.99 until used.

Lines 2-3

16. Area Spectra: Two types of area spectra for all particles will be provided. All 2D/HVPS images are to be processed by the Heymsfield and Parrish (1978) reconstructed technique. Data for each spectra is contained in 1 spectra type field and 89 area bin fields for a total of 90 fields per spectra.

The spectra type flag will be placed in 1 field prior to the 89 area bin fields. It will indicate the type of output: CT=counts and CN=concentrations. Line 2 will contain an area spectrum of counts (CT) and line 3 will contain an area spectrum of concentration (CN).

Each area spectra will consist of 89 fields corresponding to 89 area bins. Counts per bin (non-dimensional) will be displayed in floating point notation with 1 decimal place accuracy. Concentrations per bin per bin width (L^{-1} µm^{-2}) will be displayed in exponential notation with 3 decimal place accuracy (e.g., 1.234e-56). Area categories will be as follows: 1600-22500 µm^2 range with 1900 µm^2 bin width (11 bins), 22500-1000000 µm^2 range with 57500 µm^2 bin width (17 bins), 1-625 mm^2 range with 10.4 mm^2 bin width (60 bins) and greater than or equal to 625 mm^2 (1 bin). CPI data (scaled to 2DC observations) will be used for the 1600-22500 µm^2 area range, 2DC data for the 22500-1000000 µm^2 area range, and HVPS/2DP data (whichever is relevant) for areas greater than 1 mm^2. If the available instruments on an aircraft are not able to provide the desired information for a particle area bin, a value of –999.99 should be set. The 89 area bins are summarized below where A is area of a particle:

1. 1.600×10^3 µm^2 <= A < 3.500×10^3 µm^2
…. CPI (scaled to 2DC)
11. 2.060×10^4 µm^2 <= A < 2.250×10^4 µm^2
12. 2.250×10^4 µm^2 <= A < 8.000×10^4 µm^2
…. 2DC
28. 9.425×10^5 µm^2 <= A < 1.000×10^6 µm^2
29. 1.000×10^6 µm^2 <= A < 1.140×10^7 µm^2
…. HVPS or 2DP
88. 6.146×10^8 µm^2 <= A < 6.250×10^8 µm^2
89. 6.250×10^8 µm^2 <= A

Lines 4-13

17. Size Spectra: Ten types of particle spectra will be provided. All 2D/HVPS images will be processed by the Heymsfield & Parrish (1978) reconstructed technique and sized by maximum dimension. Data for each spectra is contained in 2 spectra type fields and 96 size bin fields for a total of 98 fields per spectra.

The spectra type flags will be placed in 2 fields prior to the 90 size fields. The first flag indicates the subset of particles: AL=all, SP=spherical, GR=graupel, AG=aggregate, and NC=needle/column as determined from the Heymsfield area-sphere ratio. The second flag indicates the type of output: CT=counts and CN=concentration. Flags are separated by blank space.

The full list of spectra types to be included in CMPD is as follows:

a. Line 4 (AL CT) counts for all particles
b. Line 5 (AL CN) concentration for all particles
c. Line 6 (SP CT) counts for spherical particles
d. Line 7 (SP CN) concentration for spherical particles
e. Line 8 (GR CT) counts for graupel particles
f. Line 9 (GR CN) concentration for graupel particles
g. Line 10 (AG CT) counts for aggregate particles
h. Line 11 (AG CN) concentration for aggregate particles
i. Line 12 (NC CT) counts for needle/column particles
j. Line 13 (NC CN) concentration for needle/column particles

Each size spectra will consist of 96 fields corresponding to 96 size bins. Counts per bin (non-dimensional) will be displayed in floating point notation with 1 decimal place accuracy. Concentrations per bin per bin width (L^{-1} µm^{-1}) will be displayed in exponential notation with 3 decimal place accuracy (e.g., 1.234e-56). Size categories are as follows: 5-40 µm range with 5 µm bin width (7 bins), 40-150 µm range with 10 µm bin width (11 bins), 150-1000 µm range with 50 µm bin width (17 bins), 1-25 mm range with 400 µm bin width (60 bins) and greater than or equal to 25 mm (1 bin). FSSP data will be used for the 5-40 µm size range, CPI data (scaled to 2DC observations) for the 40-150 µm size range, 2DC data for the

150-1000 µm size range, and HVPS/2DP data (whichever is relevant) for sizes greater than 1 mm. If the available instruments on an aircraft are not able to provide the desired information for a particle size bin, a value of –999.99 should be set. The 96 size bins are summarized below where D is the maximum dimension of a particle:

1. 5 µm <= D < 10 µm
…. FSSP
7. 35 µm <= D < 40 µm
8. 40 µm <= D < 50 µm
…. CPI (scaled to 2DC)
18. 140 µm <= D < 150 µm
19. 150 µm <= D < 200 µm
…. 2DC
35. 950 µm <= D < 1000 µm
36. 1000 µm <= D < 1400 µm
…. HVPS or 2DP
95. 24600 µm <= D < 25000 µm
96. 25000 µm <= D

E. References

Heymsfield, A.J., and J.L. Parrish, 1978: A computational technique for increasing the effective sampling volume of the PMS two-dimensional particle size spectrometer. *J. Appl. Meteor,.* **17**, 1566-1572.

Heymsfield, A.J., P.R. Field, J. Stith, J. E. Dye, and A. Grainger, 2000: Ice particle evolution in tropical stratiform ice clouds: Results from TRMM field programs. Preprint Vol., *13th AMS International Conf. on Clouds and Precipitation*, Amer. Meteorol. Soc., Boston, MA, 669-672.

F. Document Access

The most current version of this document in PDF format can be found at:

http://www.atmos.washington.edu/gcg/MG/KWAJ/ops-web/intro_microphys.html

Please direct questions and comments to:

Dr. David Kingsmill	Dr. Sandra Yuter
Desert Research Institute	University of Washington
Reno, NV	Seattle, Washington
davidk@dri.edu	yuter@atmos.washington.edu

10.0 Appendix 3: Superpixel-Matched Aircraft Microphysics Dataset

SP #	Lat	Lon	Cvr	Cit	DC-8	SP #	Lat	Lon	Cvr	Cit	DC-8
1254	7.75	166.84	NO	NO	YES	1580	7.70	166.92	NO	NO	YES
1255	7.74	166.84	NO	NO	YES	1584	7.68	166.92	NO	NO	YES
1261	7.76	166.85	NO	NO	YES	1911	7.92	167.14	NO	NO	YES
1262	7.74	166.86	NO	NO	YES	1916	7.91	167.13	NO	NO	YES
1267	7.77	166.86	NO	NO	YES	1917	7.93	167.13	YES	NO	NO
1268	7.76	166.87	NO	NO	YES	1921	7.91	167.11	NO	NO	YES
1274	7.77	166.87	NO	NO	YES	1922	7.93	167.11	YES	NO	NO
1275	7.76	166.88	NO	NO	YES	1928	7.92	167.10	YES	NO	YES
1281	7.78	166.88	NO	NO	YES	1929	7.93	167.10	YES	NO	NO
1282	7.77	166.89	NO	NO	YES	1933	7.91	167.08	YES	NO	YES
1288	7.79	166.89	NO	NO	YES	1937	7.91	167.07	YES	NO	YES
1289	7.78	166.90	NO	NO	YES	1941	7.92	167.06	YES	NO	YES
1296	7.79	166.91	NO	NO	YES	1949	7.91	167.03	YES	NO	YES
1303	7.79	166.92	NO	NO	YES	1950	7.93	167.02	YES	NO	NO
1310	7.80	166.93	NO	NO	YES	1954	7.91	167.01	YES	NO	YES
1311	7.79	166.94	NO	NO	YES	1955	7.93	167.01	YES	NO	NO
1317	7.81	166.95	NO	NO	YES	1960	7.91	167.00	YES	NO	YES
1324	7.81	166.96	NO	NO	YES	1961	7.93	167.00	YES	NO	NO
1331	7.82	166.97	NO	NO	YES	1967	7.91	166.98	YES	NO	YES
1338	7.83	166.98	NO	NO	YES	1968	7.93	166.98	YES	NO	NO
1339	7.82	166.99	NO	NO	YES	1974	7.92	166.97	YES	NO	YES
1345	7.84	167.00	NO	NO	YES	1975	7.93	166.97	YES	NO	NO
1352	7.84	167.01	NO	NO	YES	1981	7.92	166.95	YES	NO	YES
1353	7.83	167.02	NO	NO	YES	1982	7.93	166.95	YES	NO	NO
1359	7.85	167.02	NO	NO	YES	1988	7.91	166.94	YES	NO	YES
1366	7.86	167.03	NO	NO	YES	1989	7.93	166.94	YES	NO	NO
1373	7.86	167.05	NO	NO	YES	1995	7.91	166.93	YES	NO	YES
1380	7.87	167.06	NO	NO	YES	1996	7.93	166.92	YES	NO	NO
1387	7.88	167.07	NO	NO	YES	2002	7.91	166.91	YES	NO	YES
1394	7.89	167.08	NO	NO	YES	2003	7.93	166.91	YES	NO	NO
1401	7.89	167.10	NO	NO	YES	2008	7.92	166.90	YES	NO	YES
1408	7.90	167.11	NO	NO	YES	2009	7.93	166.90	YES	NO	NO
1409	7.89	167.11	NO	NO	YES	2014	7.92	166.88	YES	NO	YES
1415	7.91	167.12	NO	NO	YES	2020	7.92	166.87	YES	NO	YES
1416	7.90	167.13	NO	NO	YES	2021	7.93	166.87	YES	NO	NO
1422	7.92	167.13	NO	NO	YES	2026	7.92	166.85	YES	NO	YES
1423	7.90	167.14	NO	NO	YES	2032	7.92	166.84	YES	NO	YES
1428	7.93	167.14	NO	NO	YES	2038	7.92	166.83	YES	NO	YES
1429	7.92	167.15	NO	NO	YES	2044	7.92	166.81	YES	NO	YES
1435	7.94	167.15	NO	NO	YES	2051	7.91	166.80	YES	NO	YES
1436	7.93	167.16	NO	NO	YES	2052	7.93	166.80	YES	NO	NO
1443	7.94	167.17	NO	NO	YES	2058	7.91	166.78	YES	NO	YES
1444	7.93	167.18	NO	NO	YES	2065	7.91	166.77	YES	NO	YES
1447	7.95	167.18	NO	NO	YES	2072	7.92	166.75	YES	NO	YES
1448	7.93	167.19	NO	NO	YES	2079	7.92	166.74	YES	NO	YES
1451	7.95	167.19	NO	NO	YES	2083	7.91	166.72	YES	NO	YES
1452	7.94	167.20	NO	NO	YES	2087	7.91	166.71	YES	NO	YES
1465	7.98	167.27	NO	NO	YES	2091	7.91	166.69	YES	NO	YES
1473	8.01	167.30	NO	NO	YES	2096	7.91	166.68	YES	NO	YES
1474	8.00	167.31	NO	NO	YES	2102	7.92	166.67	YES	NO	YES
1478	8.01	167.31	NO	NO	YES	2109	7.92	166.65	YES	NO	NO
1496	7.96	167.22	NO	NO	YES	2116	7.92	166.64	YES	NO	NO
1497	7.97	167.21	NO	NO	YES	2123	7.92	166.62	YES	NO	NO
1501	7.95	167.21	NO	NO	YES	2157	8.00	166.73	NO	NO	YES
1506	7.95	167.20	NO	NO	YES	2160	7.99	166.74	NO	NO	YES
1511	7.94	167.19	NO	NO	YES	2172	7.97	166.80	NO	NO	YES
1515	7.93	167.17	NO	NO	YES	2177	7.97	166.81	NO	NO	YES
1519	7.92	167.16	NO	NO	YES	2178	7.95	166.80	NO	NO	YES
1520	7.93	167.15	NO	NO	YES	2180	7.93	166.78	YES	NO	NO
1524	7.92	167.15	NO	NO	YES	2184	7.96	166.82	NO	NO	YES
1531	7.91	167.13	NO	NO	YES	2187	7.92	166.80	YES	NO	NO
1537	7.86	167.09	NO	NO	YES	2191	7.95	166.83	NO	NO	YES
1538	7.87	167.08	NO	NO	YES	2192	7.94	166.83	NO	NO	YES
1545	7.77	166.99	NO	NO	YES	2193	7.93	166.82	YES	NO	NO
1552	7.76	166.98	NO	NO	YES	2194	7.91	166.81	YES	NO	NO
1558	7.75	166.98	NO	NO	YES	2198	7.94	166.84	NO	NO	YES
1563	7.74	166.97	NO	NO	YES	2199	7.93	166.84	NO	NO	YES
1564	7.75	166.95	NO	NO	YES	2200	7.92	166.83	YES	NO	NO
1567	7.73	166.96	NO	NO	YES	2205	7.94	166.86	NO	NO	YES
1568	7.74	166.95	NO	NO	YES	2206	7.92	166.85	YES	NO	NO
1571	7.72	166.95	NO	NO	YES	2207	7.91	166.84	YES	NO	NO
1575	7.71	166.94	NO	NO	YES	2212	7.93	166.87	YES	NO	YES
1576	7.71	166.93	NO	NO	YES	2213	7.91	166.86	YES	NO	NO
1579	7.69	166.93	NO	NO	YES	2219	7.92	166.88	YES	NO	YES

SP #	Lat	Lon	Cvr	Cit	DC-8	SP #	Lat	Lon	Cvr	Cit	DC-8
2220	7.91	166.87	YES	NO	NO	2636	7.89	166.95	YES	NO	NO
2225	7.92	166.89	YES	NO	YES	2638	7.91	166.95	NO	NO	YES
2226	7.91	166.89	NO	NO	YES	2639	7.93	166.95	NO	NO	YES
2230	7.91	166.90	YES	NO	YES	2643	7.89	166.93	YES	NO	NO
2240	7.92	166.98	YES	NO	NO	2645	7.92	166.93	NO	NO	YES
2241	7.91	166.97	YES	NO	NO	2650	7.89	166.92	YES	NO	NO
2243	7.88	166.96	NO	NO	YES	2652	7.91	166.92	NO	NO	YES
2244	7.87	166.95	NO	NO	YES	2658	7.89	166.89	YES	NO	NO
2245	7.91	166.99	YES	NO	NO	2660	7.89	166.88	YES	NO	NO
2248	7.87	166.97	NO	NO	YES	2662	7.91	166.88	NO	NO	YES
2254	7.86	166.98	NO	NO	YES	2664	7.89	166.87	YES	NO	NO
2260	7.86	166.99	NO	NO	YES	2666	7.91	166.86	NO	NO	YES
2261	7.84	166.98	NO	NO	YES	2668	7.89	166.85	YES	NO	NO
2266	7.85	167.00	NO	NO	YES	2670	7.92	166.85	NO	NO	YES
2277	7.83	167.04	NO	NO	YES	2674	7.91	166.84	NO	NO	YES
2283	7.82	167.05	NO	NO	YES	2678	7.91	166.82	NO	NO	YES
2289	7.81	167.06	NO	NO	YES	2679	7.93	166.82	NO	NO	YES
2290	7.80	167.06	NO	NO	YES	2683	7.91	166.81	NO	NO	YES
2296	7.81	167.08	NO	NO	YES	2684	7.93	166.81	NO	NO	YES
2297	7.79	167.07	NO	NO	YES	2688	7.91	166.80	NO	NO	YES
2302	7.80	167.09	NO	NO	YES	2692	7.91	166.78	NO	NO	YES
2303	7.79	167.08	NO	NO	YES	3255	8.21	167.93	YES	NO	NO
2307	7.79	167.10	NO	NO	YES	3258	8.22	167.95	YES	NO	NO
2308	7.78	167.09	NO	NO	YES	3259	8.21	167.95	YES	NO	NO
2317	7.87	167.08	YES	NO	NO	3264	8.22	167.96	YES	NO	NO
2319	7.89	167.07	YES	NO	NO	3265	8.21	167.96	YES	NO	NO
2321	7.92	167.07	YES	NO	YES	3270	8.22	167.97	YES	NO	NO
2326	7.88	167.05	YES	NO	NO	3271	8.21	167.97	YES	NO	NO
2328	7.91	167.05	NO	NO	YES	3273	8.22	167.99	YES	NO	NO
2333	7.88	167.04	YES	NO	NO	3274	8.21	167.99	YES	NO	NO
2335	7.92	167.04	YES	NO	YES	3277	8.22	168.00	YES	NO	NO
2340	7.89	167.02	YES	NO	NO	3278	8.21	168.00	YES	NO	NO
2342	7.92	167.02	YES	NO	YES	3282	8.22	168.01	YES	NO	NO
2347	7.89	167.01	YES	NO	NO	3283	8.21	168.01	YES	NO	NO
2349	7.92	167.01	YES	NO	YES	3286	8.22	168.03	YES	NO	NO
2354	7.89	166.99	YES	NO	NO	3287	8.20	168.03	YES	NO	NO
2356	7.89	166.98	YES	NO	NO	3290	8.22	168.04	YES	NO	NO
2358	7.89	166.97	YES	NO	NO	3291	8.20	168.04	YES	NO	NO
2360	7.88	166.95	YES	NO	NO	3296	8.22	168.06	YES	NO	NO
2362	7.88	166.94	YES	NO	NO	3297	8.20	168.06	YES	NO	NO
2363	7.90	166.94	YES	NO	NO	3304	8.20	168.07	YES	NO	NO
2365	7.88	166.92	YES	NO	NO	3311	8.20	168.08	YES	NO	NO
2370	7.90	166.86	YES	NO	NO	3321	8.19	168.11	YES	NO	NO
2371	7.91	166.86	NO	NO	YES	3327	8.20	168.12	YES	NO	NO
2372	7.93	166.86	NO	NO	YES	3328	8.19	168.12	YES	NO	NO
2376	7.89	166.85	YES	NO	NO	3334	8.20	168.14	YES	NO	NO
2377	7.90	166.85	YES	NO	NO	3335	8.19	168.14	YES	NO	NO
2378	7.92	166.85	NO	NO	YES	3341	8.18	168.15	YES	NO	NO
2383	7.89	166.84	YES	NO	NO	3346	8.20	168.16	YES	NO	NO
2385	7.92	166.83	NO	NO	YES	3347	8.18	168.16	YES	NO	NO
2390	7.88	166.82	YES	NO	NO	3352	8.19	168.18	YES	NO	NO
2392	7.91	166.82	NO	NO	YES	3353	8.18	168.18	YES	NO	NO
2397	7.88	166.81	YES	NO	NO	3359	8.19	168.19	YES	NO	NO
2399	7.91	166.80	NO	NO	YES	3360	8.18	168.19	YES	NO	NO
2404	7.88	166.79	YES	NO	NO	3366	8.19	168.20	YES	NO	NO
2406	7.91	166.79	NO	NO	YES	3367	8.18	168.20	YES	NO	NO
2411	7.88	166.78	YES	NO	NO	3374	8.18	168.22	YES	NO	NO
2413	7.91	166.77	NO	NO	YES	3380	8.19	168.23	YES	NO	NO
2420	7.91	166.76	NO	NO	YES	3381	8.18	168.23	YES	NO	NO
2427	7.91	166.74	NO	NO	YES	3386	8.19	168.25	YES	NO	NO
2434	7.91	166.73	NO	NO	YES	3387	8.17	168.25	YES	NO	NO
2441	7.92	166.71	NO	NO	YES	3392	8.17	168.26	YES	NO	NO
2448	7.92	166.70	NO	NO	YES	3396	8.17	168.27	YES	NO	NO
2455	7.92	166.68	NO	NO	YES	3401	8.17	168.29	YES	NO	NO
2462	7.92	166.67	NO	NO	YES	3406	8.17	168.30	YES	NO	NO
2469	7.92	166.65	NO	NO	YES	3410	8.18	168.31	YES	NO	NO
2476	7.92	166.64	NO	NO	YES	3411	8.17	168.31	YES	NO	NO
2483	7.91	166.62	NO	NO	YES	3420	8.17	168.27	YES	NO	NO
2540	7.90	166.84	YES	NO	NO	3422	8.17	168.26	YES	NO	NO
2541	7.90	166.88	YES	NO	NO	3425	8.17	168.25	YES	NO	NO
2542	7.89	166.87	YES	NO	NO	3429	8.17	168.23	YES	NO	NO
2545	7.89	166.89	YES	NO	NO	3433	8.17	168.22	YES	NO	NO
2630	7.89	166.96	YES	NO	NO	3434	8.19	168.22	YES	NO	NO
2632	7.91	166.96	NO	NO	YES	3438	8.17	168.20	YES	NO	NO

SP #	Lat	Lon	Cvr	Cit	DC-8	SP #	Lat	Lon	Cvr	Cit	DC-8
3439	8.19	168.20	YES	NO	NO	4687	8.12	167.80	NO	NO	YES
3443	8.17	168.19	YES	NO	NO	4694	8.13	167.80	NO	NO	YES
3444	8.19	168.19	YES	NO	NO	4695	8.13	167.82	NO	NO	YES
3449	8.18	168.17	YES	NO	NO	4701	8.15	167.81	NO	NO	YES
3450	8.19	168.18	YES	NO	NO	4702	8.14	167.82	NO	NO	YES
3455	8.18	168.16	YES	NO	NO	4708	8.16	167.81	NO	NO	YES
3459	8.18	168.14	YES	NO	NO	4709	8.16	167.83	NO	NO	YES
3460	8.19	168.15	YES	NO	NO	4715	8.17	167.82	NO	NO	YES
3463	8.18	168.13	YES	NO	NO	4722	8.19	167.83	NO	NO	YES
3464	8.19	168.13	YES	NO	NO	4723	8.18	167.84	NO	NO	YES
3469	8.18	168.12	YES	NO	NO	4730	8.21	167.84	NO	NO	YES
3489	8.20	168.05	YES	NO	NO	4735	8.23	167.84	NO	NO	YES
3491	8.20	168.03	YES	NO	NO	4736	8.22	167.86	NO	NO	YES
3492	8.20	168.02	YES	NO	NO	4742	8.24	167.85	NO	NO	YES
3495	8.19	168.00	YES	NO	NO	4749	8.25	167.85	NO	NO	YES
3496	8.20	168.00	YES	NO	NO	4756	8.27	167.86	NO	NO	YES
3500	8.19	167.99	YES	NO	NO	4763	8.28	167.86	NO	NO	YES
3508	8.19	167.96	YES	NO	NO	4764	8.28	167.87	NO	NO	YES
3512	8.19	167.94	YES	NO	NO	4770	8.29	167.87	NO	NO	YES
3516	8.19	167.93	YES	NO	NO	4771	8.29	167.88	NO	NO	YES
3517	8.21	167.93	YES	NO	NO	4777	8.31	167.87	NO	NO	YES
3528	8.21	167.89	YES	NO	NO	4778	8.30	167.89	NO	NO	YES
3532	8.20	167.87	YES	NO	NO	4784	8.32	167.88	NO	NO	YES
3822	9.13	167.66	YES	NO	NO	4785	8.31	167.89	NO	NO	YES
3823	9.12	167.67	YES	NO	NO	4791	8.33	167.88	NO	NO	YES
3828	9.10	167.66	YES	NO	NO	4792	8.33	167.89	NO	NO	YES
3829	9.12	167.65	YES	NO	NO	4798	8.35	167.89	NO	NO	YES
3833	9.10	167.64	YES	NO	NO	4799	8.34	167.90	NO	NO	YES
3834	9.11	167.64	YES	NO	NO	4805	8.36	167.90	NO	NO	YES
3837	9.08	167.63	YES	NO	NO	4811	8.37	167.89	NO	NO	YES
3838	9.09	167.63	YES	NO	NO	4812	8.37	167.91	NO	NO	YES
3841	9.06	167.62	YES	NO	NO	4819	8.38	167.91	NO	NO	YES
3842	9.07	167.62	YES	NO	NO	4826	8.40	167.91	NO	NO	YES
3845	9.06	167.61	YES	NO	NO	4827	8.39	167.92	NO	NO	YES
3846	9.07	167.61	YES	NO	NO	4833	8.41	167.92	NO	NO	YES
3852	9.05	167.58	YES	NO	NO	4834	8.41	167.93	NO	NO	YES
3854	9.06	167.58	YES	NO	NO	4840	8.42	167.92	NO	NO	YES
3888	9.10	167.60	YES	NO	NO	4847	8.44	167.93	NO	NO	YES
3891	9.08	167.60	YES	NO	NO	4854	8.45	167.93	NO	NO	YES
3892	9.09	167.59	YES	NO	NO	4855	8.45	167.95	NO	NO	YES
3894	9.06	167.59	YES	NO	NO	4861	8.46	167.94	NO	NO	YES
3895	9.07	167.58	YES	NO	NO	4868	8.48	167.94	NO	NO	YES
3897	9.05	167.58	YES	NO	NO	4869	8.47	167.96	NO	NO	YES
3898	9.06	167.58	YES	NO	NO	4875	8.49	167.95	NO	NO	YES
3968	8.11	167.77	NO	NO	YES	4882	8.50	167.96	NO	NO	YES
3969	8.12	167.76	NO	NO	YES	4889	8.52	167.96	NO	NO	YES
3973	8.11	167.76	NO	NO	YES	4896	8.53	167.97	NO	NO	YES
3976	8.09	167.76	NO	NO	YES	4903	8.54	167.97	NO	NO	YES
3977	8.10	167.75	NO	NO	YES	4904	8.54	167.98	NO	NO	YES
3978	8.10	167.73	NO	NO	YES	4910	8.55	167.98	NO	NO	YES
3979	8.09	167.71	YES	NO	NO	4911	8.55	167.99	NO	NO	YES
3980	8.11	167.70	YES	NO	NO	4917	8.57	167.98	NO	NO	YES
3981	8.10	167.69	YES	NO	NO	4918	8.56	167.99	NO	NO	YES
3992	8.01	167.65	YES	NO	YES	4924	8.58	167.99	NO	NO	YES
3993	8.02	167.64	YES	NO	NO	4931	8.59	167.99	NO	NO	YES
3999	8.00	167.64	YES	NO	YES	4938	8.61	168.00	NO	NO	YES
4000	8.01	167.63	YES	NO	YES	4945	8.62	168.00	NO	NO	YES
4006	7.99	167.63	YES	NO	YES	4952	8.63	168.01	NO	NO	YES
4007	8.00	167.62	NO	NO	YES	4959	8.65	168.02	NO	NO	YES
4012	7.98	167.63	YES	NO	NO	4966	8.66	168.02	NO	NO	YES
4013	7.99	167.62	YES	NO	YES	4967	8.65	168.03	NO	NO	YES
4014	8.00	167.61	NO	NO	YES	4973	8.67	168.02	NO	NO	YES
4019	7.97	167.62	YES	NO	NO	4974	8.67	168.04	NO	NO	YES
4020	7.98	167.61	YES	NO	YES	4980	8.68	168.03	NO	NO	YES
4026	7.96	167.61	YES	NO	YES	4981	8.68	168.04	NO	NO	YES
4027	7.97	167.60	YES	NO	YES	4987	8.70	168.04	YES	NO	YES
4028	7.98	167.59	NO	NO	YES	4994	8.71	168.04	YES	NO	YES
4033	7.95	167.59	YES	NO	NO	4995	8.71	168.05	YES	NO	YES
4034	7.96	167.59	YES	NO	YES	4996	8.70	168.07	NO	YES	NO
4040	7.94	167.58	YES	NO	NO	5000	8.73	168.03	YES	NO	NO
4041	7.95	167.57	YES	NO	NO	5001	8.73	168.05	YES	NO	YES
4064	7.96	167.59	NO	NO	YES	5002	8.72	168.06	YES	NO	YES
4065	7.96	167.61	NO	NO	YES	5003	8.72	168.07	NO	YES	NO
4069	7.98	167.61	NO	NO	YES	5007	8.74	168.04	YES	NO	NO

SP #	Lat	Lon	Cvr	Cit	DC-8	SP #	Lat	Lon	Cvr	Cit	DC-8
5008	8.74	168.05	YES	NO	YES	5224	8.65	168.03	NO	YES	NO
5009	8.73	168.07	YES	NO	NO	5225	8.65	168.02	YES	NO	NO
5010	8.73	168.08	NO	YES	NO	5230	8.63	168.04	NO	YES	NO
5014	8.76	168.05	YES	NO	NO	5232	8.64	168.01	YES	NO	NO
5015	8.75	168.06	YES	NO	YES	5237	8.62	168.04	NO	YES	NO
5016	8.75	168.07	YES	NO	YES	5238	8.63	168.02	NO	YES	NO
5017	8.74	168.09	NO	YES	NO	5239	8.63	168.01	YES	NO	NO
5021	8.77	168.05	YES	NO	NO	5244	8.61	168.03	NO	YES	NO
5022	8.77	168.07	YES	NO	YES	5245	8.61	168.02	NO	YES	NO
5023	8.76	168.08	YES	NO	NO	5246	8.62	168.01	YES	NO	NO
5024	8.76	168.09	NO	YES	NO	5251	8.59	168.03	NO	YES	NO
5029	8.78	168.07	YES	NO	YES	5252	8.60	168.01	NO	YES	NO
5030	8.77	168.08	YES	NO	YES	5253	8.60	168.00	YES	NO	NO
5031	8.77	168.10	NO	YES	NO	5258	8.58	168.02	NO	YES	NO
5035	8.80	168.06	YES	NO	NO	5259	8.59	168.01	YES	YES	NO
5036	8.79	168.08	YES	NO	YES	5260	8.59	167.99	YES	NO	NO
5037	8.79	168.09	YES	NO	YES	5265	8.57	168.02	NO	YES	NO
5038	8.78	168.10	NO	YES	NO	5266	8.57	168.00	YES	YES	NO
5042	8.81	168.07	YES	NO	NO	5267	8.58	167.99	YES	NO	NO
5043	8.80	168.08	YES	NO	YES	5272	8.56	168.01	NO	YES	NO
5044	8.80	168.09	YES	YES	YES	5273	8.56	168.00	YES	YES	NO
5045	8.79	168.11	NO	YES	NO	5274	8.57	167.98	YES	NO	NO
5049	8.82	168.07	YES	NO	NO	5279	8.54	168.00	NO	YES	NO
5050	8.82	168.09	YES	NO	YES	5280	8.55	167.99	YES	YES	NO
5051	8.81	168.10	YES	NO	YES	5281	8.55	167.98	YES	NO	NO
5052	8.81	168.11	NO	YES	NO	5287	8.53	167.99	NO	YES	NO
5056	8.84	168.08	YES	NO	NO	5288	8.54	167.97	YES	NO	NO
5057	8.83	168.09	YES	NO	YES	5294	8.52	167.98	NO	YES	NO
5058	8.83	168.10	YES	YES	NO	5295	8.52	167.97	YES	NO	NO
5059	8.82	168.12	NO	YES	NO	5301	8.51	167.97	YES	YES	NO
5063	8.85	168.08	YES	NO	NO	5302	8.51	167.96	YES	NO	NO
5064	8.84	168.10	YES	NO	YES	5308	8.49	167.97	NO	YES	NO
5065	8.84	168.11	NO	NO	YES	5309	8.50	167.96	YES	YES	NO
5125	8.83	168.12	NO	YES	NO	5315	8.48	167.96	NO	YES	NO
5126	8.83	168.10	NO	YES	NO	5316	8.49	167.95	YES	NO	NO
5132	8.81	168.11	NO	YES	NO	5322	8.47	167.96	NO	YES	NO
5133	8.82	168.10	YES	NO	NO	5323	8.47	167.95	YES	YES	NO
5134	8.82	168.09	YES	NO	NO	5329	8.45	167.96	NO	YES	NO
5139	8.80	168.11	NO	YES	NO	5330	8.46	167.94	YES	YES	NO
5140	8.80	168.10	YES	YES	NO	5336	8.44	167.95	NO	YES	NO
5141	8.81	168.08	YES	NO	NO	5337	8.45	167.93	YES	YES	NO
5146	8.79	168.11	NO	YES	NO	5343	8.43	167.94	NO	YES	NO
5147	8.79	168.09	YES	YES	NO	5344	8.44	167.93	YES	NO	NO
5148	8.80	168.08	YES	NO	NO	5350	8.42	167.94	NO	YES	NO
5153	8.77	168.10	NO	YES	NO	5351	8.42	167.92	YES	YES	NO
5154	8.78	168.09	NO	YES	NO	5357	8.40	167.93	NO	YES	NO
5155	8.78	168.07	YES	NO	NO	5358	8.41	167.92	YES	YES	NO
5160	8.76	168.10	NO	YES	NO	5364	8.39	167.93	NO	YES	NO
5161	8.77	168.08	YES	YES	NO	5365	8.39	167.91	YES	YES	NO
5162	8.77	168.07	YES	NO	NO	5371	8.38	167.92	NO	YES	NO
5167	8.75	168.09	NO	YES	NO	5372	8.38	167.91	YES	YES	NO
5168	8.75	168.08	YES	YES	NO	5379	8.37	167.90	YES	YES	NO
5169	8.76	168.06	YES	NO	NO	5385	8.35	167.91	NO	YES	NO
5174	8.73	168.08	NO	YES	NO	5386	8.36	167.90	YES	YES	NO
5175	8.74	168.07	YES	NO	NO	5392	8.34	167.90	NO	YES	NO
5176	8.75	168.06	YES	NO	NO	5393	8.34	167.89	YES	YES	NO
5181	8.72	168.08	NO	YES	NO	5400	8.33	167.89	YES	YES	NO
5182	8.73	168.06	YES	NO	NO	5401	8.34	167.88	YES	NO	NO
5183	8.73	168.05	YES	NO	NO	5407	8.32	167.88	YES	YES	NO
5188	8.71	168.07	NO	YES	NO	5411	8.29	167.92	NO	YES	NO
5189	8.72	168.06	YES	NO	NO	5412	8.29	167.90	NO	YES	NO
5190	8.72	168.04	YES	NO	NO	5413	8.30	167.89	NO	YES	NO
5195	8.70	168.07	NO	YES	NO	5414	8.31	167.87	YES	YES	NO
5196	8.70	168.05	YES	NO	NO	5419	8.28	167.90	NO	YES	NO
5197	8.71	168.04	YES	NO	NO	5421	8.29	167.87	YES	YES	NO
5202	8.68	168.06	NO	YES	NO	5422	8.30	167.86	YES	NO	NO
5204	8.69	168.04	YES	NO	NO	5428	8.28	167.86	YES	YES	NO
5209	8.67	168.06	NO	YES	NO	5527	8.29	167.88	NO	YES	NO
5210	8.68	168.04	NO	YES	NO	5528	8.29	167.90	NO	YES	NO
5211	8.68	168.03	YES	NO	NO	5529	8.28	167.91	NO	YES	NO
5216	8.66	168.06	NO	YES	NO	5533	8.31	167.88	YES	YES	NO
5217	8.66	168.04	NO	YES	NO	5534	8.30	167.89	YES	YES	NO
5218	8.67	168.03	YES	NO	NO	5535	8.30	167.90	NO	YES	NO
5223	8.64	168.05	NO	YES	NO	5536	8.29	167.92	NO	YES	NO

SP #	Lat	Lon	Cvr	Cit	DC-8	SP #	Lat	Lon	Cvr	Cit	DC-8
5540	8.32	167.88	YES	NO	NO	10579	7.96	167.79	NO	NO	YES
5541	8.32	167.89	YES	YES	NO	10580	7.95	167.78	NO	NO	YES
5547	8.33	167.88	YES	NO	NO	10584	7.95	167.80	NO	NO	YES
5548	8.33	167.90	YES	YES	NO	10592	8.00	167.74	NO	NO	YES
5554	8.35	167.89	YES	NO	NO	10593	7.99	167.75	NO	NO	YES
5555	8.34	167.90	YES	YES	NO	10594	8.01	167.74	NO	NO	YES
5561	8.36	167.90	YES	YES	NO	10595	8.00	167.76	NO	NO	YES
5562	8.35	167.91	NO	YES	NO	10976	8.02	168.77	NO	YES	NO
5568	8.37	167.90	YES	NO	NO	10977	7.97	168.72	NO	YES	NO
5569	8.37	167.91	NO	YES	NO	10978	7.99	168.71	NO	YES	NO
5575	8.38	167.91	YES	YES	NO	10979	7.96	168.69	NO	YES	NO
5576	8.38	167.92	NO	YES	NO	10982	7.97	168.67	NO	YES	NO
5582	8.40	167.91	YES	YES	NO	10987	7.96	168.66	NO	YES	NO
5583	8.39	167.93	NO	YES	NO	10988	7.97	168.65	NO	YES	NO
5588	8.41	167.91	YES	NO	NO	10992	7.95	168.64	NO	YES	NO
5589	8.41	167.92	YES	YES	NO	10993	7.97	168.64	NO	YES	NO
5590	8.40	167.93	NO	YES	NO	10998	7.95	168.63	NO	YES	NO
5595	8.43	167.91	YES	NO	NO	10999	7.96	168.63	NO	YES	NO
5596	8.42	167.93	YES	YES	NO	11002	7.94	168.62	NO	YES	NO
5597	8.42	167.94	NO	YES	NO	11003	7.95	168.61	NO	YES	NO
5603	8.44	167.93	YES	YES	NO	11326	7.87	168.05	NO	YES	NO
5604	8.43	167.94	NO	YES	NO	11334	8.01	168.22	NO	NO	YES
5609	8.46	167.92	YES	NO	NO	11339	8.02	168.23	NO	NO	YES
5610	8.45	167.93	YES	YES	NO	11449	7.89	167.86	NO	NO	YES
5611	8.45	167.95	NO	YES	NO	11453	7.85	167.86	NO	YES	NO
5617	8.46	167.94	YES	YES	NO	11454	7.87	167.86	NO	YES	NO
5618	8.46	167.95	NO	YES	NO	11455	7.88	167.85	NO	NO	YES
5624	8.48	167.94	YES	YES	NO	11461	7.86	167.85	NO	YES	NO
5625	8.47	167.96	NO	YES	NO	11462	7.87	167.84	NO	YES	YES
5631	8.49	167.95	YES	YES	NO	11463	7.89	167.84	NO	NO	YES
5632	8.48	167.96	NO	YES	NO	11469	7.87	167.83	NO	YES	YES
5638	8.50	167.95	YES	YES	NO	11470	7.89	167.82	NO	YES	NO
5639	8.50	167.97	NO	YES	NO	11476	7.87	167.81	NO	NO	YES
5645	8.52	167.96	YES	YES	NO	11477	7.89	167.81	NO	YES	NO
5646	8.51	167.97	NO	YES	NO	11478	7.90	167.80	NO	YES	NO
5652	8.53	167.96	YES	YES	NO	11483	7.87	167.80	NO	NO	YES
5653	8.53	167.98	YES	YES	NO	11484	7.88	167.79	NO	YES	NO
5659	8.54	167.97	YES	YES	NO	11485	7.89	167.79	NO	YES	NO
5660	8.54	167.98	YES	YES	NO	11486	7.91	167.78	NO	YES	NO
5666	8.56	167.98	YES	YES	NO	11490	7.86	167.79	NO	NO	YES
5667	8.55	167.99	YES	YES	NO	11491	7.87	167.78	NO	NO	YES
5673	8.57	167.98	YES	YES	NO	11492	7.90	167.78	NO	YES	NO
5674	8.56	168.00	YES	YES	NO	11496	7.85	167.78	NO	NO	YES
5680	8.58	167.99	YES	YES	NO	11500	7.85	167.76	NO	NO	YES
5681	8.58	168.00	YES	YES	NO	11515	7.87	167.81	NO	NO	YES
5687	8.60	167.99	YES	YES	NO	11516	7.87	167.83	NO	YES	YES
5688	8.59	168.01	YES	YES	NO	11517	7.89	167.81	NO	YES	NO
5694	8.61	168.00	YES	YES	NO	11520	7.90	167.80	NO	NO	YES
5695	8.60	168.01	YES	YES	NO	11524	7.90	167.78	NO	NO	YES
5701	8.62	168.00	YES	YES	NO	11531	7.90	167.77	NO	NO	YES
5702	8.62	168.02	YES	YES	NO	11538	7.89	167.75	NO	NO	YES
5708	8.64	168.01	YES	YES	NO	11545	7.89	167.74	NO	NO	YES
5709	8.63	168.02	YES	YES	NO	11552	7.89	167.73	NO	NO	YES
5715	8.65	168.01	YES	NO	NO	11557	7.89	167.71	NO	NO	YES
5716	8.64	168.03	YES	NO	NO	13619	8.27	166.90	NO	NO	YES
10438	7.90	167.76	NO	NO	YES	13625	8.27	166.91	NO	NO	YES
10442	7.91	167.77	NO	NO	YES	13631	8.28	166.92	NO	NO	YES
10447	7.92	167.77	NO	NO	YES	13636	8.29	166.94	NO	NO	YES
10451	7.94	167.77	NO	NO	YES	13641	8.29	166.95	NO	NO	YES
10455	7.95	167.78	NO	NO	YES	13642	8.28	166.95	NO	NO	YES
10456	7.95	167.79	NO	NO	YES	13647	8.30	166.96	NO	NO	YES
10460	7.96	167.79	NO	NO	YES	13653	8.31	166.97	NO	NO	YES
10465	7.98	167.79	NO	NO	YES	13660	8.32	166.98	NO	NO	YES
10471	7.99	167.80	NO	NO	YES	13666	8.32	166.99	NO	NO	YES
10477	8.00	167.80	NO	NO	YES	13667	8.31	167.00	NO	NO	YES
10484	8.01	167.81	NO	NO	YES	13671	8.33	167.01	NO	NO	YES
10489	8.06	167.81	NO	NO	YES	13676	8.33	167.02	NO	NO	YES
10490	8.05	167.83	NO	NO	YES	13681	8.34	167.03	NO	NO	YES
10491	8.06	167.83	NO	NO	YES	13686	8.35	167.04	NO	NO	YES
10559	7.98	167.76	NO	NO	YES	13693	8.36	167.06	NO	NO	YES
10560	7.97	167.75	NO	NO	YES	13700	8.36	167.07	NO	NO	YES
10565	7.97	167.77	NO	NO	YES	13707	8.37	167.08	NO	NO	YES
10566	7.96	167.76	NO	NO	YES	13714	8.38	167.09	NO	NO	YES
10572	7.96	167.78	NO	NO	YES	13721	8.38	167.11	NO	NO	YES

Appendix 3: Continued.

SP #	Lat	Lon	Cvr	Cit	DC-8	SP #	Lat	Lon	Cvr	Cit	DC-8
13728	8.39	167.11	NO	NO	YES	15003	9.55	166.96	NO	NO	YES
13729	8.38	167.12	NO	NO	YES	15004	9.53	166.96	NO	NO	YES
13735	8.40	167.13	NO	NO	YES	15017	9.49	166.85	NO	YES	NO
13736	8.39	167.13	NO	NO	YES	15019	9.48	166.84	NO	YES	NO
13742	8.40	167.14	NO	NO	YES	15020	9.47	166.83	NO	YES	NO
13746	8.41	167.15	NO	NO	YES	15338	9.66	168.61	NO	YES	YES
13757	8.38	167.11	NO	YES	YES	15341	9.66	168.60	NO	YES	YES
13758	8.39	167.10	NO	YES	NO	15343	9.66	168.48	NO	YES	YES
13762	8.37	167.09	NO	YES	YES	15348	9.66	168.47	NO	YES	YES
13763	8.38	167.09	NO	YES	NO	15355	9.66	168.46	NO	YES	YES
13769	8.37	167.08	NO	YES	YES	15362	9.66	168.44	NO	YES	YES
13770	8.38	167.07	NO	YES	NO	15369	9.66	168.43	NO	YES	YES
13776	8.36	167.07	NO	YES	YES	15376	9.66	168.41	NO	YES	YES
13777	8.37	167.06	NO	YES	NO	15383	9.66	168.40	NO	YES	YES
13783	8.35	167.06	NO	YES	YES	15390	9.66	168.38	NO	YES	YES
13784	8.36	167.05	NO	YES	NO	15397	9.66	168.37	NO	YES	YES
13790	8.34	167.04	NO	YES	YES	15404	9.66	168.35	NO	YES	YES
13791	8.36	167.04	NO	YES	NO	15411	9.66	168.34	NO	YES	YES
13797	8.34	167.03	NO	YES	YES	15418	9.66	168.33	NO	YES	YES
13798	8.35	167.02	NO	YES	NO	15425	9.66	168.31	NO	YES	YES
13804	8.33	167.02	NO	NO	YES	15432	9.66	168.30	NO	YES	YES
13805	8.34	167.01	NO	YES	YES	15439	9.66	168.29	NO	YES	YES
13811	8.32	167.01	NO	YES	YES	15446	9.66	168.27	NO	YES	YES
13812	8.33	167.00	NO	YES	YES	15453	9.66	168.26	NO	YES	YES
13818	8.32	166.99	NO	YES	YES	15460	9.66	168.24	NO	YES	YES
13819	8.33	166.99	NO	YES	NO	15461	9.68	168.24	NO	YES	NO
13825	8.31	166.98	NO	YES	YES	15467	9.66	168.23	NO	YES	YES
13826	8.32	166.97	NO	YES	NO	15474	9.66	168.22	NO	YES	YES
13832	8.30	166.97	NO	YES	YES	15475	9.68	168.22	NO	YES	NO
13833	8.31	166.96	NO	YES	NO	15481	9.66	168.20	NO	YES	YES
13839	8.29	166.96	NO	YES	YES	15488	9.66	168.19	NO	YES	YES
13840	8.31	166.95	NO	YES	NO	15489	9.68	168.19	NO	YES	NO
13846	8.29	166.94	NO	YES	YES	15495	9.66	168.17	NO	YES	YES
13847	8.30	166.94	NO	YES	NO	15496	9.68	168.17	NO	YES	NO
13853	8.28	166.93	NO	YES	YES	15502	9.66	168.16	NO	YES	YES
13854	8.29	166.92	NO	YES	YES	15503	9.68	168.16	NO	YES	NO
13859	8.27	166.92	NO	YES	YES	15509	9.66	168.15	NO	YES	YES
13860	8.28	166.91	NO	YES	NO	15510	9.68	168.15	NO	YES	NO
13864	8.26	166.91	NO	YES	YES	15516	9.66	168.13	NO	YES	YES
13865	8.28	166.90	NO	YES	YES	15517	9.68	168.13	NO	YES	NO
13868	8.26	166.90	NO	NO	YES	15523	9.66	168.12	NO	YES	YES
13869	8.27	166.89	NO	YES	YES	15524	9.68	168.12	NO	YES	NO
13872	8.25	166.88	NO	YES	YES	15530	9.67	168.11	NO	YES	YES
13873	8.26	166.87	NO	YES	YES	15537	9.66	168.09	NO	YES	YES
13876	8.25	166.86	NO	YES	NO	15544	9.66	168.08	NO	YES	YES
13879	8.25	166.85	NO	YES	YES	15545	9.68	168.08	NO	YES	YES
13880	8.26	166.84	NO	YES	NO	15551	9.66	168.07	NO	YES	YES
13882	8.22	166.85	NO	NO	YES	15558	9.66	168.05	NO	YES	YES
13883	8.24	166.84	NO	YES	YES	15565	9.66	168.04	NO	YES	YES
13884	8.25	166.83	NO	YES	NO	15572	9.66	168.03	NO	YES	YES
14931	9.74	167.17	NO	NO	YES	15573	9.68	168.02	NO	YES	NO
14934	9.75	167.18	NO	NO	YES	15579	9.66	168.01	NO	YES	YES
14936	9.76	167.19	NO	NO	YES	15580	9.68	168.01	NO	YES	NO
14937	9.75	167.20	NO	NO	YES	15586	9.66	168.00	NO	YES	YES
14947	9.74	167.17	NO	NO	YES	15587	9.68	168.00	NO	YES	NO
14950	9.74	167.16	NO	NO	YES	15593	9.66	167.99	NO	YES	YES
14955	9.72	167.16	NO	NO	YES	15594	9.68	167.99	NO	YES	NO
14956	9.73	167.15	NO	NO	YES	15600	9.66	167.97	NO	YES	YES
14958	9.72	167.14	NO	NO	YES	15601	9.68	167.97	NO	YES	NO
14973	9.67	167.09	NO	NO	YES	15611	9.66	167.94	NO	NO	YES
14976	9.66	167.09	NO	NO	YES	15616	9.66	167.93	NO	NO	YES
14977	9.67	167.08	NO	NO	YES	15713	9.67	168.17	NO	YES	NO
14980	9.64	167.08	NO	NO	YES	15720	9.67	168.18	NO	YES	NO
14984	9.65	167.06	NO	NO	YES	15726	9.68	168.20	NO	YES	NO
14987	9.64	167.05	NO	NO	YES	15727	9.66	168.19	NO	YES	NO
14989	9.66	167.03	NO	YES	NO	15733	9.67	168.21	NO	YES	NO
14991	9.65	167.02	NO	YES	NO	15734	9.66	168.21	NO	YES	NO
14993	9.64	167.01	NO	YES	NO	15739	9.67	168.23	NO	YES	NO
14994	9.62	166.99	NO	YES	NO	15740	9.66	168.22	NO	YES	NO
14995	9.61	166.98	NO	YES	NO	15746	9.67	168.24	NO	YES	NO
14996	9.56	166.99	NO	NO	YES	15747	9.66	168.24	NO	YES	NO
14997	9.57	166.98	NO	NO	YES	15811	9.66	168.38	NO	YES	YES
14999	9.55	166.98	NO	NO	YES	15813	9.66	168.37	NO	YES	YES
15002	9.54	166.97	NO	NO	YES	15814	9.68	168.37	NO	YES	NO

Appendix 3: Continued.

SP #	Lat	Lon	Cvr	Cit	DC-8	SP #	Lat	Lon	Cvr	Cit	DC-8
15816	9.66	168.35	NO	YES	YES	16596	9.49	167.85	NO	NO	YES
15820	9.66	168.34	NO	YES	YES	16603	9.50	167.84	NO	NO	YES
15827	9.66	168.33	NO	YES	YES	16610	9.51	167.83	NO	NO	YES
15828	9.67	168.33	NO	YES	YES	16611	9.51	167.84	NO	NO	YES
15834	9.66	168.30	NO	YES	YES	16617	9.52	167.82	NO	NO	YES
15835	9.68	168.30	NO	YES	NO	16618	9.53	167.83	NO	NO	YES
15840	9.65	168.28	YES	NO	NO	16624	9.53	167.81	NO	NO	YES
15841	9.66	168.28	YES	YES	YES	16625	9.54	167.82	NO	NO	YES
15847	9.65	168.27	YES	NO	NO	16631	9.54	167.80	NO	NO	YES
15848	9.66	168.27	YES	YES	YES	16632	9.55	167.81	NO	NO	YES
15849	9.68	168.27	NO	YES	NO	16638	9.55	167.79	NO	NO	YES
15854	9.65	168.26	YES	NO	NO	16642	9.56	167.79	NO	NO	YES
15855	9.66	168.26	YES	YES	YES	16646	9.57	167.78	NO	NO	YES
15856	9.68	168.26	NO	YES	NO	16653	9.58	167.77	NO	NO	YES
15861	9.65	168.24	YES	NO	NO	16654	9.59	167.78	NO	NO	YES
15862	9.66	168.24	YES	YES	YES	16660	9.60	167.76	NO	NO	YES
15863	9.68	168.24	NO	YES	NO	16667	9.61	167.76	NO	NO	YES
15868	9.65	168.23	YES	NO	NO	16668	9.62	167.77	NO	NO	YES
15869	9.66	168.23	YES	YES	YES	16674	9.63	167.76	NO	NO	YES
15870	9.68	168.23	NO	YES	YES	16676	9.64	167.78	NO	YES	NO
15875	9.65	168.22	YES	NO	NO	16682	9.66	167.78	NO	YES	NO
15876	9.66	168.22	YES	YES	YES	16686	9.64	167.73	NO	NO	YES
15877	9.68	168.22	NO	YES	YES	16688	9.66	167.76	NO	YES	NO
15882	9.65	168.20	YES	NO	NO	16689	9.67	167.77	NO	YES	NO
15883	9.66	168.20	YES	YES	YES	16693	9.67	167.72	NO	NO	YES
15884	9.68	168.20	NO	YES	YES	16694	9.67	167.73	NO	NO	YES
15889	9.65	168.19	YES	NO	NO	16695	9.68	167.74	NO	YES	NO
15890	9.66	168.19	YES	YES	YES	16696	9.69	167.75	NO	YES	NO
15891	9.68	168.19	NO	YES	YES	16700	9.67	167.71	NO	NO	YES
15896	9.65	168.17	YES	NO	NO	16701	9.68	167.72	NO	NO	YES
15897	9.67	168.17	YES	YES	YES	16703	9.70	167.75	NO	YES	NO
15903	9.65	168.16	YES	NO	NO	16707	9.69	167.70	NO	NO	YES
15904	9.66	168.16	YES	YES	YES	16710	9.71	167.74	NO	YES	NO
15905	9.68	168.16	NO	YES	YES	16714	9.70	167.70	NO	NO	YES
15910	9.65	168.15	YES	NO	NO	16715	9.71	167.71	NO	NO	YES
15911	9.67	168.15	YES	YES	YES	16717	9.72	167.73	NO	YES	NO
15917	9.65	168.13	YES	NO	NO	16721	9.71	167.69	NO	NO	YES
15918	9.67	168.13	YES	YES	YES	16722	9.72	167.70	NO	NO	YES
15924	9.65	168.12	YES	NO	NO	16724	9.73	167.72	NO	YES	NO
15925	9.66	168.12	YES	YES	YES	16728	9.72	167.68	NO	NO	YES
15931	9.65	168.11	YES	NO	NO	16729	9.73	167.69	NO	NO	YES
15932	9.66	168.11	NO	YES	YES	16735	9.73	167.67	NO	NO	YES
15938	9.65	168.09	YES	NO	NO	16736	9.74	167.68	NO	NO	YES
15939	9.66	168.09	NO	YES	NO	16738	9.76	167.71	NO	YES	NO
15946	9.66	168.08	NO	YES	NO	16742	9.75	167.67	NO	NO	YES
16477	9.29	167.98	NO	NO	YES	16749	9.76	167.66	NO	NO	YES
16484	9.30	167.97	NO	NO	YES	16750	9.77	167.67	NO	NO	YES
16485	9.31	167.98	NO	NO	YES	16756	9.77	167.65	NO	NO	YES
16491	9.31	167.96	NO	NO	YES	16763	9.78	167.64	NO	NO	YES
16498	9.32	167.95	NO	NO	YES	16764	9.79	167.66	NO	NO	YES
16499	9.33	167.97	NO	NO	YES	16770	9.82	167.67	NO	YES	NO
16505	9.33	167.95	NO	NO	YES	16777	9.82	167.63	NO	YES	YES
16512	9.34	167.94	NO	NO	YES	16778	9.83	167.64	NO	YES	NO
16513	9.35	167.95	NO	NO	YES	16782	9.83	167.61	NO	NO	YES
16519	9.35	167.93	NO	NO	YES	16783	9.83	167.62	NO	NO	YES
16520	9.36	167.94	NO	NO	YES	16787	9.84	167.60	NO	NO	YES
16526	9.37	167.92	NO	NO	YES	16792	9.85	167.60	NO	NO	YES
16527	9.37	167.93	NO	NO	YES	16794	9.87	167.62	NO	YES	NO
16533	9.38	167.92	NO	NO	YES	16795	9.88	167.63	NO	YES	NO
16540	9.39	167.91	NO	NO	YES	16799	9.86	167.59	NO	NO	YES
16541	9.40	167.92	NO	NO	YES	16800	9.87	167.60	NO	NO	YES
16547	9.40	167.90	NO	NO	YES	16802	9.89	167.62	NO	YES	NO
16548	9.41	167.91	NO	NO	YES	16806	9.88	167.58	NO	NO	YES
16554	9.41	167.89	NO	NO	YES	16808	9.89	167.60	NO	YES	NO
16561	9.43	167.88	NO	NO	YES	16809	9.90	167.61	NO	YES	NO
16562	9.43	167.89	NO	NO	YES	16813	9.89	167.57	NO	NO	YES
16568	9.44	167.87	NO	NO	YES	16814	9.90	167.58	NO	NO	YES
16569	9.45	167.89	NO	NO	YES	16816	9.91	167.61	NO	YES	NO
16575	9.45	167.86	NO	NO	YES	16820	9.90	167.56	NO	NO	YES
16576	9.45	167.88	NO	NO	YES	16821	9.91	167.57	NO	NO	YES
16582	9.46	167.86	NO	NO	YES	16823	9.92	167.60	NO	YES	NO
16589	9.47	167.85	NO	NO	YES	16827	9.91	167.56	NO	NO	YES
16590	9.48	167.86	NO	NO	YES	16828	9.92	167.57	NO	NO	YES
16595	9.48	167.83	NO	NO	YES	16834	9.92	167.55	NO	NO	YES

SP #	Lat	Lon	Cvr	Cit	DC-8	SP #	Lat	Lon	Cvr	Cit	DC-8
16835	9.93	167.56	NO	NO	YES	17279	9.22	167.83	NO	NO	YES
16841	9.94	167.54	NO	NO	YES	17285	9.20	167.82	NO	NO	YES
16848	9.95	167.53	NO	NO	YES	17286	9.22	167.82	NO	NO	YES
16854	9.96	167.52	NO	NO	YES	17292	9.20	167.81	NO	NO	YES
16859	9.97	167.51	NO	NO	YES	17299	9.20	167.79	NO	NO	YES
16886	9.89	167.61	NO	NO	YES	17306	9.19	167.78	NO	NO	YES
16898	9.84	167.65	NO	YES	NO	17307	9.21	167.78	NO	NO	YES
16901	9.83	167.64	NO	YES	NO	17313	9.19	167.77	NO	NO	YES
16904	9.81	167.64	NO	YES	NO	17314	9.20	167.76	NO	NO	YES
16905	9.81	167.63	NO	NO	YES	17320	9.19	167.75	NO	NO	YES
16909	9.80	167.64	NO	YES	NO	17327	9.18	167.74	NO	NO	YES
16910	9.80	167.63	NO	YES	YES	17328	9.19	167.74	NO	NO	YES
16914	9.79	167.65	NO	YES	NO	17334	9.18	167.73	NO	NO	YES
16915	9.78	167.63	NO	YES	YES	17335	9.19	167.72	NO	NO	YES
16920	9.77	167.64	NO	YES	YES	17341	9.17	167.71	NO	NO	YES
16927	9.75	167.64	NO	YES	YES	17342	9.18	167.71	NO	NO	YES
16934	9.74	167.64	NO	YES	YES	17348	9.17	167.70	NO	NO	YES
16941	9.73	167.65	NO	YES	YES	17355	9.17	167.69	NO	NO	YES
16942	9.72	167.63	NO	NO	YES	17362	9.16	167.67	NO	NO	YES
16948	9.71	167.65	NO	YES	YES	17368	9.16	167.66	NO	NO	YES
16955	9.70	167.65	NO	YES	YES	17410	9.20	167.78	YES	NO	NO
16962	9.69	167.66	NO	YES	YES	17417	9.21	167.80	YES	NO	NO
16963	9.68	167.64	NO	YES	NO	17418	9.20	167.81	YES	NO	NO
16969	9.67	167.66	NO	YES	YES	17422	9.21	167.82	YES	NO	NO
16986	9.59	167.68	NO	YES	YES	17426	9.22	167.83	YES	YES	NO
16991	9.57	167.68	NO	YES	YES	17427	9.21	167.85	YES	YES	NO
16997	9.56	167.69	NO	YES	YES	17430	9.20	167.81	YES	YES	NO
17002	9.55	167.69	NO	YES	YES	17447	8.49	167.37	YES	NO	NO
17009	9.53	167.69	NO	YES	YES	17449	8.46	167.39	YES	NO	NO
17016	9.52	167.69	NO	YES	YES	17450	8.47	167.37	YES	NO	NO
17023	9.50	167.70	NO	YES	YES	17455	8.45	167.38	YES	NO	NO
17030	9.49	167.70	NO	YES	YES	17456	8.45	167.37	YES	NO	NO
17037	9.48	167.71	NO	YES	YES	17462	8.44	167.36	YES	NO	NO
17044	9.46	167.71	NO	YES	YES	17468	8.42	167.36	YES	NO	NO
17051	9.45	167.71	NO	YES	YES	17469	8.43	167.35	YES	NO	NO
17058	9.44	167.72	NO	YES	YES	17475	8.41	167.35	YES	NO	NO
17065	9.42	167.72	NO	YES	YES	17476	8.42	167.34	YES	NO	NO
17072	9.41	167.72	NO	YES	YES	17483	8.41	167.33	YES	NO	NO
17079	9.39	167.73	NO	YES	YES	17575	8.37	167.30	NO	NO	YES
17086	9.38	167.73	NO	YES	YES	17580	8.39	167.31	YES	NO	YES
17093	9.36	167.73	NO	YES	YES	17583	8.40	167.31	NO	YES	NO
17100	9.35	167.74	NO	YES	YES	17584	8.40	167.32	YES	YES	YES
17107	9.34	167.74	NO	YES	YES	17587	8.41	167.32	NO	YES	NO
17108	9.33	167.73	NO	YES	NO	17590	8.43	167.33	NO	YES	NO
17114	9.32	167.75	NO	YES	YES	17594	8.42	167.23	NO	YES	NO
17115	9.32	167.73	NO	NO	YES	17902	8.11	167.03	NO	YES	NO
17121	9.31	167.75	NO	YES	YES	17903	8.10	167.04	NO	YES	NO
17128	9.30	167.75	NO	YES	YES	17905	8.12	167.04	NO	YES	NO
17135	9.28	167.75	NO	YES	YES	17906	8.11	167.05	YES	YES	NO
17142	9.27	167.76	NO	YES	YES	17911	8.12	167.06	YES	YES	YES
17148	9.26	167.77	NO	YES	NO	17912	8.12	167.07	NO	NO	YES
17149	9.25	167.76	NO	YES	YES	17916	8.15	167.03	NO	YES	NO
17156	9.24	167.76	NO	YES	YES	17918	8.14	167.06	YES	YES	YES
17163	9.23	167.77	NO	YES	YES	17919	8.13	167.07	NO	YES	YES
17170	9.21	167.77	NO	YES	YES	17923	8.16	167.04	NO	YES	NO
17177	9.20	167.78	NO	YES	YES	17924	8.16	167.05	NO	YES	NO
17184	9.19	167.78	NO	YES	YES	17925	8.15	167.06	YES	YES	YES
17191	9.17	167.78	NO	YES	YES	17926	8.15	167.08	NO	YES	YES
17197	9.16	167.80	NO	NO	YES	17931	8.17	167.06	YES	NO	NO
17198	9.16	167.78	NO	YES	YES	17932	8.16	167.07	YES	YES	YES
17221	9.24	167.95	NO	NO	YES	17933	8.16	167.08	NO	YES	YES
17224	9.24	167.94	NO	NO	YES	17939	8.18	167.07	NO	YES	YES
17230	9.23	167.93	NO	NO	YES	17940	8.17	167.09	NO	YES	YES
17231	9.25	167.92	NO	NO	YES	17946	8.19	167.08	YES	YES	NO
17237	9.23	167.91	NO	NO	YES	17947	8.19	167.09	NO	YES	YES
17238	9.24	167.91	NO	NO	YES	17953	8.20	167.08	YES	YES	NO
17244	9.23	167.90	NO	NO	YES	17954	8.20	167.09	YES	YES	YES
17251	9.23	167.89	NO	NO	YES	17955	8.19	167.11	NO	NO	YES
17258	9.22	167.87	NO	NO	YES	17960	8.22	167.09	YES	YES	NO
17265	9.21	167.86	NO	NO	YES	17961	8.21	167.10	YES	YES	YES
17266	9.23	167.86	NO	NO	YES	17967	8.23	167.09	YES	YES	NO
17271	9.21	167.85	NO	NO	YES	17968	8.22	167.10	YES	YES	YES
17272	9.22	167.84	NO	NO	YES	17969	8.22	167.12	NO	NO	YES
17278	9.21	167.83	NO	NO	YES	17974	8.24	167.10	YES	YES	NO

Appendix 3: Continued.

SP #	Lat	Lon	Cvr	Cit	DC-8	SP #	Lat	Lon	Cvr	Cit	DC-8
17975	8.23	167.11	NO	YES	YES	18819	7.55	168.27	YES	NO	NO
17981	8.26	167.10	YES	YES	NO	18820	7.56	168.27	NO	NO	YES
17982	8.25	167.12	YES	YES	YES	18822	7.54	168.25	YES	NO	NO
17988	8.27	167.11	YES	NO	NO	18823	7.55	168.26	YES	NO	NO
17989	8.26	167.12	YES	YES	YES	18824	7.57	168.26	NO	NO	YES
17993	8.28	167.11	NO	YES	NO	18827	7.54	168.24	YES	NO	NO
17994	8.28	167.13	YES	YES	YES	18828	7.56	168.25	YES	NO	NO
17999	8.29	167.13	YES	YES	YES	18829	7.57	168.25	NO	NO	YES
18005	8.30	167.14	YES	YES	YES	18834	7.56	168.23	YES	NO	NO
18010	8.32	167.14	YES	YES	YES	18835	7.57	168.24	NO	NO	YES
18014	8.33	167.13	YES	YES	NO	18841	7.58	168.22	NO	NO	YES
18015	8.33	167.15	YES	YES	YES	18847	7.58	168.21	NO	NO	YES
18019	8.34	167.14	YES	YES	NO	18850	7.62	168.22	YES	NO	NO
18020	8.34	167.15	YES	YES	YES	18854	7.58	168.20	NO	NO	YES
18024	8.35	167.16	YES	YES	YES	18855	7.60	168.20	NO	NO	YES
18529	7.57	168.60	NO	NO	YES	18857	7.63	168.21	YES	NO	NO
18531	7.57	168.58	NO	NO	YES	18860	7.59	168.18	NO	NO	YES
18532	7.58	168.59	NO	NO	YES	18861	7.60	168.19	NO	NO	YES
18535	7.58	168.57	NO	NO	YES	18863	7.63	168.19	YES	NO	NO
18539	7.58	168.56	NO	NO	YES	18867	7.59	168.17	NO	NO	YES
18543	7.59	168.55	NO	NO	YES	18873	7.59	168.16	NO	NO	YES
18550	7.62	168.53	NO	NO	YES	18878	7.60	168.15	NO	NO	YES
18553	7.62	168.52	NO	NO	YES	18882	7.60	168.13	NO	NO	YES
18575	7.68	168.41	NO	NO	YES	18886	7.60	168.12	NO	NO	YES
18578	7.68	168.39	NO	NO	YES	18888	7.64	168.07	NO	NO	YES
18583	7.68	168.38	NO	NO	YES	18889	7.63	168.07	NO	NO	YES
18584	7.70	168.39	NO	NO	YES	18893	7.62	168.08	NO	NO	YES
18588	7.69	168.37	NO	NO	YES	18896	7.62	168.10	NO	NO	YES
18594	7.70	168.36	NO	NO	YES	20250	7.86	167.58	NO	NO	YES
18595	7.71	168.37	NO	NO	YES	20255	7.87	167.56	NO	NO	YES
18599	7.71	168.35	NO	NO	YES	20260	7.88	167.53	NO	NO	YES
18604	7.71	168.34	NO	NO	YES	20265	7.88	167.52	NO	NO	YES
18605	7.73	168.34	NO	NO	YES	20272	7.88	167.51	NO	NO	YES
18609	7.72	168.33	NO	NO	YES	20273	7.90	167.51	NO	NO	YES
18613	7.73	168.31	NO	NO	YES	20279	7.89	167.49	NO	NO	YES
18614	7.74	168.32	NO	NO	YES	20285	7.90	167.48	NO	NO	YES
18615	7.73	168.30	NO	NO	YES	20290	7.90	167.47	NO	NO	YES
18618	7.75	168.29	NO	NO	YES	20297	7.91	167.45	NO	NO	YES
18622	7.74	168.30	NO	NO	YES	20304	7.91	167.44	NO	NO	YES
18626	7.73	168.31	NO	NO	YES	20305	7.92	167.44	NO	NO	YES
18630	7.72	168.33	NO	NO	YES	20310	7.91	167.42	NO	NO	YES
18635	7.72	168.34	NO	NO	YES	20311	7.92	167.42	NO	NO	YES
18636	7.71	168.33	NO	NO	YES	20318	7.92	167.41	NO	NO	YES
18640	7.71	168.35	NO	NO	YES	20325	7.93	167.40	NO	NO	YES
18646	7.70	168.37	NO	NO	YES	20332	7.93	167.38	NO	NO	YES
18647	7.69	168.36	NO	NO	YES	20333	7.94	167.39	NO	NO	YES
18651	7.69	168.38	NO	NO	YES	20339	7.93	167.37	NO	NO	YES
18652	7.68	168.37	NO	NO	YES	20340	7.94	167.37	NO	NO	YES
18657	7.69	168.39	NO	NO	YES	20344	7.94	167.35	NO	NO	YES
18658	7.68	168.39	NO	NO	YES	20345	7.95	167.36	NO	NO	YES
18662	7.68	168.41	NO	NO	YES	20348	7.96	167.34	NO	NO	YES
18664	7.65	168.39	YES	NO	NO	20351	7.96	167.33	NO	NO	YES
18668	7.67	168.42	NO	NO	YES	20909	8.11	168.34	NO	NO	YES
18669	7.66	168.41	YES	NO	YES	20910	8.12	168.35	NO	NO	YES
18670	7.65	168.40	YES	NO	NO	20915	8.16	168.31	NO	NO	YES
18674	7.66	168.43	NO	NO	YES	20922	8.19	168.26	NO	NO	YES
18675	7.65	168.42	YES	NO	NO	20923	8.20	168.27	NO	NO	YES
18679	7.66	168.44	NO	NO	YES	20929	8.20	168.25	NO	NO	YES
18680	7.64	168.44	YES	NO	NO	20930	8.21	168.27	NO	NO	YES
18684	7.65	168.46	NO	NO	YES	20936	8.21	168.25	NO	NO	YES
18685	7.64	168.45	YES	NO	YES	20937	8.22	168.26	NO	NO	YES
18689	7.64	168.47	NO	NO	YES	20943	8.22	168.24	NO	NO	YES
18693	7.63	168.48	NO	NO	YES	20944	8.23	168.25	NO	NO	YES
18697	7.62	168.50	NO	NO	YES	20950	8.23	168.23	NO	NO	YES
18700	7.59	168.49	YES	NO	NO	20951	8.24	168.24	NO	NO	YES
18709	7.70	168.25	YES	NO	NO	20957	8.25	168.22	NO	NO	YES
18710	7.70	168.26	YES	NO	NO	20964	8.26	168.21	NO	NO	YES
18711	7.70	168.28	YES	NO	NO	20965	8.27	168.22	NO	NO	YES
18712	7.69	168.29	YES	NO	NO	20971	8.27	168.20	NO	NO	YES
18755	7.67	168.11	YES	NO	NO	20978	8.28	168.20	NO	NO	YES
18756	7.66	168.11	YES	NO	NO	20985	8.29	168.19	NO	NO	YES
18759	7.65	168.12	YES	NO	NO	20986	8.30	168.20	NO	NO	YES
18762	7.65	168.14	YES	NO	NO	20992	8.30	168.17	NO	NO	YES
18816	7.54	168.28	YES	NO	NO	20993	8.31	168.19	NO	NO	YES

SP #	Lat	Lon	Cvr	Cit	DC-8	SP #	Lat	Lon	Cvr	Cit	DC-8
20999	8.31	168.17	NO	NO	YES	21851	8.10	168.12	NO	NO	YES
21000	8.32	168.18	NO	NO	YES	21855	8.09	168.13	NO	NO	YES
21006	8.32	168.16	NO	NO	YES	21858	8.08	168.15	NO	NO	YES
21013	8.33	168.15	NO	NO	YES	21862	8.07	168.15	NO	NO	YES
21014	8.34	168.16	NO	NO	YES	21863	8.06	168.14	NO	NO	YES
21019	8.34	168.14	NO	NO	YES	21866	8.06	168.16	NO	NO	YES
21024	8.35	168.13	NO	NO	YES	21871	8.05	168.17	NO	NO	YES
21030	8.36	168.12	NO	NO	YES	21876	8.04	168.18	NO	NO	YES
21031	8.37	168.13	NO	NO	YES	21881	8.03	168.19	NO	NO	YES
21035	8.37	168.11	NO	NO	YES	21967	7.86	168.27	NO	NO	YES
21040	8.39	168.10	NO	NO	YES	21974	7.87	168.26	NO	NO	YES
21041	8.39	168.11	NO	NO	YES	21975	7.88	168.28	NO	NO	YES
21044	8.39	168.09	NO	NO	YES	21981	7.88	168.26	NO	NO	YES
21045	8.40	168.10	NO	NO	YES	21982	7.89	168.27	NO	NO	YES
21049	8.50	168.22	NO	NO	YES	21988	7.90	168.25	NO	NO	YES
21050	8.49	168.21	NO	NO	YES	21994	7.91	168.24	NO	NO	YES
21060	8.24	168.39	NO	NO	YES	21995	7.92	168.25	NO	NO	YES
21065	8.22	168.41	NO	NO	YES	22001	7.92	168.23	NO	NO	YES
21067	8.21	168.43	NO	NO	YES	22008	7.93	168.22	NO	NO	YES
21070	8.20	168.44	NO	NO	YES	22009	7.94	168.23	NO	NO	YES
21072	8.19	168.45	NO	NO	YES	22015	7.94	168.21	NO	NO	YES
21080	8.16	168.48	NO	NO	YES	22021	7.95	168.20	NO	NO	YES
21081	8.15	168.47	NO	NO	YES	22022	7.96	168.21	NO	NO	YES
21087	8.14	168.49	NO	NO	YES	22028	7.96	168.19	NO	NO	YES
21088	8.13	168.48	NO	NO	YES	22029	7.97	168.20	NO	NO	YES
21094	8.13	168.50	NO	NO	YES	22035	7.97	168.18	NO	NO	YES
21115	8.10	168.41	NO	NO	YES	22042	7.98	168.18	NO	NO	YES
21122	8.11	168.39	NO	NO	YES	22049	7.99	168.17	NO	NO	YES
21138	8.18	168.36	NO	NO	YES	22050	8.00	168.18	NO	NO	YES
21145	8.20	168.33	NO	NO	YES	22056	8.01	168.16	NO	NO	YES
21148	8.21	168.32	NO	NO	YES	22061	8.02	168.15	NO	NO	YES
21152	8.22	168.31	NO	NO	YES	23643	8.69	168.73	NO	NO	YES
21384	8.00	168.38	NO	NO	YES	23647	8.70	168.72	NO	NO	YES
21388	8.02	168.37	NO	NO	YES	23648	8.70	168.73	NO	NO	YES
21393	8.03	168.36	NO	NO	YES	23653	8.71	168.71	NO	NO	YES
21397	8.04	168.35	NO	NO	YES	23654	8.72	168.73	NO	NO	YES
21401	8.05	168.34	NO	NO	YES	23660	8.73	168.71	NO	NO	YES
21437	8.18	168.23	NO	NO	YES	23661	8.73	168.72	NO	NO	YES
21438	8.19	168.23	NO	NO	YES	23667	8.74	168.70	NO	NO	YES
21442	8.20	168.22	NO	NO	YES	23668	8.74	168.72	NO	NO	YES
21451	8.22	168.18	NO	NO	YES	23674	8.75	168.70	NO	NO	YES
21462	8.28	168.14	NO	NO	YES	23680	8.77	168.69	NO	NO	YES
21466	8.30	168.14	NO	NO	YES	23681	8.77	168.71	NO	NO	YES
21470	8.30	168.13	NO	NO	YES	23686	8.78	168.69	NO	NO	YES
21474	8.31	168.12	NO	NO	YES	23692	8.79	168.69	NO	NO	YES
21479	8.33	168.11	NO	NO	YES	23698	8.81	168.68	NO	NO	YES
21484	8.34	168.10	NO	NO	YES	23699	8.81	168.69	NO	NO	YES
21485	8.35	168.11	NO	NO	YES	23702	8.83	168.69	NO	NO	YES
21639	7.94	168.34	NO	NO	YES	23706	8.84	168.68	NO	NO	YES
21645	7.95	168.33	NO	NO	YES	23708	8.86	168.68	NO	NO	YES
21651	7.96	168.33	NO	NO	YES	23712	8.94	168.65	NO	NO	YES
21652	7.97	168.34	NO	NO	YES	23722	8.98	168.64	NO	NO	YES
21655	7.97	168.32	NO	NO	YES	25238	8.56	167.23	NO	YES	NO
21660	7.98	168.31	NO	NO	YES	25245	8.57	167.23	NO	YES	NO
21661	7.99	168.32	NO	NO	YES	25252	8.58	167.22	NO	YES	NO
21664	7.99	168.29	NO	NO	YES	25253	8.59	167.23	NO	YES	NO
21665	8.00	168.30	NO	NO	YES	25259	8.59	167.21	NO	YES	NO
21670	8.01	168.29	NO	NO	YES	25260	8.60	167.22	NO	YES	NO
21675	8.02	168.28	NO	NO	YES	25267	8.61	167.21	NO	YES	NO
21676	8.03	168.29	NO	NO	YES	25274	8.62	167.21	NO	YES	NO
21680	8.03	168.27	NO	NO	YES	25281	8.63	167.20	NO	YES	NO
21686	8.04	168.26	NO	NO	YES	25288	8.64	167.19	NO	YES	NO
21704	8.12	168.21	NO	NO	YES	25289	8.65	167.20	NO	YES	NO
21819	8.22	168.03	NO	NO	YES	25295	8.66	167.18	NO	YES	NO
21823	8.21	168.04	NO	NO	YES	25296	8.66	167.20	NO	YES	NO
21824	8.20	168.03	NO	NO	YES	25302	8.67	167.17	NO	YES	NO
21827	8.20	168.05	NO	NO	YES	25303	8.68	167.19	NO	YES	NO
21828	8.19	168.04	NO	NO	YES	25309	8.68	167.17	NO	YES	NO
21831	8.19	168.06	NO	NO	YES	25310	8.69	167.18	NO	YES	NO
21832	8.18	168.05	NO	NO	YES	25316	8.69	167.16	NO	YES	NO
21835	8.17	168.07	NO	NO	YES	25317	8.70	167.17	NO	YES	NO
21839	8.15	168.07	NO	NO	YES	25322	8.70	167.15	NO	YES	NO
21850	8.11	168.13	NO	NO	YES	25323	8.71	167.16	NO	YES	NO
21854	8.10	168.14	NO	NO	YES	25329	8.72	167.15	NO	YES	NO

Appendix 3: Continued.

SP #	Lat	Lon	Cvr	Cit	DC-8	SP #	Lat	Lon	Cvr	Cit	DC-8
25334	8.72	167.13	NO	YES	NO	36131	8.46	167.51	NO	NO	YES
25335	8.73	167.15	NO	YES	NO	36135	8.46	167.49	NO	NO	YES
25341	8.74	167.14	NO	YES	NO	36136	8.47	167.48	NO	NO	YES
25347	8.76	167.13	NO	YES	NO	39084	7.65	166.97	NO	NO	YES
25353	8.77	167.12	NO	YES	NO	39087	7.65	166.96	NO	NO	YES
25359	8.78	167.11	NO	YES	NO	39096	7.62	166.92	NO	NO	YES
25364	8.79	167.11	NO	YES	NO	39097	7.63	166.92	NO	NO	YES
25369	8.80	167.10	NO	YES	NO	39101	7.62	166.91	NO	NO	YES
25375	8.81	167.09	NO	YES	NO	39105	7.60	166.90	NO	NO	YES
25380	8.82	167.07	NO	YES	NO	39106	7.62	166.89	NO	NO	YES
25381	8.83	167.08	NO	YES	NO	39111	7.61	166.88	NO	NO	YES
25386	8.84	167.07	NO	YES	NO	39115	7.60	166.87	NO	NO	YES
25390	8.85	167.06	NO	YES	NO	39116	7.61	166.86	NO	NO	YES
25394	8.86	167.06	NO	YES	NO	39119	7.60	166.86	NO	NO	YES
25398	8.87	167.05	NO	YES	NO	39120	7.61	166.85	NO	NO	YES
25402	8.88	167.04	NO	YES	NO	39124	7.60	166.76	NO	NO	YES
25406	8.90	167.03	NO	YES	NO	39127	7.61	166.78	NO	NO	YES
25413	8.91	167.02	NO	YES	NO	39133	7.61	166.79	NO	NO	YES
25420	8.92	167.01	NO	YES	NO	39136	7.57	166.80	NO	NO	YES
25427	8.93	167.01	NO	YES	NO	39140	7.62	166.80	NO	NO	YES
25434	8.94	167.00	NO	YES	NO	39147	7.62	166.81	NO	NO	YES
25435	8.95	167.01	NO	YES	NO	39148	7.61	166.82	NO	NO	YES
25441	8.95	166.99	NO	YES	NO	39154	7.63	166.83	NO	NO	YES
25448	8.96	166.98	NO	YES	NO	39159	7.63	166.84	NO	NO	YES
25455	8.97	166.97	NO	YES	NO	39160	7.62	166.84	NO	NO	YES
25462	8.98	166.97	NO	YES	NO	39165	7.64	166.85	NO	NO	YES
25463	8.99	166.98	NO	YES	NO	39171	7.64	166.87	NO	NO	YES
25468	8.89	167.02	NO	YES	NO	39172	7.63	166.87	NO	NO	YES
31383	7.35	168.10	NO	NO	YES	39178	7.65	166.88	NO	NO	YES
31387	7.35	168.11	NO	NO	YES	39179	7.63	166.88	NO	NO	YES
31391	7.36	168.13	NO	NO	YES	39184	7.66	166.89	NO	NO	YES
31396	7.37	168.14	NO	NO	YES	39185	7.65	166.89	NO	NO	YES
31400	7.37	168.15	NO	NO	YES	39190	7.65	166.91	NO	NO	YES
31405	7.38	168.16	NO	NO	YES	39195	7.66	166.92	NO	NO	YES
31412	7.39	168.18	NO	NO	YES	39200	7.67	166.93	NO	NO	YES
31419	7.39	168.19	NO	NO	YES	39205	7.67	166.94	NO	NO	YES
31420	7.38	168.20	NO	NO	YES	39572	8.36	167.90	NO	NO	YES
31426	7.40	168.20	NO	NO	YES	39575	8.35	167.90	NO	NO	YES
31432	7.41	168.23	NO	NO	YES	39579	8.34	167.90	NO	NO	YES
31438	7.42	168.24	NO	NO	YES	39987	7.61	167.29	NO	YES	NO
31439	7.41	168.25	NO	NO	YES	39988	7.60	167.30	NO	YES	NO
31444	7.43	168.25	NO	NO	YES	39989	7.64	167.29	NO	NO	YES
31445	7.41	168.26	NO	NO	YES	39991	7.62	167.30	NO	YES	NO
31450	7.43	168.26	NO	NO	YES	39992	7.65	167.30	NO	NO	YES
31455	7.43	168.28	NO	NO	YES	39993	7.64	167.31	NO	NO	YES
31460	7.44	168.29	NO	NO	YES	39995	7.66	167.31	NO	NO	YES
31466	7.45	168.30	NO	NO	YES	39998	7.66	167.32	NO	NO	YES
31472	7.49	168.39	NO	NO	YES	40001	7.68	167.33	NO	NO	YES
31478	7.50	168.40	NO	NO	YES	40002	7.67	167.34	NO	NO	YES
31485	7.51	168.41	NO	NO	YES	40005	7.68	167.35	NO	NO	YES
31490	7.51	168.43	NO	NO	YES	40008	7.68	167.36	NO	NO	YES
31494	7.52	168.44	NO	NO	YES	40009	7.67	167.37	NO	NO	YES
31500	7.53	168.45	NO	NO	YES	40012	7.69	167.37	NO	NO	YES
31507	7.53	168.46	NO	NO	YES	40013	7.68	167.38	NO	NO	YES
31513	7.54	168.47	NO	NO	YES	40014	7.67	167.39	NO	YES	NO
31518	7.55	168.49	NO	NO	YES	40015	7.66	167.39	NO	YES	NO
31523	7.55	168.50	NO	NO	YES	40018	7.70	167.38	NO	NO	YES
31528	7.56	168.52	NO	NO	YES	40019	7.69	167.39	NO	NO	YES
31533	7.57	168.53	NO	NO	YES	40020	7.68	167.40	NO	YES	NO
31534	7.56	168.53	NO	NO	YES	40024	7.72	167.39	NO	NO	YES
31539	7.58	168.54	NO	NO	YES	40025	7.70	167.40	NO	NO	YES
31540	7.56	168.55	NO	NO	YES	40026	7.69	167.41	NO	YES	NO
31546	7.58	168.55	NO	NO	YES	40027	7.68	167.41	NO	YES	NO
31553	7.59	168.57	NO	NO	YES	40030	7.72	167.41	NO	NO	YES
31554	7.58	168.57	NO	NO	YES	40031	7.71	167.41	NO	YES	YES
36117	8.55	167.65	NO	NO	YES	40032	7.70	167.42	NO	YES	NO
36120	8.54	167.64	NO	NO	YES	40038	7.72	167.42	NO	YES	YES
36123	8.54	167.63	NO	NO	YES	40039	7.71	167.43	NO	YES	NO
36126	8.53	167.62	NO	NO	YES	40041	7.74	167.43	NO	YES	NO
40042	7.73	167.43	NO	YES	YES	40044	7.75	167.44	NO	YES	NO

List of Tables

Table 1: KWAJEX aircraft operations daily flight summary.

Flt	Date	Flight Time Blocks (LE, M, A, EE)	Overpass (LE, M, A, EE) (Zipser Code)	Overpass Rating (1, 2) PR / TMI or Bust (B)	Data Quality (T, 0, 1, 2)	Aircraft
1	Jul 26	M A	M (2) EE (5)	B	T / 2	Con
2	Jul 27	M	-	-	T / 0	Cit
3	Jul 28	A EE	M (3) EE (3)	2 (PR)	2	Con
	Jul 29	-	-	-	-	(1) No Fly
4	Jul 30	A	M (5) EE (1)	B	T / 2	DC8 – Con
	Jul 31	-	LE (4)	-	-	(2) No Fly
5	Aug 1	EE	EE (4)	2 (TMI)	T / 2	Cit – Con
6	Aug 2	A	LE (3) A (6)	B	0	Con
7	Aug 3	A	A (6)	B	2	DC8 – Con
	Aug 4	-	LE (2) A (4)	-	-	(3) No Fly
	Aug 5	-	-	-	-	(4) No Fly
8	Aug 6	A	LE (4) A (2)	2 (PR)	2	DC8 – Con
	Aug 7	-	LE (5)	-	-	(5) No Fly
9	Aug 8	A	A (2)	B	0	Con
	Aug 9	-	EE (4)	-	-	(6) No Fly
10	Aug 10	M A	-	-	2	DC8 – Con
11		A	A (5)	B	T / 2	Cit
	Aug 11	-	LE (1) A (5)	-	-	(7) No Fly
12	Aug 12	M A	-	-	2	DC8 – Cit/Con
13	Aug 13	A	LE (3) A (3)	B	0	Cit
	Aug 14	-	EE (5)	-	-	(8) No Fly
14	Aug 15	M A	A (2) EE (4)	2 (PR)	2	DC8 – Cit
	Aug 16	-	-	-	-	(9) No Fly
15	Aug 17	M	M (4) EE (2)	B	0	DC8 – Cit
16	Aug 18	M	M (6)	2 (TMI)	2	DC8 – Cit
17		A	-	-	2	Cit
	Aug 19	-	M (6) EE (2)	-	-	(10) No Fly
18	Aug 20	M	M (4)	2 (TMI)	2	DC8 – Cit
	Aug 21	-	EE (4)	-	-	(11) No Fly
	Aug 22	-	M (1) A (5)	-	-	(12) No Fly
19	Aug 23	M	-	-	2	DC8 – Cit
20		A	-	-	2	DC8 – Cit/Con
21	Aug 24	A	M (3) A (3)	1 (TMI)	2	DC8 – Cit/Con
22	Aug 25	A	-	-	2	DC8 – Cit/Con
23	Aug 26	A	M (5) A (1)	2 (PR)	2	DC8 – Cit/Con
	Aug 27	-	LE (4)	-	-	(13) No Fly

Table 1: Continued.

Flt	Date	Flight Time Blocks (LE, M, A, EE)	Overpass (LE, M, A, EE) (Zipser Code)	Overpass Rating (1, 2) PR / TMI or Bust (B)	Data Quality (T, 0, 1, 2)	Aircraft
24	Aug 28	M	-	-	T / 2	Con
25		A	A (4)	B	2	DC8-Cit/Con
26	Aug 29	M A	LE (3) A (6)	B	2	DC8 - Cit
27	Aug 30	A	A (6)	2 (TMI)	2	Con
28	Aug 31	M A	LE (2) A (4)	2 (TMI)	2	DC8 - Cit
	Sep 1	-	-	-	-	(14) No Fly
29	Sep 2	M → A	LE (4) A (2)	2 (TMI)	1	DC8 - Cit
30	Sep 3	M	LE (5)	-	2	DC8 - Cit
31		A	-	-	2	DC8 - Cit
	Sep 4	-	A (4)	-	-	(15) No Fly
32	Sep 5	M	LE (3)	B	2	DC8
33	Sep 6	M → A	M (5)	1 (TMI)	1	DC8 - Cit
	Sep 7	-	LE (1) M (5)	-	-	(16) No Fly
34	Sep 8	M → A	EE (4)	B	2	DC8 - Cit
35	Sep 9	M	M (3) EE (6)	1 (PR)	2	DC8 - Cit
	Sep 10	-	EE (6)	-	-	(17) No Fly
36	Sep 11	M → A	M (2) EE (4)	2 (PR)	2	DC8 - Cit
37	Sep 12	M	-	-	2	DC8 - Cit
38	Sep 13	M	M (4) EE (2)	B	1	DC8
39	Sep 14	A	M (6)	B	2	DC8 - Cit
	Sep 15	-	EE (3)	-	-	(18) No Fly

LE is late evening (~0100-0700)   M is morning (~0700-1300)
A is afternoon (~1300-1900)   EE is early evening (~1900-0100)
B for "Bust"   T for "Test Flight"
0 for no science data   1 for marginal science data   2 for good to excellent science data
Zipser Scale: 1 (>75% PR cover);   2 (50-75% PR cover);   3 (25-50% PR cover)
          4 (>75% TMI cover);   5 (50-75% TMI cover);   6 (25-50% TMI cover)

Table 2: Aircraft component of matched-merged microphysics dataset.

COLUMN #	PARAMETER	UNITS	SOURCE	NOTES
1	Year	YYYY	superpixel	
2	Month	MM	superpixel	
3	Day	DD	superpixel	
4	Hour	HH	superpixel	
5	Minute	MM	superpixel	
6	Second	SS	superpixel	
7	Latitude	DDD.ddd	superpixel	
8	Longitude	sDDD.ddd	superpixel	
9	Altitude	m	a/c CMPD	
10	Temperature	^{o}C	a/c CMPD	
11	Pressure	hPa	a/c CMPD	
12	Dewpoint	^{o}C	a/c CMPD	
13	Cloud LWC	g m^{-3}	a/c CMPD	
14	Precipitation LWC	g m^{-3}	a/c CMPD	Calculated from Eqn (10) for Convair points > +5 C
15	Total Precipitation IWC	g m^{-3}	a/c CMPD	Indeterminate ice = total – other habits
16	Graupel IWC	g m^{-3}	a/c CMPD	
17	Aggregate IWC	g m^{-3}	a/c CMPD	
18	Needle/Column IWC	g m^{-3}	a/c CMPD	
19	Reflectivity	dBZ	a/c CMPD	
20	Effective Water Radius	μm	Equation (8)	Set to zero for DC-8
21	Effective Ice Radius	μm	Equation (8)	
22	Effective Water Variance	dimensionless	Equation (9)	Set to zero for DC-8
23	Effective Ice Variance	dimensionless	Equation (9)	
24	Convair Reflectivity	dBZ	Equation (11)	At Convair points > +5 C
25	Convair Rainrate	mm h^{-1}	Equations (12) & (13)	At Convair points > +5 C

List of Figures

Figure 10a: Top panel shows GV-radar convective/stratiform mapping plotted by convective/stratiform index (CSI) vs. superpixel number. Bottom panel shows variation of convective superpixel fraction with changes in CSI.

Figure 10b: Top panel shows GV-radar convective/stratiform mapping plotted in *E-S* space. Bottom panel shows *E-S* space separation of convective and stratiform superpixels using convective fraction values > 0.5 = convective (or CSI > 0.31 = convective).

Figure 11a: Comparison of 2A-12-derived (blue plot) and GV-radar-derived (red plot) rainrates at matched HQ GV-radar superpixels. [HQ indicates high resolution range (range < 78 km) and best interpolation quality (interpolation quality = 8).]

Figure 11b: Top panel shows scatter diagram of 2A-12 and GV-radar rainrates equivalent to those given in Fig. 11a. Bottom 2 panels show individual histograms.

Figure 12: Left three panels show comparisons involving 2A-25 rainrates with respect to GV-radar (top-left), 2A-12 (middle-left), and ARMAR (bottom-left) rainrates vs. matched HQ or QC superpixel number. Right three panels show corresponding scatter diagrams.

Figure 13:   Rainrate (top two panels) and liquid water content (bottom two panels) intercomparisons and scatter diagrams of 2A-25- vs. Convair-derived values in 2-3 km layer. Convair rainrates and LWCs recalculated from particle size spectra after conversion of ice artifacts to liquid water spheres. 2A-25 LWCs calculated from rainrates assuming Marshall-Palmer distribution.

Figure 14:   Top panel shows *E-S* diagram of all merged-matched aircraft priority leg microphysical measurements. Bottom panel shows *E-S* diagram of only those superpixels where Convair observations match up with one or both of other aircraft observations -- these points are used to produce total column microphysical profiles.

Figure 15: Total water content ice fraction vs. outside air temperature for all matched Convair and Citation measurements. Top panel shows diagram of unrealistic ice fraction values in Convair data at temperatures > +5 ^{o}C, whereas bottom panel shows same diagram after Convair ice artifacts are converted to liquid water spheres.

Figure 16: Scatter diagram and histogram comparisons of reflectivity calculated from aircraft particle spectra vs. ARMAR. Left panels show ARMAR vs. Convair in 2-3 km layer, whereas right panels show ARMAR vs. Citation in 6-7 km layer. Convair reflectivities are calculated after ice artifact conversion to liquid water.

Figure 17a: Scatter diagrams of 2A-12 vs. aircraft-observed LWCs in 0-4 km layer (left two panels—Convair) and 5-10 km layer (right two panels -- Citation). Rainrate differences color-coded according to GV-radar minus 2A-12 rainrate differences.

Figure 17b: Scatter diagrams of 2A-12 vs. aircraft-observed IWCs in layers specified. Rainrate differences color-coded as in Fig. 17a.

Figure 18: Six outside panels show observed minus assumed column average microphysical parameter differences vs. GV-radar minus 2A-12 rainrate differences (six outside panels) with respect to liquid and ice. Single center panel shows scatter diagram of 2A-12 vs. GV-radar rainrate, highlighting 23 points with greatest rainrate differences used for outside diagrams. Black lines in outside diagrams are linear least squares fit lines to indicate general trend with respect to increasing rainrate difference.

Figure 19: Three-dimensional depictions of KWAJEX rainrate surfaces derived from GV-radar, synthesized 2A-25, and synthesized 2A-12. Surfaces are smoothed using 11 x 11 averaging filter. White enclosed areas in lo-emission/lo-scattering regions of each surface indicate approximate area of matched-up aircraft microphysical data (i.e., in *E-S* coordinate space).

Figure 20: Upper-left panel depicts observed minus assumed LWC difference vs. GV-radar minus 2A-12 rainrate difference at *E*-index & *S*-index > 0.5; lower-left panel shows same for *E*-index > 0.5 & *S*-index < 0.5. Right two panels are assumed (2A-12 derived) vs. observed (2A-25 derived) LWCs at same points and same *E-S* regions as left two panels.

Figure 21a: Top panel shows composite profile of matched KWAJEX aircraft and 2A-12 IWC data with cubic spline-smoothed average curve fits (blue/red lines). Bottom panel shows same as top except for LWC.

Figure 21b: Composite-average altitude vs. liquid and ice water content profiles of aircraft and 2A-12-derived LWC and IWC. Profiles are equivalent to those shown in Fig. 21a except for individual data points being removed and abscissa scales reduced.

Figure 22: Three-dimensional illustration of how convective fraction specification to 2A-12 algorithm (middle panel) changes original-unmodified rainrate profiles (top panel) to final-modified profiles (bottom panel) at hi-emission/hi-scattering points. Surfaces are smoothed using 11 x 11 averaging filter.

Figure 23: Microphysical water transfer processes amongst six hydrometeor categories based on parameterizations used in UW-NMS model and CSU-RAMS microphysics module. Legend at bottom lists primary microphysical process for each numbered inter-category mass exhange process.

Figure 24: Top panel shows averaged IWC profiles composited over all superpixel-matched microphysical A/C measurements for 4 ice habits (graupel, aggregates, needle/columns, indeterminate ice particles). Note needle/column profile lies very close to altitude axis. Bottom panel shows similar profiles except in terms of fraction of total ice water content.

Figure 1: Modeled brightness temperatures versus rainrates for three microwave frequencies for land and ocean backgrounds. [After Spencer et al., 1989.]
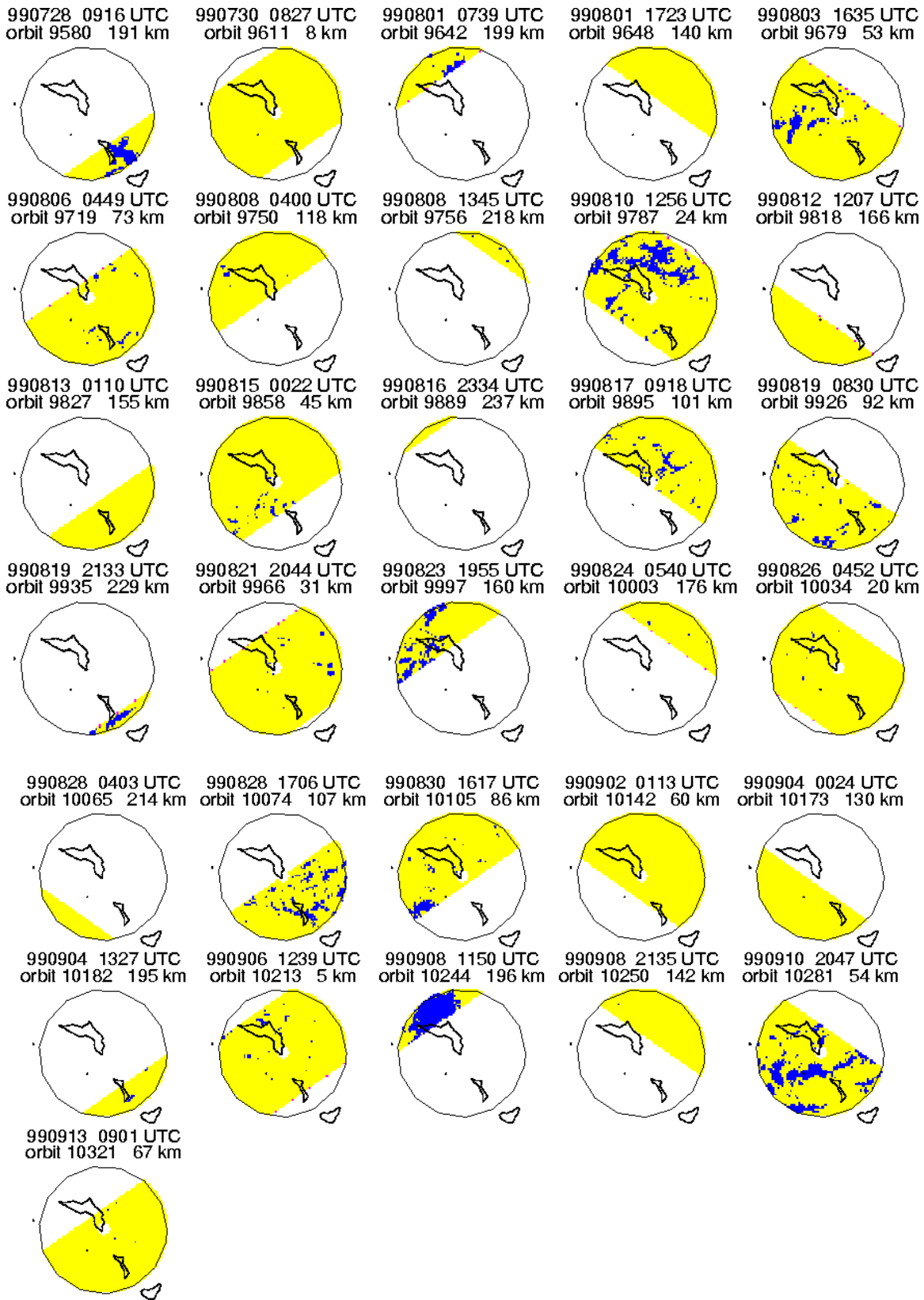
Figure 2: PR overpasses of Kwajalein ground radar domain during KWAJEX experiment period (26 Jul - 14 Sep'99).
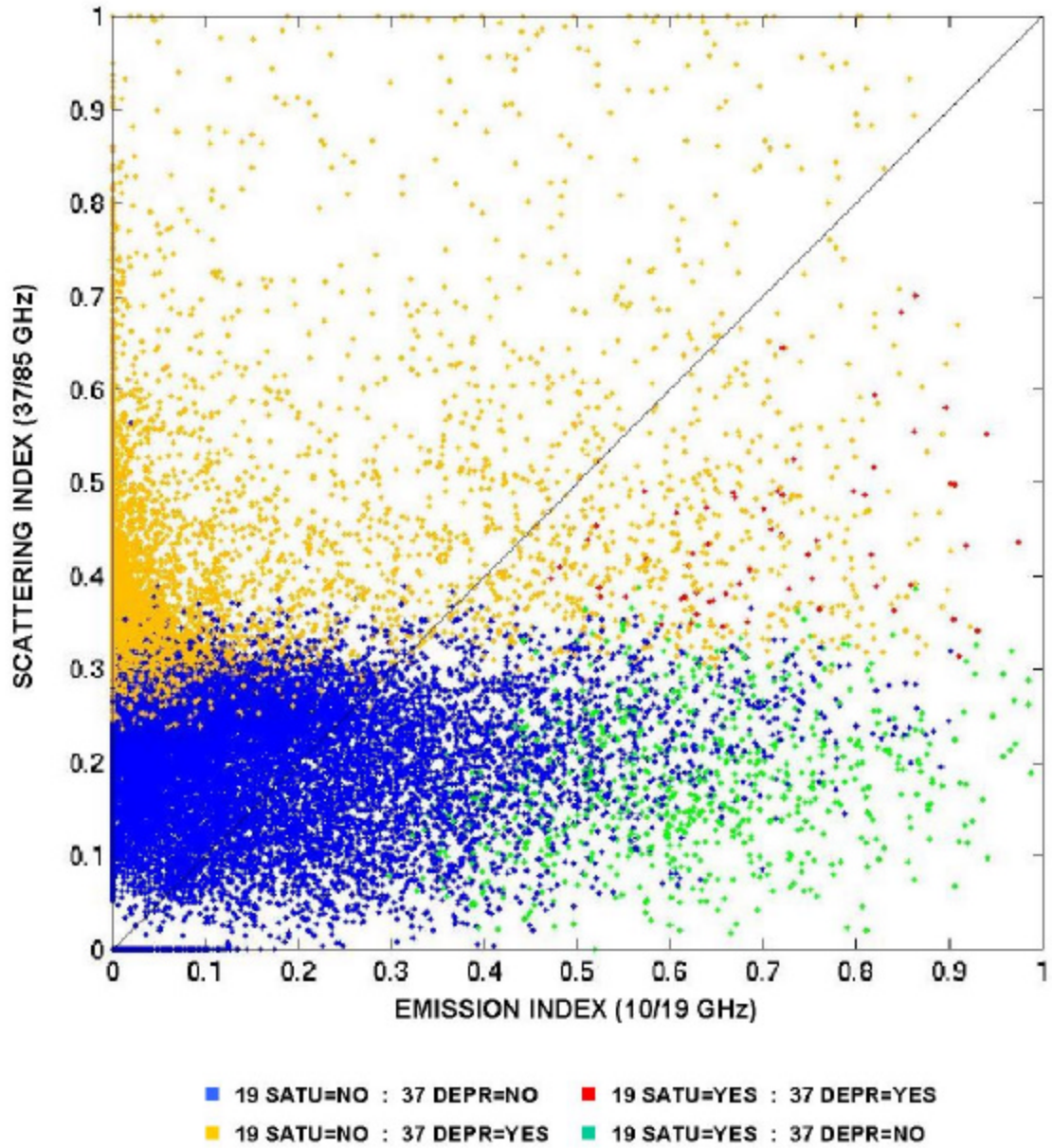
Figure 3: *E-S* diagram depicting *E*-index and *S*-index values for all 40140 AMPR-derived "wet" superpixels from 28 KWAJEX DC-8 flights. Each point is further characterized by color-coding indicating 19.35 GHz saturation and/or 37.1 GHz depression properties.
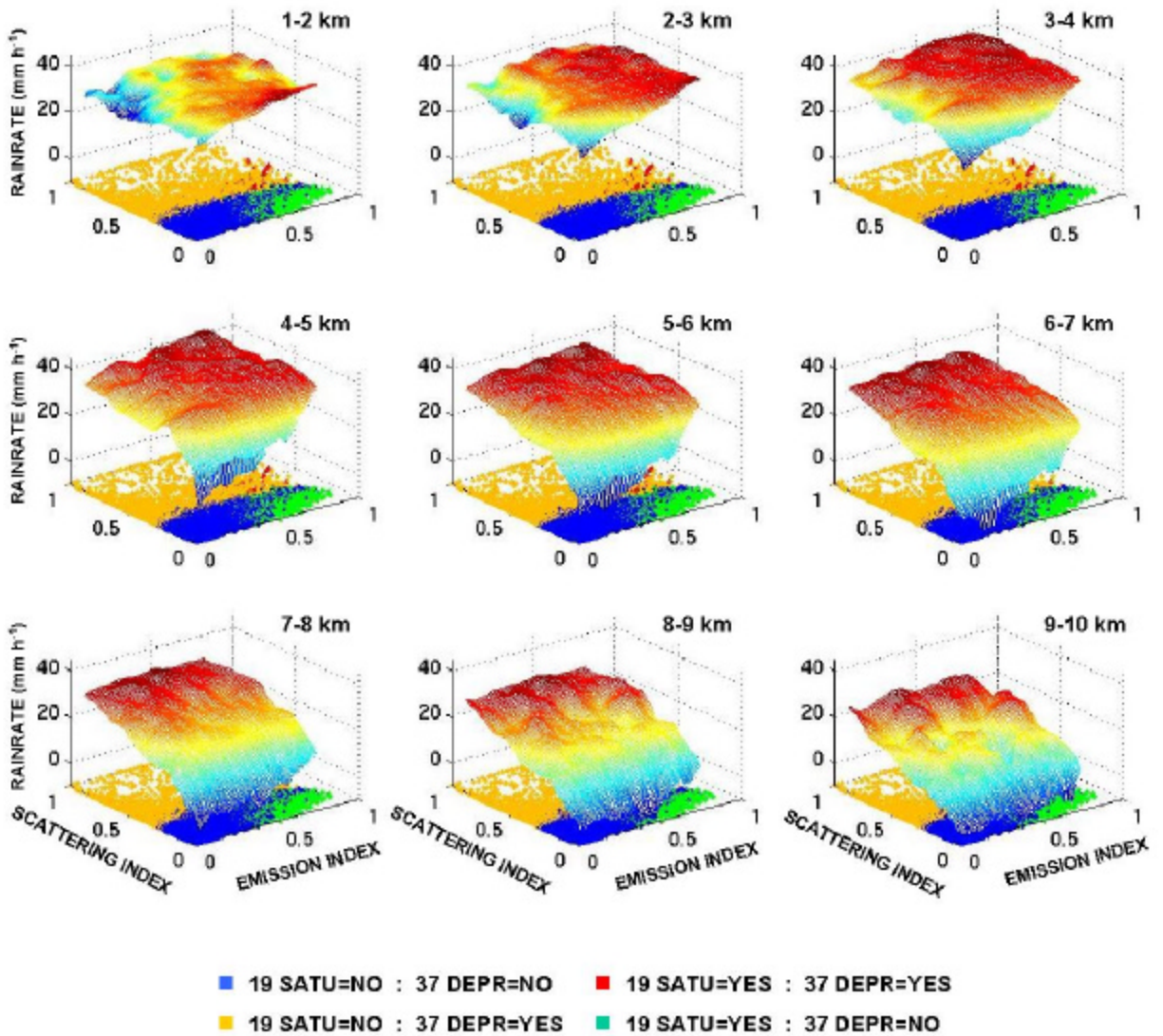
Figure 4: ARMAR reflectivity surfaces in matched *E-S* space where surfaces have been smoothed by 11 x 11 averaging filter for each of 9 layers shown (ARMAR-AMPR QC match-ups). Each ARMAR superpixel used for respective *Z*-surface is color-coded in base-plane according to bottom legend.
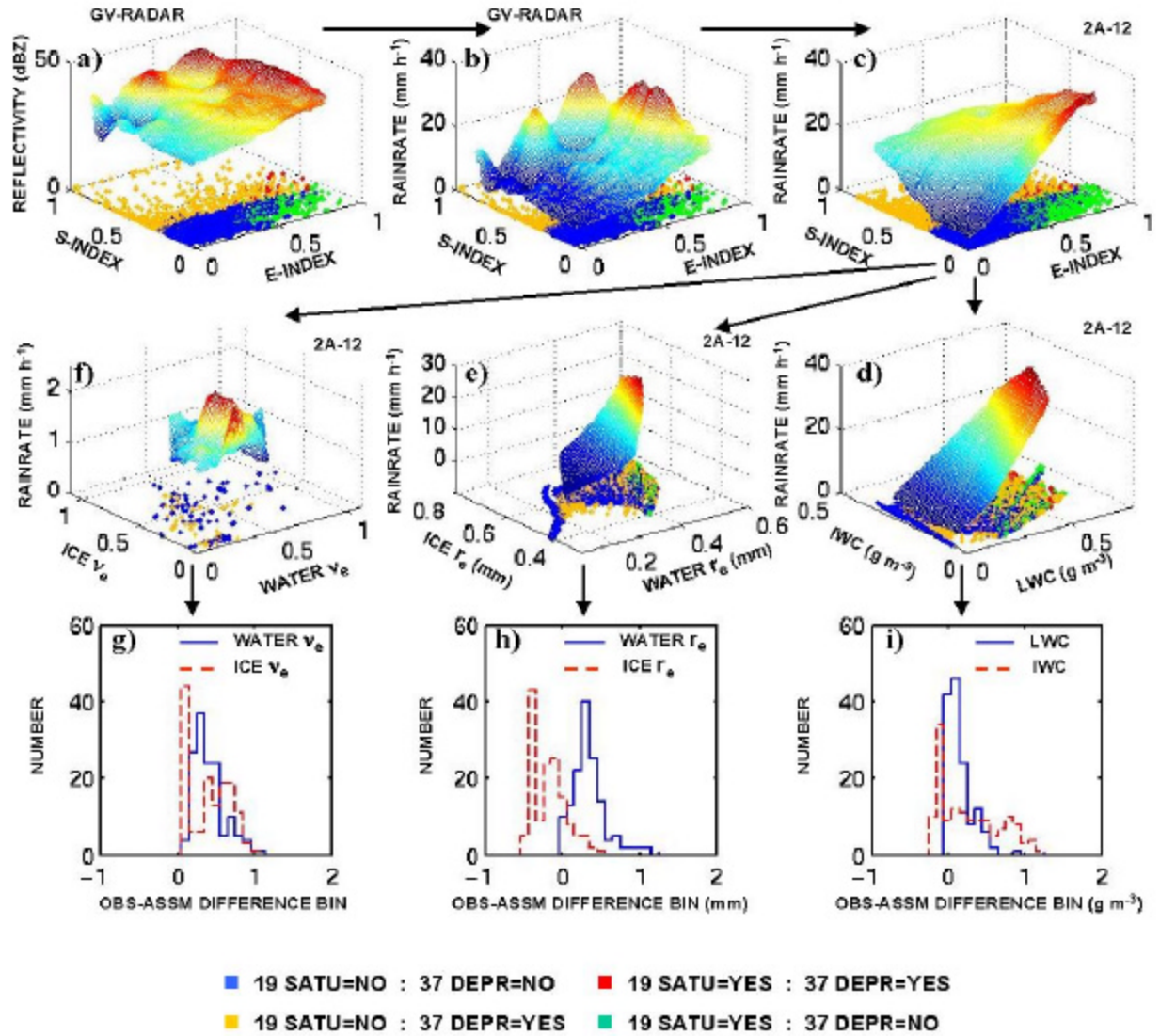
Figure 5: Three-dimensional charts and histograms depicting relationships among reflectivity-rainrate surfaces in *E-S* space (panels a-c), rainrate surfaces in total column microphysical parameter space (panels d-f), and observed-assumed difference histograms (g-i)—where panels (a) through (f) are smoothed using 11 x 11 averaging filter. Individual panels show: (a) GV-radar reflectivity (HQ values), (b) GV-radar rainrate (HQ values), (c) 2A-12 rainrate (QC values), (d) 2A-12 rainrate in assumed total column LWC-IWC space, (e) 2A-12 rainrate in assumed total column water-ice effective radius space, (f) 2A-12 rainrate in observed total column water-ice effective variance space (note assumed coordinates would be constant at 1/3), (g)-(i) histograms of observed-assumed total column microphysical parameter differences.
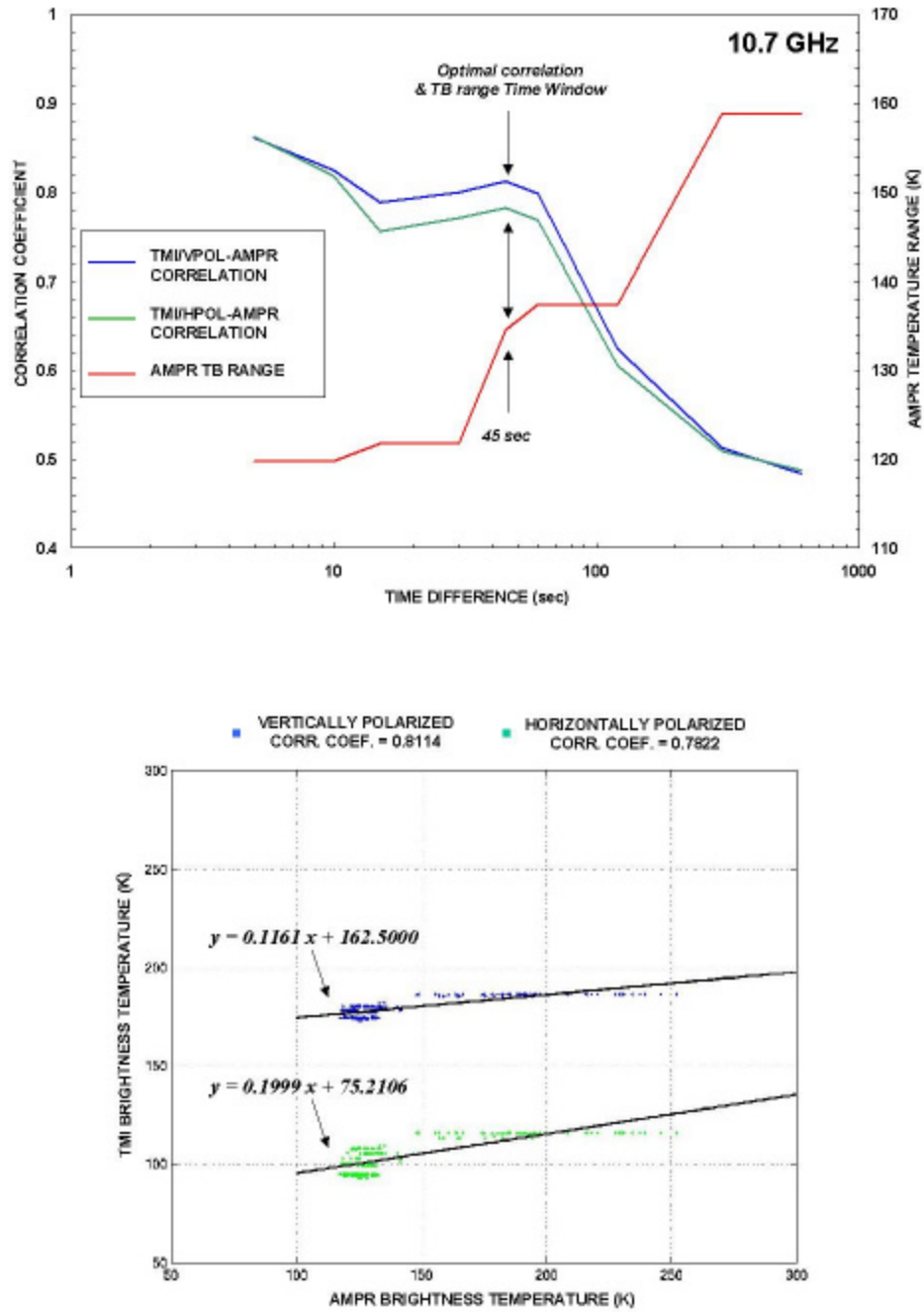
Figure 6a: 10.7 GHz TMI synthesis optimization diagram (top panel) plotted as correlation coefficient with respect to AMPR-TMI overpass time difference and synthesis regression curves (bottom panel).
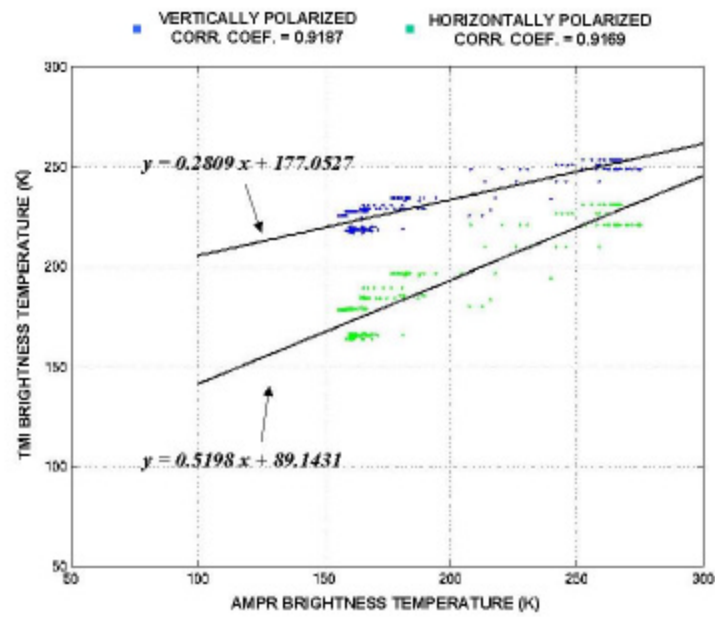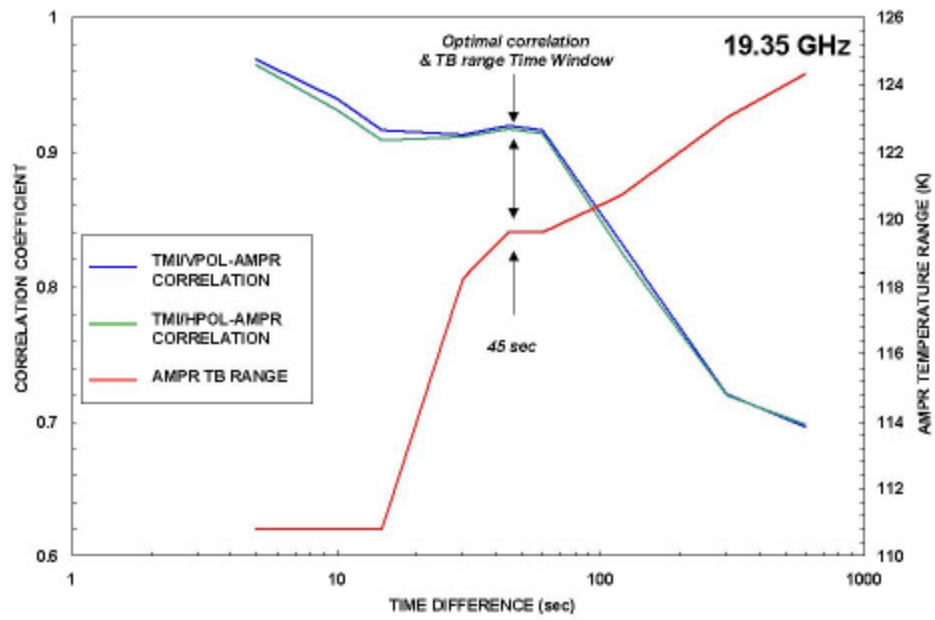
Figure 6b: Same as Fig. 6a except for 19.35 GHz.

80
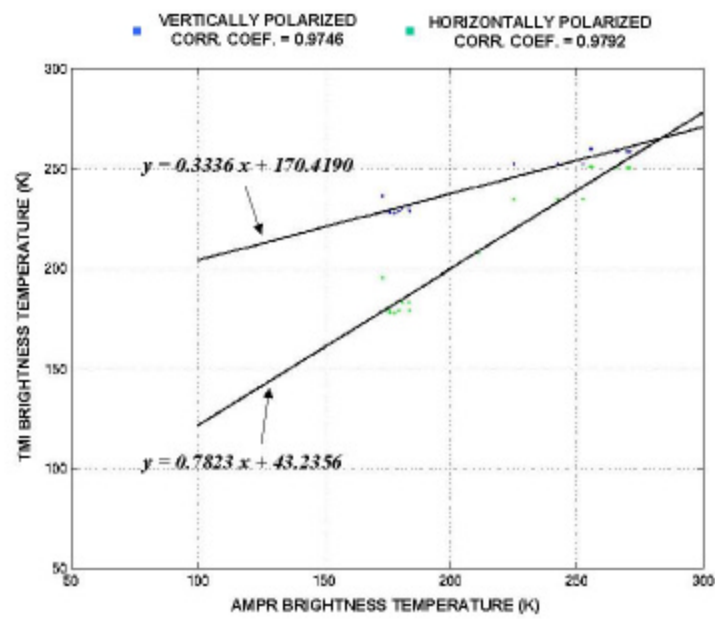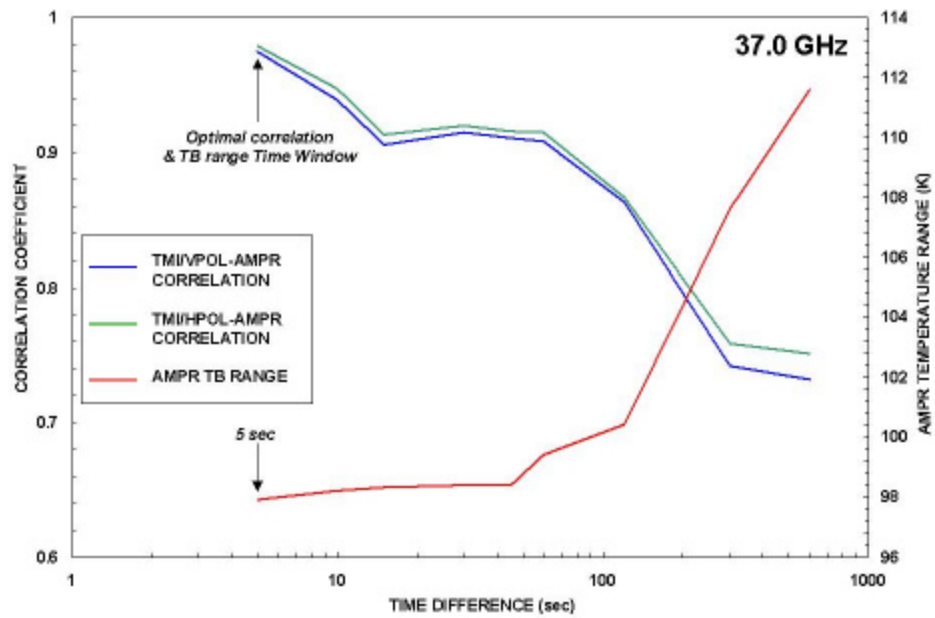
Figure 6c: Same as Fig. 6a except for 37.0 GHz.
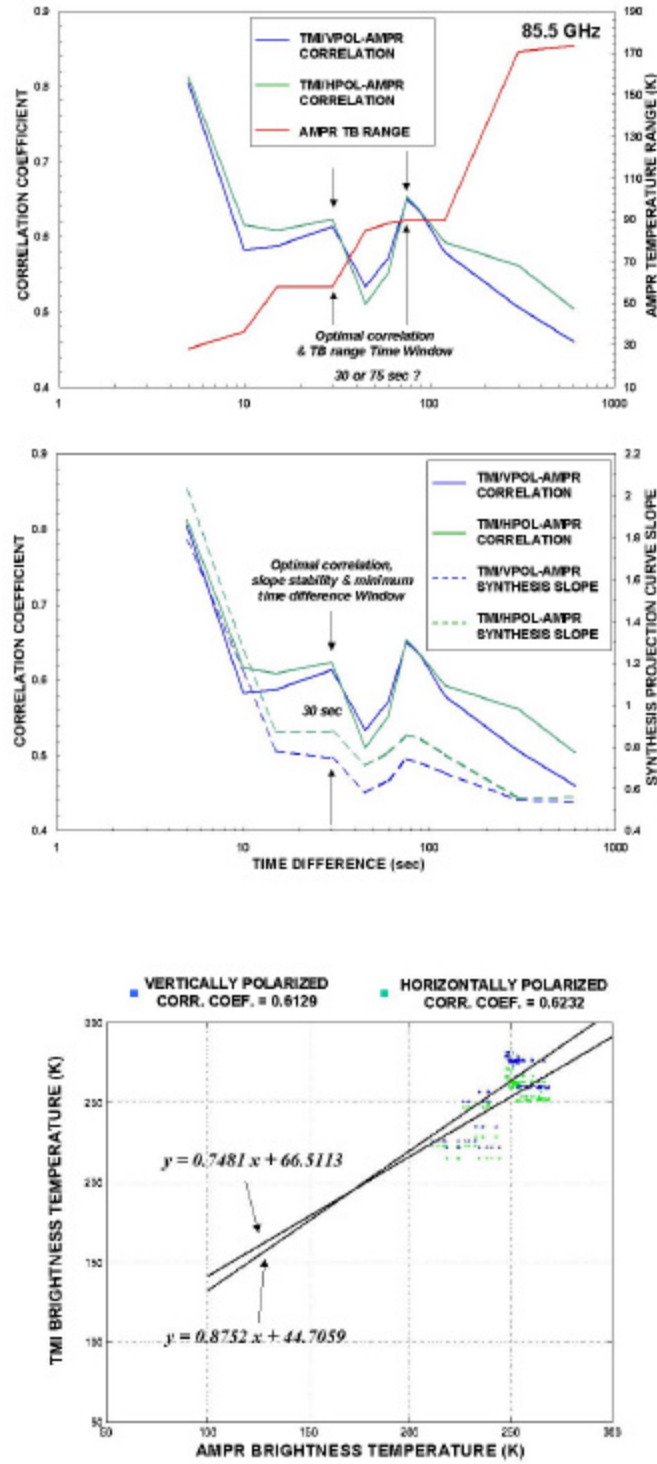
Figure 6d: Same as Fig. 6a except for 85.5 GHz and inclusion of slope optimization analysis (middle panel).
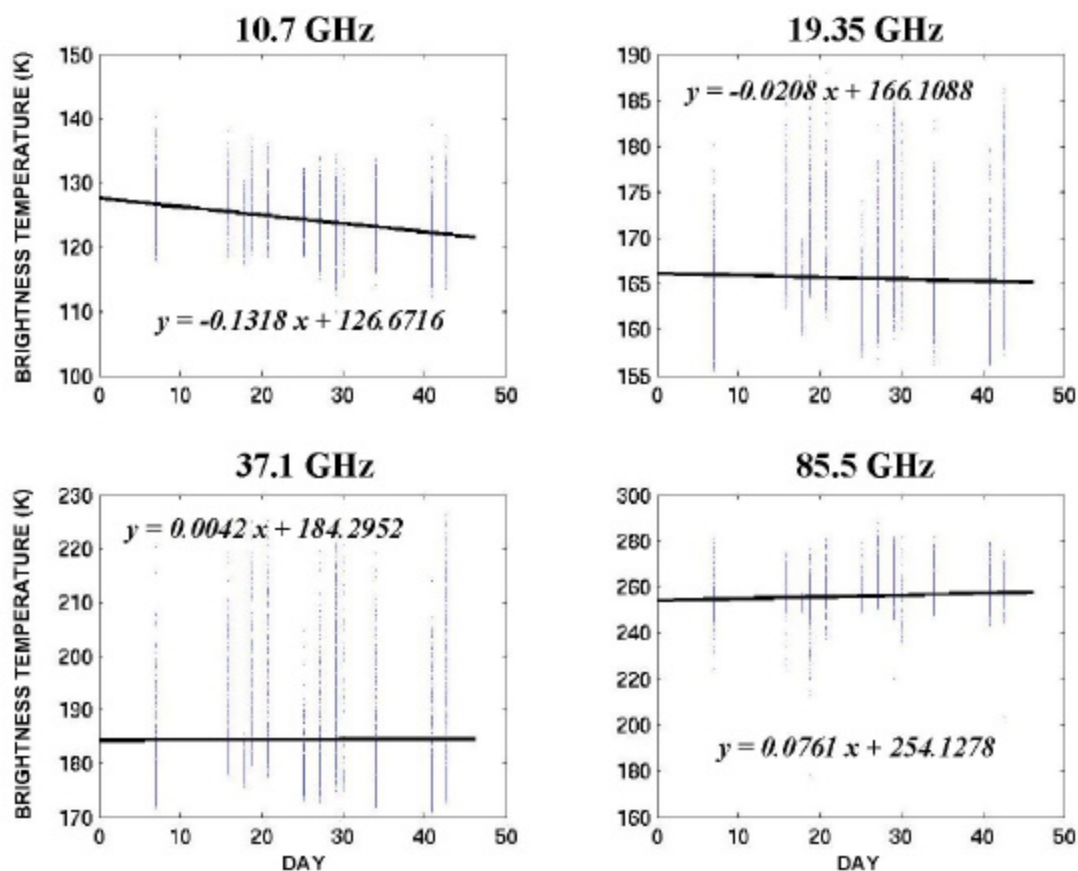
Figure 7: Linear regression curves for each of 4 AMPR channels of 4923 non-raining KWAJEX superpixels. Projections provide clear-air background AMPR Tbs for input into 2A-12 algorithm. KWAJEX flight day 0 of time series is 30 Jul'99; flight day 47 is 14 Sep'99.
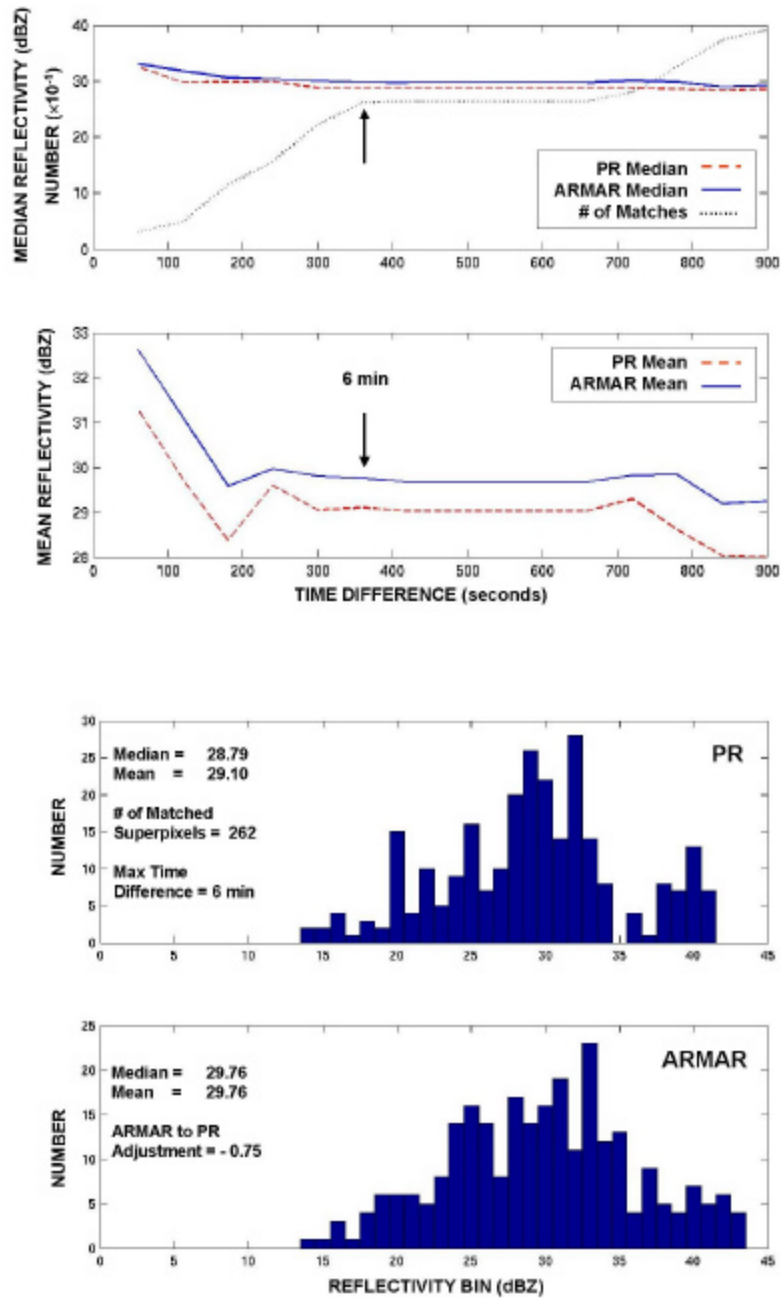
Figure 8: Top 2 panels show 3-4 km layer ARMAR to PR distribution mean, median, match-up number (plotted in number x 10^{-1}) sensitivity to observation time difference. Bottom 2 panels show 3-4 km layer PR and ARMAR matched distribution histograms.
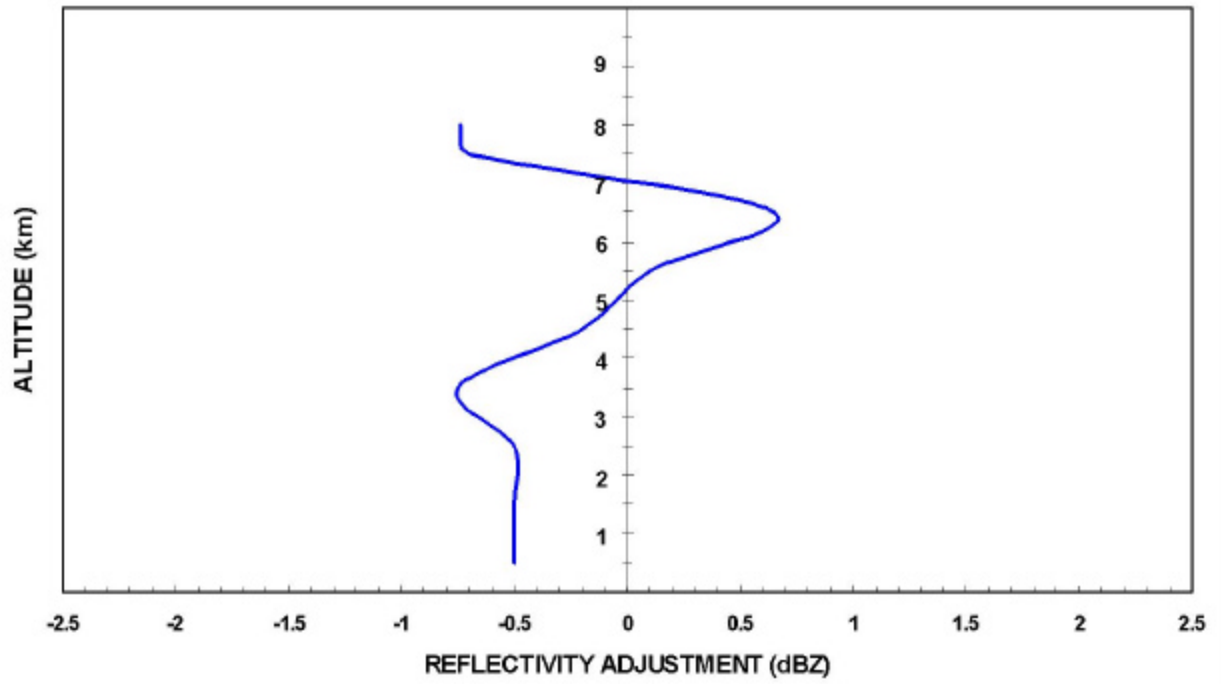
Figure 9: Smoothed altitude variation of 8-layer average ARMAR to PR calibration corrections for KWAJEX.

Figure 10a: Top panel shows GV-radar convective/stratiform mapping plotted by convective/stratiform index (CSI) vs. superpixel number. Bottom panel shows variation of convective superpixel fraction with changes in CSI.

Figure 10b: Top panel shows GV-radar convective/stratiform mapping plotted in *E-S* space. Bottom panel shows *E-S* space separation of convective and stratiform superpixels using convective fraction values > 0.5 = convective (or CSI > 0.31 = convective).

87

Figure 11a: Comparison of 2A-12-derived (blue plot) and GV-radar-derived (red plot) rainrates at matched HQ GV-radar superpixels. [HQ indicates high resolution range (range < 78 km) and best interpolation quality (interpolation quality = 8).]

Figure 11b: Top panel shows scatter diagram of 2A-12 and GV-radar rainrates equivalent to those given in Fig. 11a. Bottom 2 panels show individual histograms.

Figure 12: Left three panels show comparisons involving 2A-25 rainrates with respect to GV-radar (top-left), 2A-12 (middle-left), and ARMAR (bottom-left) rainrates vs. matched HQ or QC superpixel number. Right three panels show corresponding scatter diagrams.

Figure 13: Rainrate (top two panels) and liquid water content (bottom two panels) intercomparisons and scatter diagrams of 2A-25- vs. Convair-derived values in 2-3 km layer. Convair rainrates and LWCs recalculated from particle size spectra after conversion of ice artifacts to liquid water spheres. 2A-25 LWCs calculated from rainrates assuming Marshall-Palmer distribution.

Figure 14: Top panel shows *E-S* diagram of all merged-matched aircraft priority leg microphysical measurements. Bottom panel shows *E-S* diagram of only those superpixels where Convair observations match up with one or both of other aircraft observations -- these points are used to produce total column microphysical profiles.

Figure 15: Total water content ice fraction vs. outside air temperature for all matched Convair and Citation measurements. Top panel shows diagram of unrealistic ice fraction values in Convair data at temperatures > +5 ^{o}C, whereas bottom panel shows same diagram after Convair ice artifacts are converted to liquid water spheres.

Figure 16: Scatter diagram and histogram comparisons of reflectivity calculated from aircraft particle spectra vs. ARMAR. Left panels show ARMAR vs. Convair in 2-3 km layer, whereas right panels show ARMAR vs. Citation in 6-7 km layer. Convair reflectivities are calculated after ice artifact conversion to liquid water.

Figure 17a: Scatter diagrams of 2A-12 vs. aircraft-observed LWCs in 0-4 km layer (left two panels—Convair) and 5-10 km layer (right two panels -- Citation). Rainrate differences color-coded according to GV-radar minus 2A-12 rainrate differences.

Figure 17b: Scatter diagrams of 2A-12 vs. aircraft-observed IWCs in layers specified. Rainrate differences color-coded as in Fig. 17a.

Figure 18: Six outside panels show observed minus assumed column average microphysical parameter differences vs. GV-radar minus 2A-12 rainrate differences (six outside panels) with respect to liquid and ice. Single center panel shows scatter diagram of 2A-12 vs. GV-radar rainrate, highlighting 23 points with greatest rainrate differences used for outside diagrams. Black lines in outside diagrams are linear least squares fit lines to indicate general trend with respect to increasing rainrate difference.

Figure 19: Three-dimensional depictions of KWAJEX rainrate surfaces derived from GV-radar, synthesized 2A-25, and synthesized 2A-12. Surfaces are smoothed using 11 x 11 averaging filter. White enclosed areas in lo-emission/lo-scattering regions of each surface indicate approximate area of matched-up aircraft microphysical data (i.e., in *E-S* coordinate space).
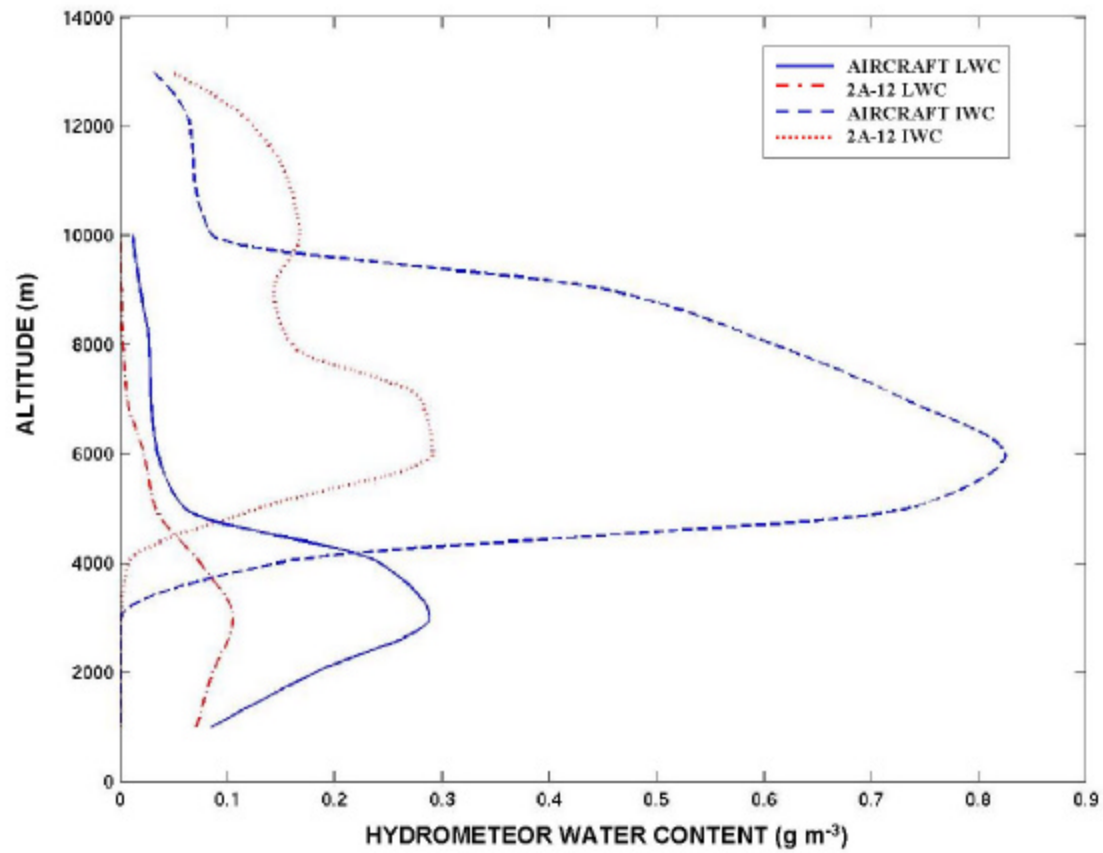
Figure 20: Upper-left panel depicts observed minus assumed LWC difference vs. GV-radar minus 2A-12 rainrate difference at *E*-index & *S*-index > 0.5; lower-left panel shows same for *E*-index > 0.5 & *S*-index < 0.5. Right two panels are assumed (2A-12 derived) vs. observed (2A-25 derived) LWCs at same points and same *E-S* regions as left two panels.
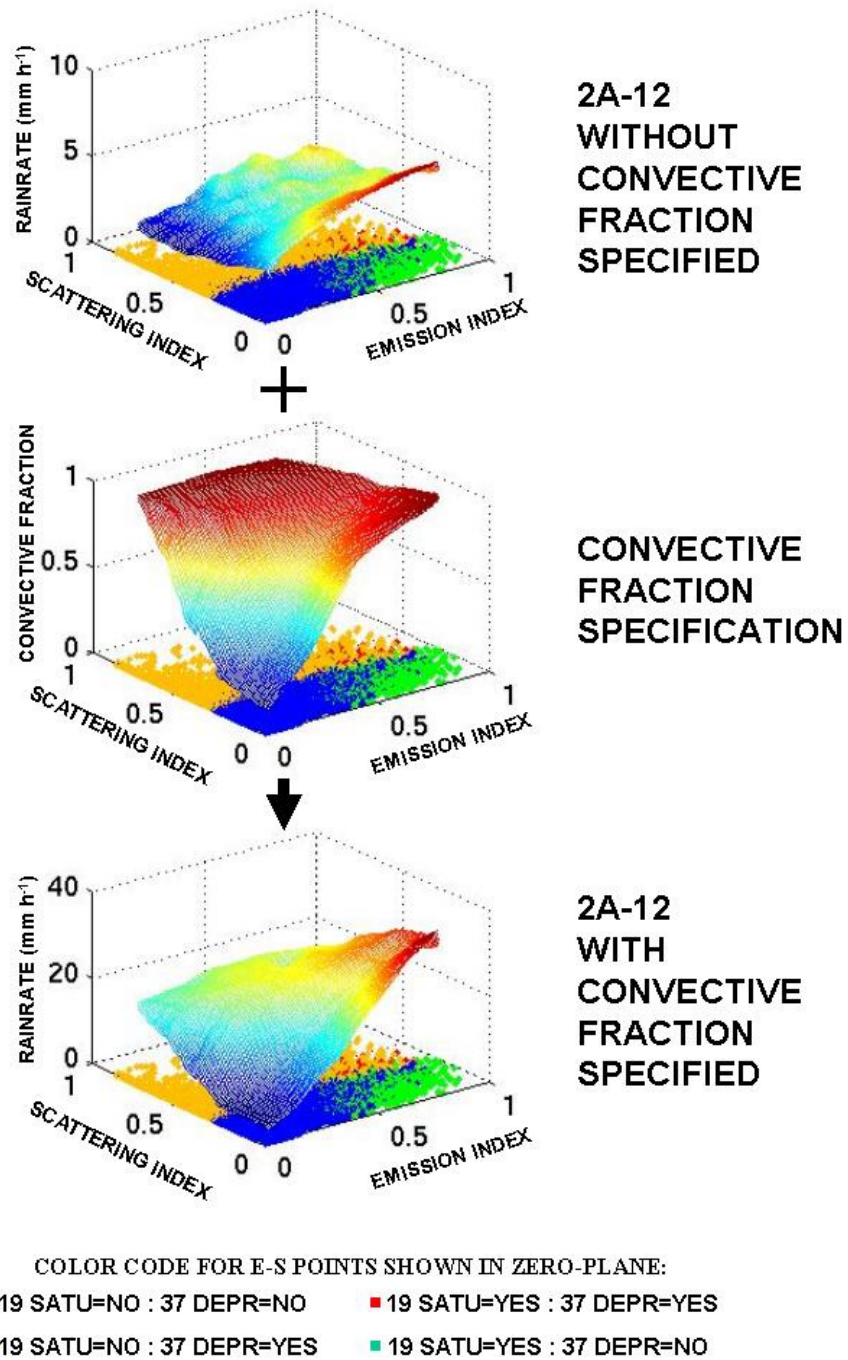
Figure 21a: Top panel shows composite profile of matched KWAJEX aircraft and 2A-12 IWC data with cubic spline-smoothed average curve fits (blue/red lines). Bottom panel shows same as top except for LWC.
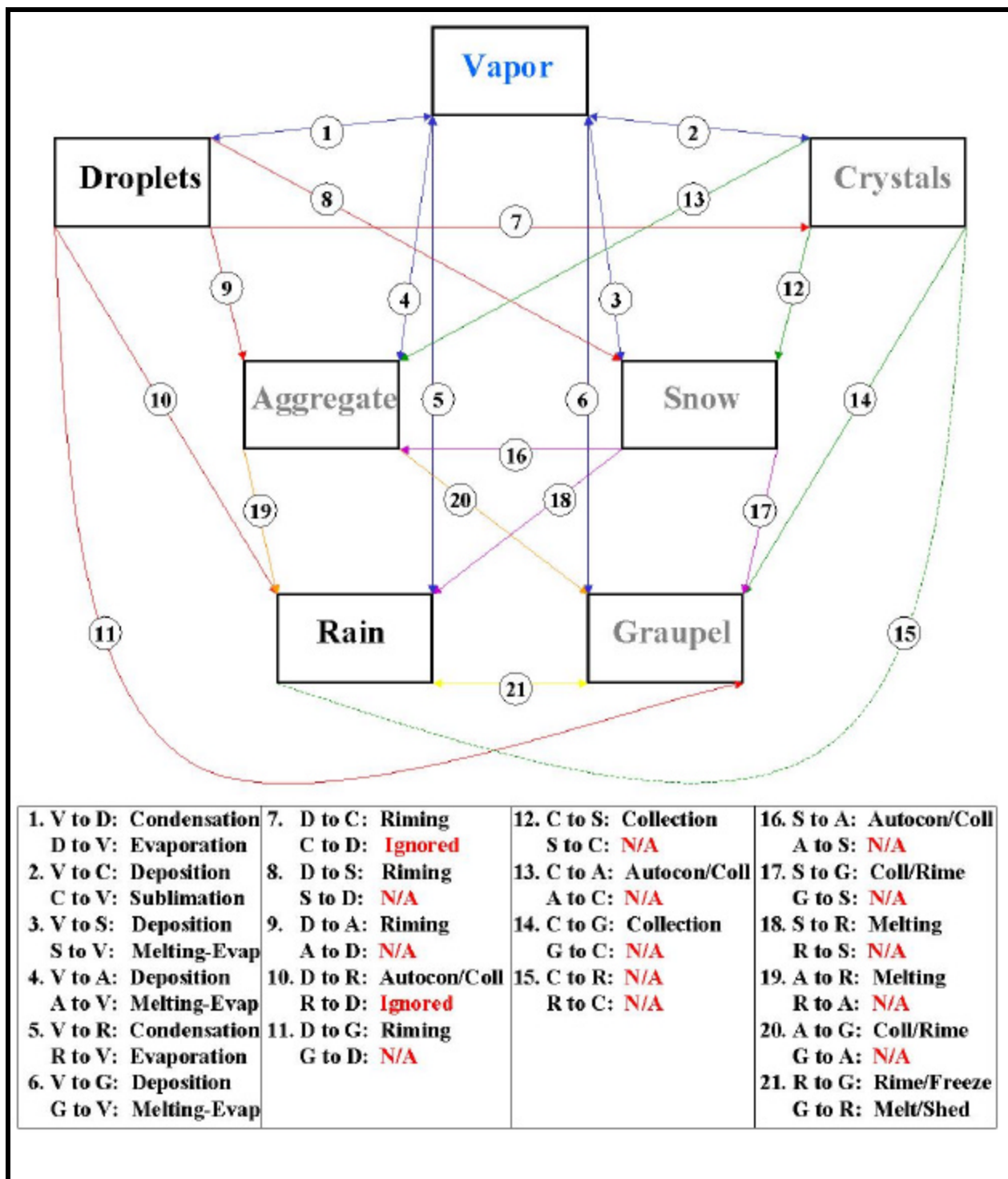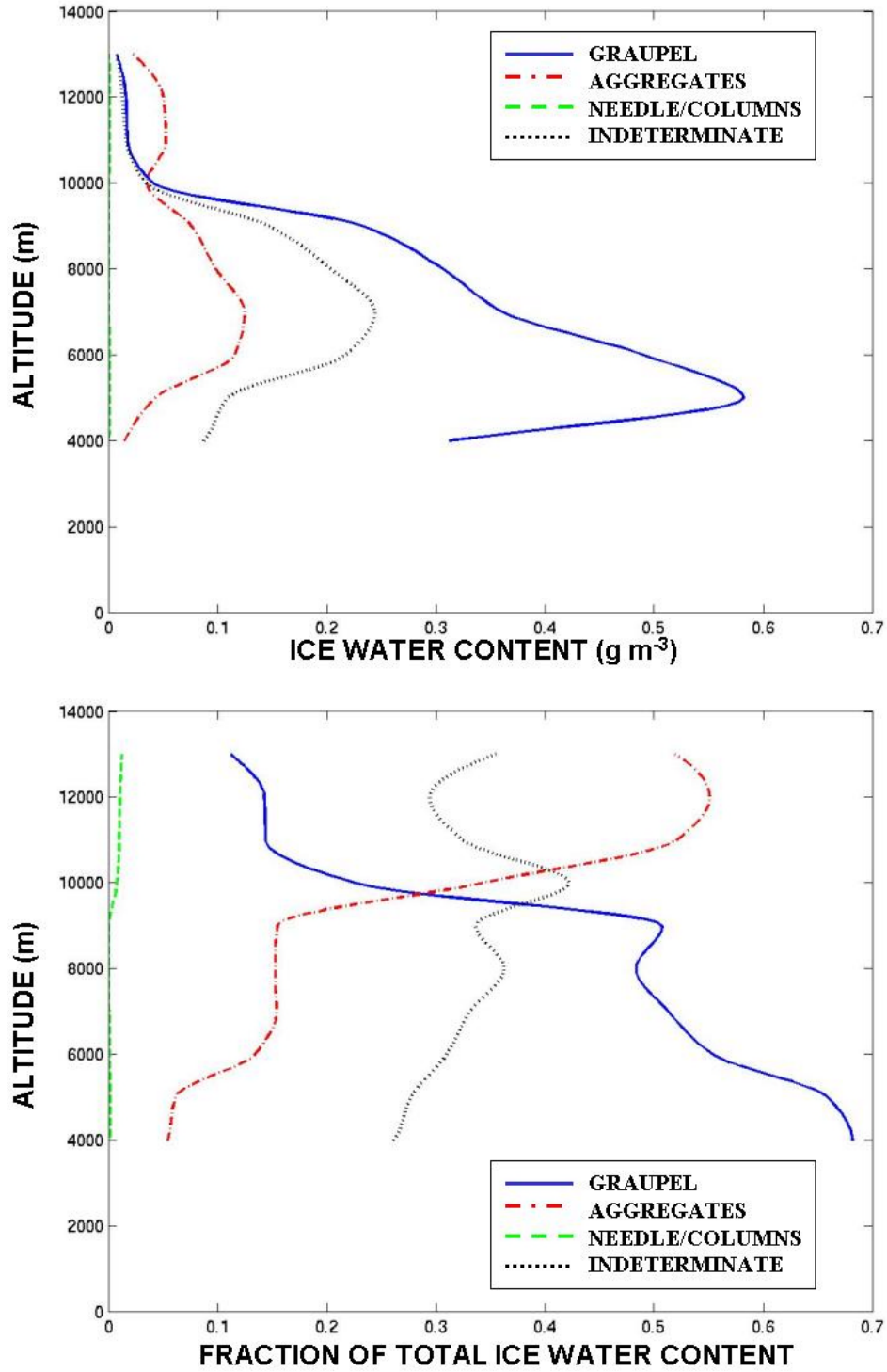
Figure 21b: Composite-average altitude vs. liquid and ice water content profiles of aircraft and 2A-12-derived LWC and IWC. Profiles are equivalent to those shown in Fig. 21a except for individual data points being removed and abscissa scales reduced.

Figure 22: Three-dimensional illustration of how convective fraction specification to 2A-12 algorithm (middle panel) changes original-unmodified rainrate profiles (top panel) to final-modified profiles (bottom panel) at hi-emission/hi-scattering points. Surfaces are smoothed using 11 x 11 averaging filter.

Figure 23: Microphysical water transfer processes amongst six hydrometeor categories based on parameterizations used in UW-NMS model and CSU-RAMS microphysics module. Legend at bottom lists primary microphysical process for each numbered inter-category mass exhange process.

Figure 24: Top panel shows averaged IWC profiles composited over all superpixel-matched microphysical A/C measurements for 4 ice habits (graupel, aggregates, needle/columns, indeterminate ice particles). Note needle/column profile lies very close to altitude axis. Bottom panel shows similar profiles except in terms of fraction of total ice water content.